

# What Makes a Good Arylsulfatase Substrate? Application in the Design of Antibody-Drug Conjugate Linkers.

**Michael Brown**

A thesis submitted in fulfilment of the requirements  
for the degree of Master of Science in pharmacology.  
The University of Auckland, 2023.

## Abstract

Antibody-drug conjugates (ADCs) are an emerging class of targeted therapies comprised of cytotoxic small molecule payloads bound to a monoclonal antibody by covalent linkers. The linkers are integral components of ADCs as they must be both stable in circulation and release the payload following target engagement. Enzyme-cleavable linkers utilise intracellular enzymes to trigger payload release following ADC binding and internalisation. Recently, arylsulfatase-cleavable linkers have been explored, illustrating several desirable characteristics for application to ADCs. Sulfatases hydrolyse sulfate monoesters to form alcohols. While each enzyme is highly selective for its natural substrates, sulfatases also hydrolyse small synthetic arylsulfates to phenols. The binding mode of sulfatases with their substrates is poorly defined, thus improved understanding of substrate recognition/binding is required to design optimal sulfatase cleavable linkers. This work aimed to generate empirical structure activity relationships of sulfate hydrolysis and payload release for model sulfatase-cleavable linkers against human arylsulfatase A (ARSA). Eight model arylsulfatase-cleavable linkers were synthesised from commercially available phenols and screened against ARSA. Following sulfate hydrolysis these linkers undergo a 1,6-elimination of a phenol intermediate to release a coumarin payload. This thesis identified ortho-difluoro and ortho-nitro substituted sulfate linkers as the most promising sulfate substrates for development of ARSA-cleavable linkers. These linkers were excellent ARSA substrates with the fastest rates of sulfate hydrolysis in this library. This work found low steric impact and electron withdrawal as beneficial properties for sulfate hydrolysis. The resonance withdrawing effect of the nitro group is able to overcome its steric effect, while a trifluoromethyl analogue was a poorer substrate than an unsubstituted control despite its strong inductive withdrawing effect. However, the resonance effect of the nitro substituent significantly reduced the rate payload release. Indeed, reducing pKa of the phenol intermediate reduced the rate of fragmentation and subsequently payload release. These sulfates linkers can be investigated in ADC development in order to elucidate the optimal combination of these properties.

## **Acknowledgements**

I could not have completed this thesis without the continuous guidance and support from many generous people and to that I would like to express my deepest thanks.

I would like to show my sincere appreciation for my supervisors Dr Moana Tercel and Dr Benjamin Dickson, who have given me constant mentorship and support throughout this work. Thank you for being so welcoming and nurturing during an interrupted two years. Your reassurance and unwavering enthusiasm has inspired me throughout this thesis.

I have been very fortunate to be a part of the Auckland Cancer Society Research Centre to undertake this work. A special thank you to Dr Adrain Blazer for NMR services, Sree Bhavan for HRMS analysis, Sisira Kumara for HPLC purity analysis and Wilson Sun for melting point analysis. It has been a joy to work alongside a group of warm, friendly and dedicated scientists. All your support has been greatly appreciated.

To my family, Barry, Angela, Kate and George, thank you for your unwavering support of me and all I do. A special thank you for listening to my ramblings about work, as uninteresting as they may have been. I would also like to thank Brendan, Anna, and Liam Spring and Chris Goodwin for supporting me throughout this work and welcoming me into your home during the lockdown. Finally, I would like to thank my loving partner Mary Spring. Thank you for your immense patience, constant kindness and proof-reading prowess. Without your support this work would not have been possible.

# Table of Contents

<i>Abstract</i> .....	<i>iii</i>
<i>Acknowledgements</i> .....	<i>iv</i>
<i>List of Figures</i> .....	<i>vii</i>
<i>List of Tables</i> .....	<i>viii</i>
<i>List of Schemes</i> .....	<i>ix</i>
<i>List of Abbreviations</i> .....	<i>x</i>
<b>1. Introduction</b> .....	<b>2</b>
<b>1.1 Cancer Chemotherapy</b> .....	<b>2</b>
<b>1.2 Antibodies</b> .....	<b>3</b>
<b>1.3 Antibody-Drug Conjugates</b> .....	<b>5</b>
1.3.1 Mechanism of Action of ADCs.....	7
1.3.2 Considerations in ADC design .....	8
<b>1.4 Payloads</b> .....	<b>10</b>
1.4.1 Auristatins .....	11
1.4.2 Maytansinoids .....	12
1.4.3 Calicheamicins .....	13
1.4.4 Topoisomerase I inhibitors.....	13
1.4.5 Pyrrolbenzodiazepine dimers .....	14
1.4.6 Duocarmycins.....	14
1.4.7 Duocarmycin-PBD heterodimers .....	15
1.4.8 Non-cancer drugs.....	16
<b>1.5 Linkers</b> .....	<b>16</b>
1.5.1 Homogeneity in bioconjugation .....	16
1.5.2 Conjugation Methods .....	18
1.5.3 Drug-linker attachment.....	21
1.5.4 Enzyme cleavable linkers .....	26
<b>1.6 Sulfatase-cleavable linkers</b> .....	<b>31</b>
<b>1.7 Sulfatases</b> .....	<b>34</b>
1.7.1 Structure .....	35
1.7.2 Sulfatase active site .....	37
1.7.3 Mechanism.....	40
1.7.4 Arylsulfatase activity .....	41
1.7.5 Human arylsulfatase A (ARSA) .....	43
<b>1.8 This work</b> .....	<b>44</b>
<b>2. Discussion</b> .....	<b>47</b>
<b>2.1 Synthesis</b> .....	<b>47</b>
2.1.1 Synthetic objectives .....	47
2.1.2 Synthesis of sulfuryl imidazolium salt 14.....	49
2.1.3 Synthesis of 7a.....	50
2.1.4 Synthesis of 7b-h .....	51
2.1.5 Synthesis of 5a and 5c .....	53
2.1.6 Model carbamate formation.....	53
2.1.7 Resynthesis of 5a and 5c.....	55
2.1.8 Synthesis of 5a-i .....	56
2.1.9 Synthesis of 1a-g,i .....	57
<b>2.2 Enzyme activity assays</b> .....	<b>58</b>

2.2.1	Enzyme condition .....	58
2.2.2	AMC (3) standard curve .....	59
2.2.3	Method development .....	60
2.2.4	Assessment of sulfate hydrolysis .....	62
2.2.5	Assessment of payload release.....	67
2.2.6	Application as ADC linkers .....	70
<b>2.3</b>	<b>Limitations and Future work.....</b>	<b>71</b>
<b>2.4</b>	<b>Conclusions.....</b>	<b>72</b>
<b>3.</b>	<b><i>Experimental</i>.....</b>	<b>74</b>
<b>3.1</b>	<b>General details.....</b>	<b>74</b>
<b>3.2</b>	<b>Characterisation.....</b>	<b>74</b>
3.2.1	Safety risks.....	75
<b>3.3</b>	<b>Assay procedures .....</b>	<b>75</b>
3.3.1	Assay procedure A.....	75
3.3.2	Assay procedure B.....	76
3.3.3	Standard curve .....	76
<b>3.4</b>	<b>Synthesis.....</b>	<b>76</b>
	<b><i>References:</i>.....</b>	<b>97</b>

## List of Figures

<b>Figure 1.</b> Dose-response curve depicting therapeutic index.....	2
<b>Figure 2.</b> Structure of an antibody.....	3
<b>Figure 3.</b> Limitations of monoclonal antibodies against solid tumours. a. mAbs only affect antigen positive cells in heterogenous tumours. ....	4
<b>Figure 4.</b> Chemical structures of the 11 clinically approved antibody drug conjugate drug linkers.....	6
<b>Figure 5.</b> Antibody-Drug Conjugate Mechanism of action.....	7
<b>Figure 6.</b> Comparison of cytotoxicity of reported ADC payloads. ....	11
<b>Figure 7.</b> Structure of Auristatin analogues Dolastatin 10, MMAE and MMAF.....	12
<b>Figure 8.</b> Structure of Maytansinoid analogues Maytansine, DM1, DM3, and DM4.....	12
<b>Figure 9.</b> Structure of calicheamicins.....	13
<b>Figure 10.</b> Structures of Top1 inhibitors Dxd and SN-38.....	14
<b>Figure 11.</b> PBD dimer SG3199 employed by loncastuximab tesirine. ....	14
<b>Figure 12.</b> Structure of duocarmycin payload of SYD985.....	15
<b>Figure 13.</b> Structure of a duocarmycin-PBD dimer. ....	16
<b>Figure 14.</b> Effects of DAR, attachment site and homogeneity on the characteristics of ADCs.....	17
<b>Figure 15.</b> Conjugation by a. the reaction of NHS-ester reagent with Lysine residues and b. the reaction of maleimide reagents with cysteine residues. ....	18
<b>Figure 16.</b> Illustration of, and a strategies to overcome maleimide linker liabilities. ....	19
<b>Figure 17.</b> Use of Disulfide rebridging using bis-reactive rebridging reagents.. ....	20
<b>Figure 18.</b> Noncleavable SMCC and mc linkers are released with an additional charged Lys or Cys appendage respectively following enzymatic degradation of the mAb within lysosomes.....	21
<b>Figure 19.</b> a. Hydrazone containing “ozogamicin” drug-linker delivers a <i>N</i> -acyl calicheamicin payload. b. Hydrolysis of the <i>N</i> -acyl hydrazone occurs at acidic pH. ....	23
<b>Figure 20.</b> Acid-cleavable <i>para</i> -aminobenzyl carbonate employed in sacituzumab govitecan.....	23
<b>Figure 21.</b> Reduction of disulfide linkers by glutathione (represented as GSH).....	24
<b>Figure 22.</b> UV-cleavable DMNB linker.....	25
<b>Figure 23.</b> IR-cleavable HMCD linker.....	26
<b>Figure 24.</b> Structure and mechanism of cleavage of dipeptide (Val-Cit) cleavable linkers.....	27
<b>Figure 25.</b> Structure and mechanism of release of examples of a. $\beta$ -glucuronidase and b. $\beta$ -galactosidase cleavable linkers. ....	29
<b>Figure 26.</b> Structure and mechanism of release of dual enzyme Cathepsin/phosphatase and Pyrophosphatase/phosphatase cleavable linkers.....	30

<b>Figure 27.</b> a. Structure and mechanism of release of <i>para</i> -sulfooxy-benzyl carbamate sulfatase cleavable linkers.....	32
<b>Figure 28.</b> Structure and mechanism of release of dual enzyme cleavable sulfatase/ $\beta$ -galactosidase cleavable linkers.....	33
<b>Figure 29.</b> Known human sulfatase substrates.....	35
<b>Figure 30.</b> Cartoon representation of human arylsulfatase A.....	36
<b>Figure 31.</b> Illustrations of the contiguous substrate binding pockets of human sulfatases generated using Pymol®.....	39
<b>Figure 32.</b> Assessment of ARSA activity through conversion of MUFS in 2020 vs. 2022.....	59
<b>Figure 33.</b> a) AMC standard curve at 320 nm for quantification of payload release.....	60
<b>Figure 34.</b> Change in % sulfate and % total AMC over time.....	61
<b>Figure 35.</b> Inconsistent peak areas over time under new 25 $\mu$ M assay conditions with 1a and AMC.....	62
<b>Figure 36.</b> Normalised rate of sulfate 1a-g,i hydrolysis with ARSA.....	63
<b>Figure 37.</b> Normalised sulfate hydrolysis over time of group i substrates.....	64
<b>Figure 38.</b> Normalised rate of sulfate hydrolysis of group ii substrates 1d-f.....	65
<b>Figure 39.</b> Normalised rate of AMC (3) release.....	68
<b>Figure 40.</b> HPLC diode array data of 1f assay, absorbance 320 nm, t = 0, t = 30 mins.....	69
<b>Figure 41.</b> HPLC diode array data of 1e assay, absorbance 320 nm. t=0, t= 30 mins.....	70

## List of Tables

<b>Table 1.</b> Identity and proposed function of conserved active site residues.....	37
<b>Table 2.</b> Rate (nM/min/mg enzyme) and affinity ( $K_m$ ) of arylsulfate probes against human arylsulfatase A-C.....	42
<b>Table 3.</b> Arylsulfate ester protecting strategies. Conditions from respective references above.....	49
<b>Table 4.</b> Summary of reactions in preparation of 7a-k.....	51
<b>Table 5.</b> Summary of reaction conditions for preparation of 21. Yields calculated from NMR analysis of crude material following workup.....	54
<b>Table 6.</b> Summary of reactions in preparation of 5a-g, i.....	56
<b>Table 7.</b> Summary of reactions in preparation of 1a-g, i.....	58
<b>Table 8.</b> Anova analysis of sulfate hydrolysis of 1b-g,i and 1a.....	63
<b>Table 9.</b> Sulfate hydrolysis analysis including the calculated pKa, % sulfate loss at 2 hours and group designation.....	67

## List of Schemes

<b>Scheme 1.</b> Sulfatase hydrolysis of sulfate monoesters (X= O) and sulfamates (X = NH). .....	31
<b>Scheme 2.</b> Proposed Addition-Hydrolysis mechanism of sulfate hydrolysis. ....	40
<b>Scheme 3.</b> Transesterification-elimination mechanism of sulfate hydrolysis. ....	41
<b>Scheme 4.</b> Hydrolysis and fragmentation of model arylsulfatase cleavable linkers. ....	45
<b>Scheme 5.</b> Retrosynthesis of sulfates <b>1a-z</b> from phenols <b>9a-z</b> . ....	47
<b>Scheme 6.</b> Methylation of imidazole sulfonate <b>14</b> . ....	49
<b>Scheme 7.</b> Preparation of <b>7a</b> from <b>9a</b> . ....	50
<b>Scheme 8.</b> Preparation of alcohol <b>7a</b> from <b>17</b> . ....	50
<b>Scheme 9.</b> Preparation of phenol <b>9e</b> from methoxy benzaldehyde <b>18</b> . ....	51
<b>Scheme 10.</b> Initial preparation of <b>5a</b> and <b>5c</b> . ....	<b>53</b>
<b>Scheme 11.</b> Mechanism of reaction of AMC <b>3</b> and triphosgene <b>19</b> to prepare isocyanate <b>6</b> . ....	55
<b>Scheme 12.</b> Synthesis of an authentic sample of the common impurity methylcarbamate <b>22</b> . ....	55
<b>Scheme 13.</b> Mechanism of carbamate <b>5a</b> formation from benzyl alcohol <b>7a</b> and AMC isocyanate <b>6</b> . ....	57
<b>Scheme 14.</b> Minor reaction of AMC and <b>2</b> forming <b>25</b> . ....	68



## List of Abbreviations

ADCs	Antibody-drug conjugates
ADEPT	Antibody directed prodrug strategy
APs	Alkaline phosphatases
APCI	Atmospheric pressure chemical ionization
APT	Attached proton test
Ar-OSO <sub>2</sub> NH <sub>2</sub>	Phenol sulfamates
ARS	Arylsulfatase
ARSA	Arylsulfatase A
ARSB	Arylsulfatase B
ARSC	Arylsulfatase C
Aq	Aqueous
Cat	Cathepsin
CDCl <sub>3</sub>	Deuterated chloroform
CDOD <sub>3</sub>	Deuterated methanol
Ces1C	Carboxyesterase 1C
Cit	Citrulline
CDRs	Complementary determining regions
d	Doublet
DAR	Drug-to-antibody ratio
DBU	1,8-Diazabicyclo[5.4.0]undec-7-ene
DCM	Dichloromethane
dd	Doublet of doublets
ddd	Doublet of doublets of doublets
DIPEA	N,N-Diisopropylethylamine
DMNB	4,5-dimethoxy-2-nitrobenzyl
DMF	Dimethylformamide
DMSO	Dimethyl sulfoxide
DNA	Deoxyribose nucleic acid
dt	Doublet of triplets
d <sub>6</sub> -DMSO	Hexadeutero-dimethylsulfoxide
ED <sub>50</sub>	Effective dose
EtOAc	Ethyl acetate
Et <sub>2</sub> O	Diethyl oxide
Et <sub>3</sub> N	Triethyl amine
eq.	Equivalents

Fab	Fragment antigen binding
Fc	Fragment crystallisable
FGly	Formylglycine
FGE	Formylglycine generating enzyme
FGH	Formylglycine hydrate
g	gram
GalN6S	Glucosamine-2-sulfatase
GAGs	Glycosaminoglycans
GlcA2S	Glucuronate-2-sulfatase, Arylsulfatase K
GlcN3S	Glucosamine-3-sulfatase, Arylsulfatase G
GlcN6S	<i>N</i> -sulfogalactosamine-6-sulfatase
Gly	Glycine
GSH	Glutathione
HBr	Hydrobromic acid
HER2	Human epidermal growth factor receptor 2
HHz	Megahertz
HMCDs	Heptamethine cyanine dyes
HMBC	Heteronuclear multiple bond correlation
HRMS	High resolution mass spectrometry
HSQC	Heteronuclear single quantum coherence
IC <sub>50</sub>	Half-inhibitory concentration
IdoA2S	Idurinate-2-sulfate
Ig	Immunoglobulin
IR	Infrared
<i>J</i>	Coupling constant
K <sub>m</sub>	Binding affinity
KOt-Bu	Potassium tert-butoxide
LOD	Limit of detection
LOQ	Limit of quantification
Lys	Lysine
LRMS	Low resolution mass spectrometry
m	Multiplet
M	Molar
mAbs	Monoclonal antibodies
mc	Maleimidocaproyl
MED	Minimum effective dose
MeOH	Methanol

MeOTf	Methyl trifluoromethanesulfonate
mL	Millilitre
mM	Millimolar
mmol	Millimole
MMAE	Monomethylauristatin E
MMAF	Monomethylauristatin F
m.p.	Melting point
MSD	Multiple sulfatase deficiency
MTD	Maximum tolerated dose
MUFS	4-methylumbelliferyl
<i>m/z</i>	Mass to charge ratio
M+	Molecular ion
NaBH <sub>4</sub>	Sodium borohydride
NaH	Sodium Hydride
NaHMDS	Sodium bis(trimethylsilyl)amide
NHS	<i>N</i> -hydroxysuccinimide
NaN <sub>3</sub>	Sodium azide
nm	Nanometres
nM	Nanomolar
NMR	Nuclear magnetic resonance
PAB	<i>para</i> -aminobenzyl
PABC	<i>para</i> -aminobenzyl carbamate
PBD	Pyrrdobenzodiazepine
Pd/C	Palladium on carbon
PEG	Polyethyleneglycol
Phy	Phenylalanine
<i>p</i> NCS	<i>para</i> -nitrocatechol
PtO <sub>2</sub> /H <sub>2</sub>	Platinum dioxide hydrogen
Pyridine/SO <sub>3</sub>	Pyridine sulfur trioxide complex
quat.	Quaternary
rt	Room temperature
s	Singlet
SAR	Structure activity relationship
SGSH	<i>N</i> -sulfoglucosamine sulfhydrolase
SMCC	Succinimidyl-4-( <i>N</i> -maleimidomethyl) cyclohexane-1-carboxylate

Sulf1/2	Sulfatase 1/2
SYD985	[vic-]trastuzumab duocarmazine
t	Triplet
TCE	Trichloroethyl
TD <sub>50</sub>	Toxic dose
TFE	Trifluoroethyl
THF	Tetrahydrofuran
TLC	Thin layer chromatography
Top I	Topoisomerase I
Tris	Trisaminomethane
T <sub>1/2</sub>	Half life
UV	Ultraviolet
Val	Valine
V <sub>max</sub>	Maximum rate
w/w	Weight for weight
X <sub>4</sub>	Petroleum ether, boiling fraction 40 – 60 °C
<i>β</i> -gal	<i>β</i> -galactosidase
°C	Degrees Celsius
$\lambda$	Wavelength
$\lambda_{em}$	Emission wavelength
$\lambda_{ex}$	Excitation wavelength
$\delta_H$	Chemical shift (proton)
$\delta_C$	Chemical shift (carbon)
$\mu\text{L}$	Microlitre
4-DMAP	4-Dimethylaminopyridine

# Chapter 1: Introduction

# 1. Introduction

## 1.1 Cancer Chemotherapy

Cancer is the second leading cause of death worldwide, accounting for one in six deaths (1). Cancer does not constitute one disease but comprises over 200 conditions characterised by genetic changes leading to uncontrolled cell growth and proliferation. Traditionally, cancer treatment has relied on small-molecule chemotherapy in combination with surgery and radiotherapy (2). As cancer develops from healthy cells, differentiating between healthy and cancerous cells is inherently difficult. Antiproliferative small molecules used in chemotherapy aim to exploit rapid proliferation to disproportionately impact cancers by killing replicating cells. However, healthy replicating cells are also killed, causing severe adverse effects.

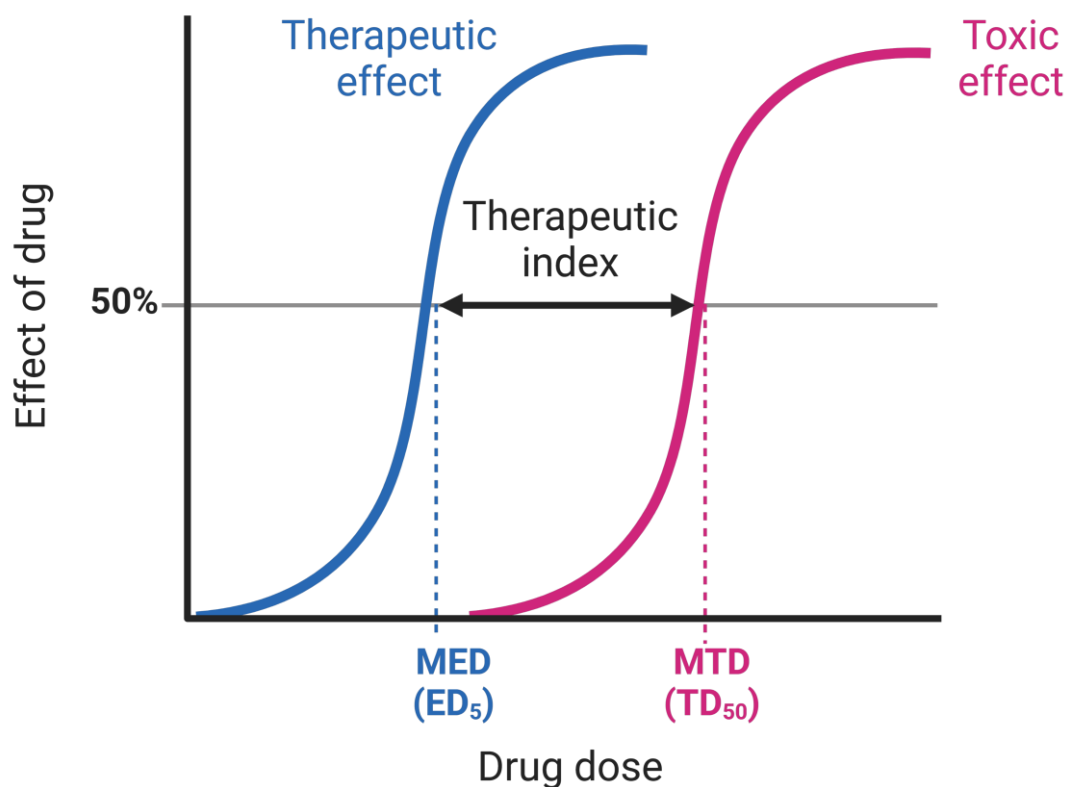


**Figure 1.** Dose-response curve depicting therapeutic index. Therapeutic effect is represented by the blue line, and toxic effect is represented in red. The MED is defined as the ED<sub>50</sub>, the dose to which 50% of patients have an effective response. The MTD is defined by the TD<sub>50</sub>, the dose in which 50% of patients experience dose-limiting toxicity. Created with Biorender.com.

Therapeutic index is defined as the ratio between the minimum effective dose (MED), and the maximum tolerated dose (MTD) (**Figure 1**); this reflects a treatment's safety. The therapeutic

index of traditional chemotherapies is low, and their accompanying adverse effects are notoriously debilitating. The development of new therapies strives to achieve wider therapeutic indexes to provide safe, efficacious, and well-tolerated treatments for patients.

## 1.2 Antibodies

The aim of targeted therapies is to achieve a wider therapeutic index through greater selectivity. Recent advances in biotherapies, such as monoclonal antibodies (mAbs), have achieved selectivity greater than small molecules alone (3,4). Antibodies are large (~150 kDa) Y-shaped glycoproteins belonging to the immunoglobulin (Ig) superfamily. Produced by B-cells, antibodies recognise and bind foreign antigens and recruit immune cells as a part of the adaptive immune system. Antibodies are comprised of two heavy chain and two light chain polypeptides held in a Y-shape by disulfide bonds and extensive non-covalent interactions. Their structure may be sub-categorised into the Fab (fragment antigen binding) and Fc (fragment crystallisable) regions (**Figure 2**). The Fab regions are each comprised of a pair of constant and variable domains, the latter containing the complementary determining regions (CDRs). The CDRs are encoded to correspond to a specific antigen epitope, facilitating selective antigen recognition and binding.

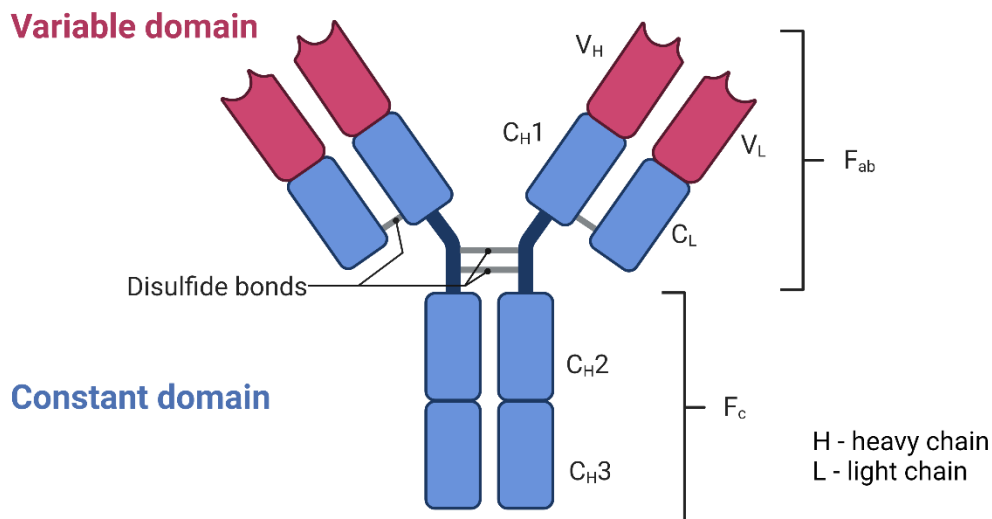


**Figure 2.** Structure of an antibody. Created with BioRender.com.

mAbs are antibodies derived from cloned B-cells. mAbs have become a major class of cancer therapy, due to their outstanding selectivity and long circulatory half-lives, a well-recognised example being the anti-human epidermal growth factor receptor 2 (HER2) mAb trastuzumab

## Introduction

(3,5). Generally, mAb therapies are well tolerated, and adverse effects are clinically manageable (6). The first therapeutic mAbs were murine molecules and once recognised as foreign by the patient's immune system were rapidly cleared. Technological developments have allowed the transition away from murine mAbs towards fully human mAbs has minimised the risk of these events (6). The extended half-lives of mAbs allow effective plasma concentrations to be maintained with infrequent dosing. Renal elimination of antibodies is insignificant as their molecular weight is higher than the glomerular filtration threshold (55 kDa). Instead, antibodies are eliminated through target specific or non-specific (pinocytosis) uptake and subsequent proteolysis within lysosomes. Antibodies that undergo non-specific uptake may be recycled back into circulation by recognition of the Fc regions by Fc receptors within the endosome, protecting them from lysosomal degradation and lengthening their circulatory half-life. Despite their selectivity, mAbs are often limited by a lack of antitumour efficacy (**Figure 3**) (7). Due to their large molecular size, mAbs suffer from poor solid tissue penetration. Consequently, the mAbs remain primarily in circulation, with no more than 20% of an administered dose interacting with solid tumours (8). A study of radiolabelled antibodies in patients found these factors limited the number of injected antibodies to accumulate in solid tumours was as little as 0.003-0.008% per gram of solid tumour. Additionally, mAbs are limited to targets expressed as antigens on the cell's surface. Finally, the highly selective nature of mAbs limits efficacy against a varied and adaptable target like cancer. Tumours are typically heterogenous mixtures; consequently, only some tumour cells will be sensitive to the therapy, and resistance can quickly develop (7,9).

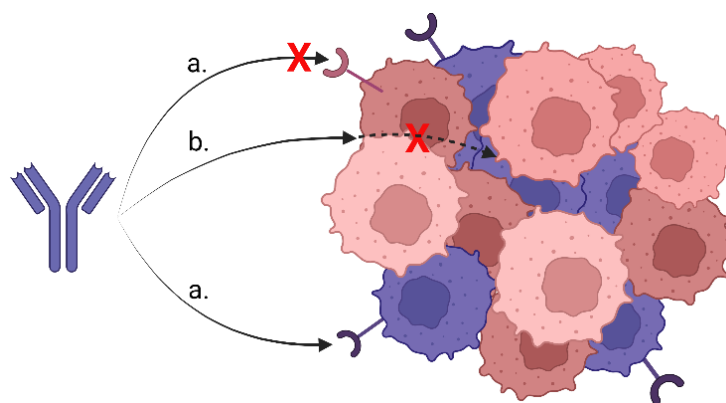


**Figure 3.** Limitations of monoclonal antibodies against solid tumours. **a.** mAbs only affect antigen positive cells in heterogenous tumours. **b.** Poor tissue penetration protects antigen positive cells in the tumour mass. Created with BioRender.com.

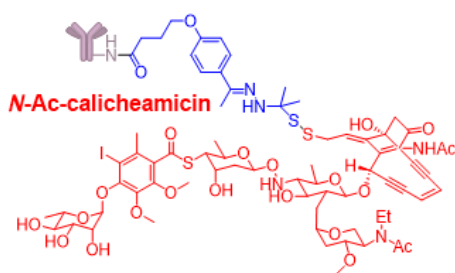


### 1.3 Antibody-Drug Conjugates

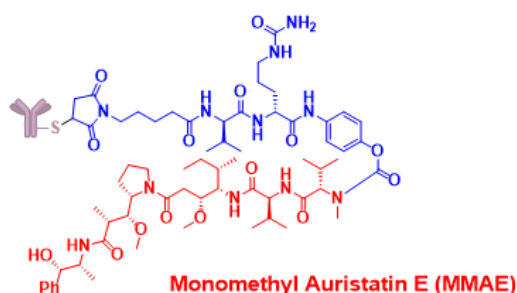
Antibody-Drug conjugates (ADCs) are a rapidly emerging class of powerful, targeted biopharmaceuticals comprised of a mAb and cytotoxic small molecule “payloads” attached via chemical linkers (**Figure 4**) (10,11). Typically, several of the same drug-linker moieties are attached to the same mAb defining the drug-to-antibody ratio (DAR). This strategy aims to combine the outstanding selectivity and convenient pharmacokinetic profile of mAbs as delivery vehicles for extremely potent cytotoxic small molecule chemotherapies. To date, most ADC development has been targeted towards cancer, although other targets, such as infectious bacteria, have been investigated (12). The use of mAbs as delivery vehicles is not novel. Investigation into the three components of ADCs began in the 1980s, ultimately leading to the first in class approval of gemtuzumab ozogamicin in 2001 (13). However, the following 15 years of development saw only limited success. Gemtuzumab ozogamicin was removed from the market in 2010 due to a lack of efficacy and increased morbidity, while drentuxumab vedotin and Ado-trastuzumab emtansine achieved approval in 2011 and 2013 respectively (14–16). Despite slow progression, interest in ADCs remained high, and following the developments in mAbs, payloads and linker technologies the field has recently matured into a major treatment class. Currently, there are 11 FDA-approved ADCs (**Figure 4**), including gemtuzumab ozogamicin, reinstated in 2017 under a new dosing regimen, and more than 80 examples are currently in clinical development (10,16–20). However, this success has not been without its setbacks. Belantamab mafoditon-blmf was given fast track approval by the FDA in 2020 for treating multiple myeloma (21) but was recently removed from the market due to a lack of clinical efficacy (22). Indeed, there is no one-size-fits-all strategy for ADC success, and significant development is still required for this emerging class of targeted therapies.

## Introduction

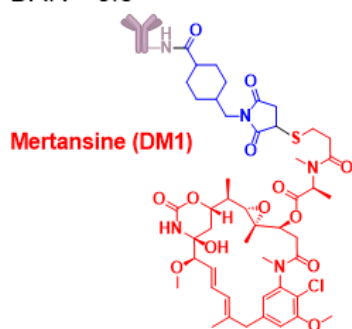
Gemtuzumab – Mylotarg® (2000)  
 DAR = 3  
 Inotuzumab – Besponsa® (2017)  
 DAR = 6



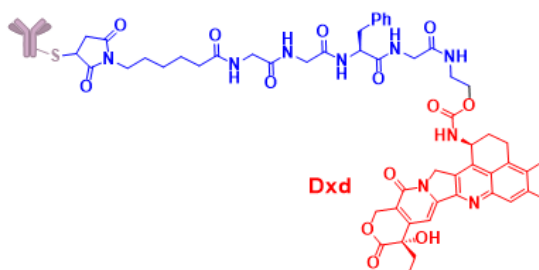
Brentuximab – Adcetris® (2011) DAR = 4  
 Polatuzuman – Polivy® (2019) DAR = 3.5  
 Enfortumab – Padcev® (2019) DAR = 3.8  
 Tisotumab – Tivdak® (2021) DAR = 4



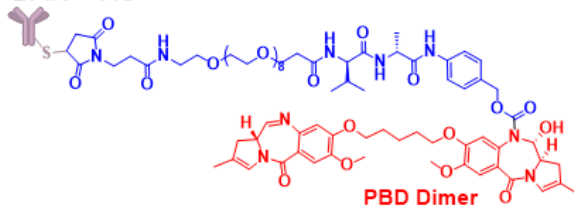
Trastuzumab – Kadcyła® (2013)  
 DAR = 3.5



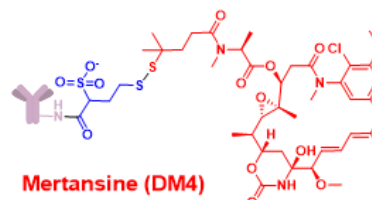
Trastuzumab – Enhertu® (2019)  
 DAR = 8



Sacituzumab – Trodelvy® (2020)  
 DAR = 7.6



M9346A - Elahere® (2022)  
 DAR = 3.5



Loncastuximab – Zylonta® (2021) DAR = 2.3

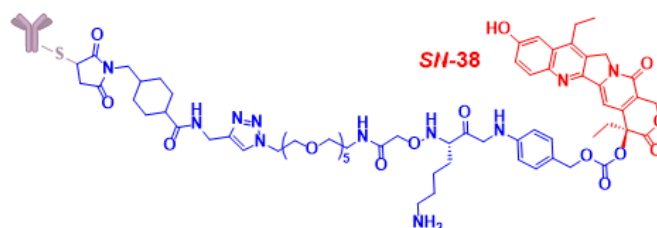


**Figure 4.** Chemical structures of the 11 clinically approved antibody drug conjugate drug linkers. Antibodies, trade names and approval dates and DAR are listed above. Linkers are illustrated in blue, and payloads and their names are in red. Gemtuzumab ozogamicin (Mylotarg®), inotuzumab ozogamicin (Besponsa®), brentuximab vedotin (Adcetris®), polatuzumab vedotin (Polivy®), enfortumab vedotin (Padcev®), tisotumab vedotin (Tivdak®), trastuzumab emtansine (Kadcyla®), sacituzumab govitecan (Trodelvy®), mirvetuximab soravtansine-gynx (Elahere®), loncastuximab tesirine (Zylonta®).

### 1.3.1 Mechanism of Action of ADCs

ADCs mechanism of action can be divided into two classes, one requiring internalisation and one where activity is derived from the extracellular release of the payload. For most ADCs, antigen binding triggers endocytosis in which the ADC-antigen complex is internalised and subsequently trafficked into lysosomes (**Figure 5**) (11). Within lysosomes proteolytic enzymes degrade the mAb into its constituent amino acids, freeing the drug-linker. The low pH and high concentration of hydrolytic enzymes unique to the lysosomes are used to trigger linker cleavage and subsequent payload release. In some cases, the payload may then diffuse into and affect neighbouring cells. Unlike mAbs, this “bystander effect” allows ADCs to affect antigen negative cells in heterogenous tumours. An alternative non-internalising mechanism of action has also been explored (23,24). In this case, linker cleavage and payload release is triggered extracellularly in the tumour microenvironment. This mechanism potentially improves activity towards tumours with heterogenous antigen expression and allows a broader range of antigens to be targeted. Extracellular release may, however, lead to lower cancer selectivity. To date, no ADCs employing a non-internalising mechanism have achieved clinical approval.

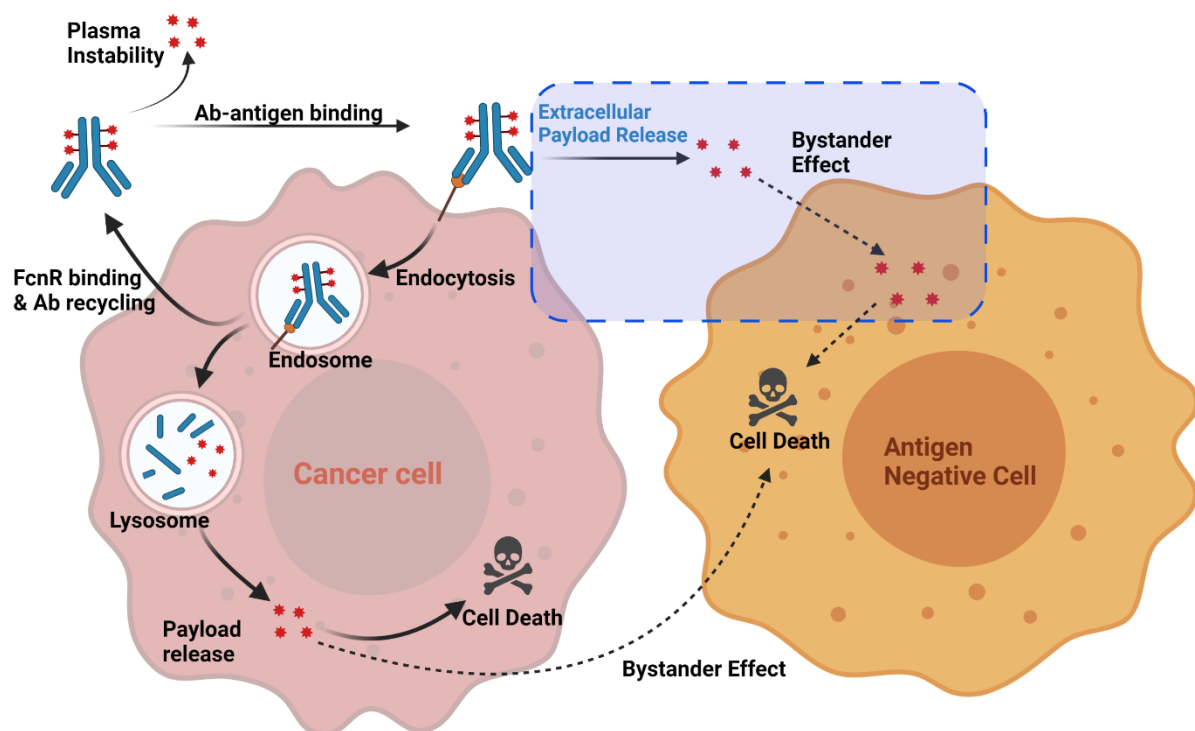


**Figure 5.** Antibody-Drug Conjugate Mechanism of action. An extracellular mechanism is highlighted in blue. Created with BioRender.com.

### **1.3.2 Considerations in ADC design**

Over 40 years of research have produced insight into what makes a successful ADC, revealing the desirable characteristics of each key structural components, the mAbs, payload, and linker and corresponding drug-to-antibody ratio and hydrophobicity of the conjugate. These components are discussed in detail below.

#### **1.3.2.1 Monoclonal antibody characteristics in ADC design**

The properties of mAbs influence the safety, efficacy, and pharmacokinetics of the ADCs they are applied to (25). The important properties of mAbs for ADCs are their; target antigen, size, binding affinity, immunogenicity, and available functionalities for bioconjugation. Antibodies are extremely selective for their target antigen; therefore, the success of an ADC, like therapeutic antibodies, depends on the high expression of the target antigen on the surface of cancer cells compared to healthy cells (25). IgG antibodies represent the vast majority of mAbs used in ADCs; however, their large size contributes to poor tissue penetration. Smaller antibody formats and even antibody fragments have been explored, although they have proven inferior to their IgG counterparts. All currently approved ADCs employ IgG antibodies. Tissue penetration can be improved by using antibodies with lower binding affinities. High affinity, rapidly internalised antibodies bind to antigens on cells closest to the tumour vasculature. In contrast, antibodies with higher antigen dissociation rates have more opportunity to penetrate deeper into solid tumours before being internalised (26). ADC antibodies should be non-immunogenic. The first ADCs employed murine-mAbs that elicited a strong immune response, producing antibodies against the ADC, reducing efficacy and causing immune-related toxicities (25). Consequently, non-immunogenicity is an important criterion in gaining regulatory approval for ADCs (27). Development of new ADCs now utilises humanised or fully human mAbs (6,25). Finally, mAbs must have suitable functionalities as handles for conjugation to drug-linkers. Originally, the reactivity of natural amino acids was employed for conjugation; however, these techniques are difficult to control. Alternative approaches include using engineered antibodies with built-in functionalities for more controlled conjugation at the risk of being identified as foreign (**Section 1.5.2.2**).

### 1.3.2.2 Payload characteristics in ADC design

Drugs employed as ADC payloads bypass the stringent safety and pharmacokinetic parameters of small molecule therapies, allowing extremely potent drugs without suitable TI for systemic distribution to be used (28). Due to the poor tissue penetration of ADCs and the limited number of antigens expressed on the cell surface (typically  $\sim 10^5$ ), high potency is essential for ADC payloads as the quantity reaching the target is low. However, potency alone does not satisfy the criteria for a successful payload. ADC payloads must be metabolically stable in circulation to survive the extended circulatory half-lives of the conjugate and must contain a chemical handle capable of being attached to the linker moiety. Ideally, these payloads will lack susceptibility to multidrug resistance protein 1 mediated efflux, a common mechanism of resistance to ADCs (17,29). Most ADC payloads are highly hydrophobic, contributing to increased clearance and limiting the achievable DAR, (discussed in **Section 1.3.2.4**). Therefore, payload optimisation often favours decreased hydrophobicity.

### 1.3.2.3 Linker characteristics in ADC design

The characteristics of the linker are vital to the success of ADCs as they influence selectivity, efficacy, and pharmacokinetics (30,31). Ideal ADC linkers must be highly stable in circulation to avoid non-specific payload release and toxicity. At the same time, the linker must efficiently release the payload following antibody-antigen binding. ADC linkers are categorised into non-cleavable linkers, which release their payload with an additional charged appendage following antibody degradation in lysosomes, and cleavable linkers, which release the unmodified payload when specific conditions are met (see **Section 1.5.2**) (30). Enzyme-cleavable linkers are a class of cleavable linkers that employ lysosomal enzymes to trigger payload release (see **Section 1.5.3**) and are now the most common linkers in ADC development. Finally, the contribution from the linker to hydrophobicity can be detrimental to ADCs (see **Section 1.3.2.4**), therefore employing linkers with low hydrophobicity is ideal.

### 1.3.2.4 Drug to antibody ratio and hydrophobicity

Given the limited number of antigens expressed on the cell's surface (typically  $\sim 10^5$ ), and the low number of mAbs which actually interact with solid tumours (**Section 1.2, Figure 3**) multiple of the same drug-linker are bound to each antibody to improve delivery efficiency (17,32,33). Maximising the DAR improves the potency of the delivery vehicle *in vitro*;

however, this is not necessarily reflected *in vivo* (34). Instead, increasing the DAR past a certain point becomes detrimental to the pharmacokinetics of the conjugate, reducing its efficacy *in vivo*. The addition of each drug-linker increases the hydrophobicity of the conjugate, causing antibody aggregation and increasing clearance. Ultimately, the hydrophobicity of many established drug-linkers limits the ideal DAR to between three and four (**Figure 4**). The use of less hydrophobic drug-linkers allows higher DARs to be achieved without promoting clearance or aggregation, thereby allowing the higher *in vitro* efficacy of high DAR analogues to be reflected in *in vivo* experiments (32). The recently approved ADCs trastuzumab deruxtecan (Enhertu ®, 2019) and sacituzumab govitecan (Trodelvy ®, 2020) have both achieved exceptional efficacy with DARs >7 carrying the camptothecin payloads Dxd and SN-38 respectively which are less hydrophilic and less potent than other ADC payloads (35,36) (**Section 1.4.4**).

### 1.4 Payloads

Moderately cytotoxic payloads such as methotrexate and doxorubicin were employed in the early development of ADCs (37,38). However, the combination of limited expression of antigens on a cell's surface and, along with inefficiency in internalisation and payload release resulted in these low potency payloads providing insufficient therapeutic benefit. Indeed only a small proportion of injected mAbs interact with solid tumours (**Section 1.2**), while the real number of ADCs internalised is expected to be lower than the ADCs which bind to the target cells surface (28,39). Subsequently, payloads for ADCs have shifted to highly potent cytotoxins with nano-molar to high-femtomolar  $IC_{50}$ s (**Figure 6**). Generally, ADC payloads can be categorised into microtubule-disrupting agents (auristatins and maytansinoids) and DNA-damaging agents (calicheamicins, topoisomerase I inhibitors, duocarmycins and pyrrolobenzodiazepine dimers).

## Introduction

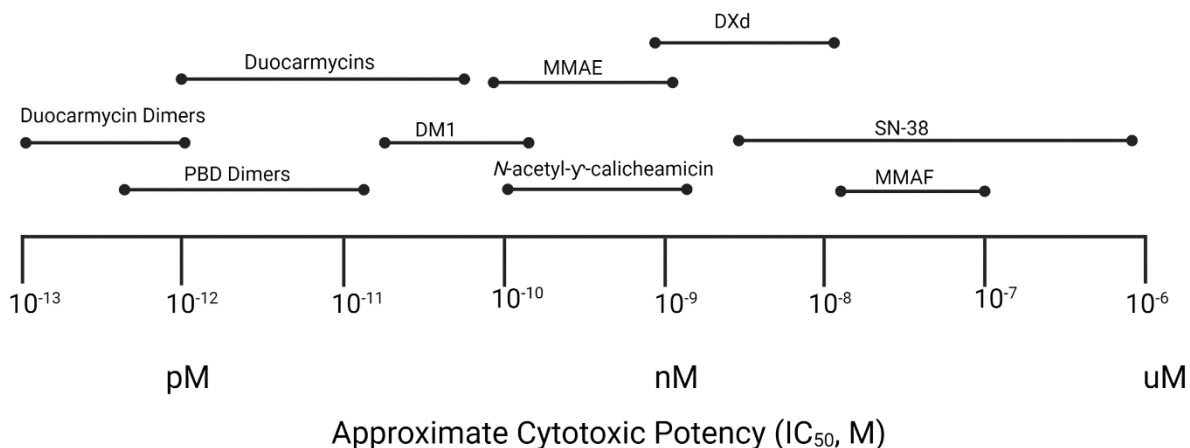


**Figure 6.** Comparison of cytotoxicity of reported ADC payloads. Auristatins MMAE and MMAF (40,41), DM1 (42), N-acetyl- $\gamma$ -calicheamicin (43), Dxd (44), SN-38 (44,45), Duocarmycins (46,47), PBD dimers (48), and Duocarmycin dimers (46). Adapted from (49). Created with Biorender.com.

### 1.4.1 Auristatins

Auristatins are analogues of a cytotoxic marine natural product, dolastatin 10 (50) (**Figure 7**). These cytotoxins inhibit microtubule assembly at high pico-nanomolar concentrations, causing metaphase arrest and apoptosis (40,51). Clinical evaluation of dolastatin 10 and other auristatin analogues failed to achieve significant activity in patients at tolerated doses when employed as a single agent. Interest in auristatins moved to application as ADC payloads to improve their therapeutic index. Structure-activity relationship (SAR) studies of dolastatin 10 identified monomethylauristatin E (MMAE) and F (MMAF) as potent and stable analogues with appropriate handles for conjugation (**Figure 7**) (40,52). MMAE payloads have been approved in brentuxumab vedotin, polatuzumab vedotin-piiq, enfortumab-vedotin-ejfv, and tisotumab - vedotin-tftv. MMAF payloads originally found clinical approval in belantamab mafoditin, however, this was recently removed from the market due to a lack of efficacy. Given their clinical success auristatins make up a large portion of ADC payloads in ongoing clinical trials (10).

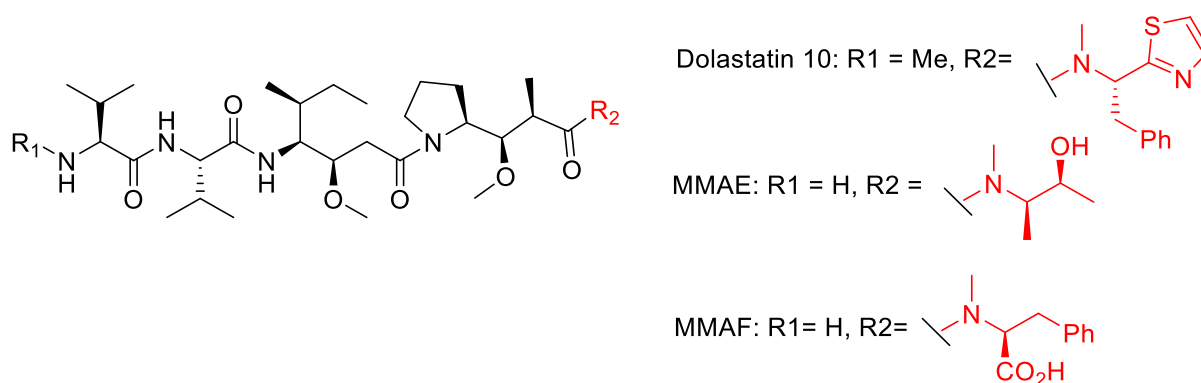


**Figure 7.** Structure of Auristatin analogues Dolastatin 10, MMAE and MMAF.

### 1.4.2 Maytansinoids

Maytansinoids are a class of potent tubulin inhibitors derived from the natural product maytansine (**Figure 8**). Maytansine is a 19-member lactam structure originally isolated from an Ethiopian shrub *Maytenus ovatus* (53). Maytansinoids inhibit microtubule assembly by binding tubulin, causing mitotic arrest with sub-nanomolar potency making them interesting candidates as anticancer drugs. Despite its potency, maytansine failed in clinical trials due to severe toxicity caused by poor selectivity (54). Interest in Maytansinoids as ADC payloads began in the 1980s. Thiol derivatives DM1, DM3, and DM4 were developed, allowing conjugation to a linker via a thiosuccinimide or disulfide linkage (**Figure 8**) (42). Each analogue presents varied steric bulk around the thiol moiety, adjusting linker stability and antitumour activity; thus, the payload can be optimised for the ADC it is applied to. Ado-trastuzumab emtansine employs a DM1 payload conjugated to the anti-HER2 antibody trastuzumab (15).

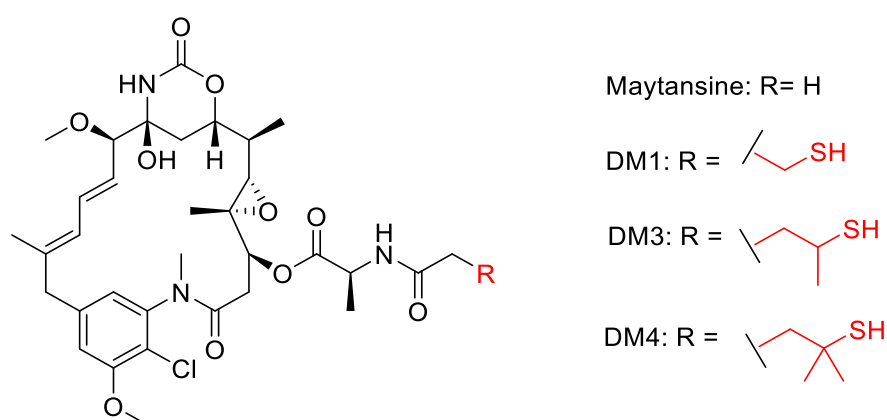


**Figure 8.** Structure of Maytansinoid analogues Maytansine, DM1, DM3, and DM4.



### 1.4.3 Calicheamicins

Calicheamicins are a class of cytotoxin derived from *Micromonospora echinospora* (**Figure 9**) (43,55). These cytotoxins bind the DNA minor groove causing strand breaks via the formation of a reactive diradical species. Preclinical evaluation of calicheamicin  $\gamma_1^I$  reported potent picomolar activity however, poor selectivity and subsequently poor therapeutic index shifted attention to development as ADC payloads. Two approved ADCs (Gemtuzumab ozogamicin and Inotuzumab ozogamicin) employ calicheamicin derivatives (56), however, there is relatively little use of these payloads in the development of new ADCs, presumably due to their complicated and expensive synthesis.

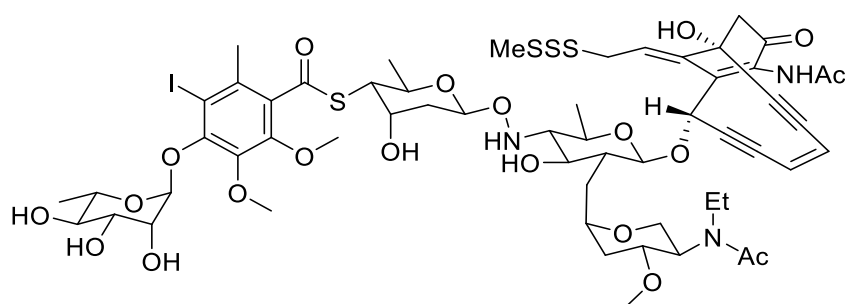


**Figure 9.** Structure of calicheamicin.

### 1.4.4 Topoisomerase I inhibitors

Camptothecin analogue topoisomerase I (Top I) inhibitors Dxd and SN-38 (**Figure 10**) are employed in the approved ADCs trastuzumab deruxtecan and sacituzumab govitecan respectively (35,36). During DNA replication, Top I binds and cleaves DNA forming a Top I-DNA complex (57), this allows rotation of the cleaved strand around the helix, preventing DNA supercoiling. Top I then re-ligates the broken strand reforming the double helix. Top I inhibitors such as Dxd and SN-38 bind the TopI-DNA complex, preventing strand re-ligation and initiating apoptotic cell death. While less potent than other ADC payloads (44,45) (SN-38  $IC_{50} = 1-6$  nM, Dxd  $IC_{50} = 0.1$  nM, **Figure 6**), these payloads are considerably less hydrophobic allowing more drug-linker moieties to be loaded onto each antibody without causing aggregation. Both trastuzumab deruxtecan and sacituzumab govitecan achieve DAR >7, significantly greater than the average of 3-4 for other approved ADCs (**Figure 4**).

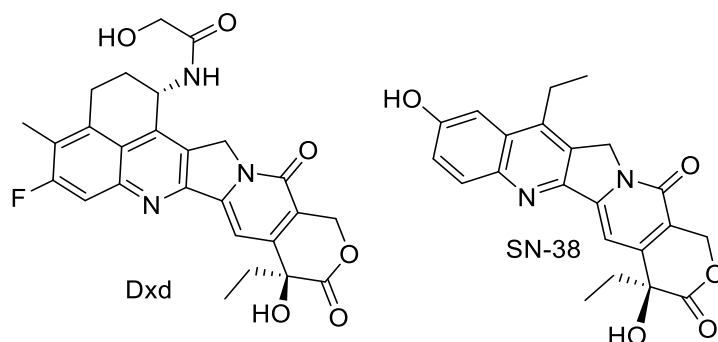


**Figure 10.** Structures of Top1 inhibitors Dxd (**left**) and SN-38 (**right**) employed in trastuzumab deruxtecan and sacituzumab govitecan respectively.

#### 1.4.5 Pyrrolobenzodiazepine dimers

Pyrrolobenzodiazepine (PBD) dimers are potent DNA alkylators based on the naturally occurring anthramycin PBD monomers (**Figure 11**) (58). These PBD dimers bind guanine residues in the DNA minor groove to form inter- or intra-strand cross-links, halting DNA replication and initiating apoptosis. These dimers are attractive for several reasons. They are synthetically straightforward, offer a novel mechanism of action compared to other ADC payloads, and are among the most potent cytotoxins available for ADCs achieving picomolar  $IC_{50}$  *in vitro* (48). As a result, PBD dimers have recently found extensive use in ADC development, reaching clinical approval in 2021 with loncastuximab tesirine (18,59,60).

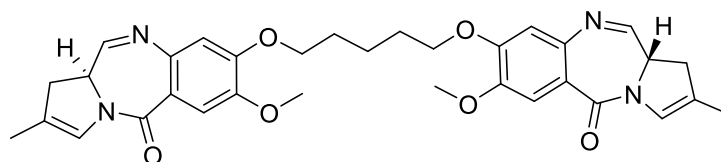


**Figure 11.** PBD dimer SG3199 employed by loncastuximab tesirine.

#### 1.4.6 Duocarmycins

Duocarmycins (**Figure 12**) are a class of potent DNA alkylators that bind adenine residues, causing double-strand DNA breaks and inducing apoptosis in both replicating and non-replicating cells (61). In clinical investigation of various duocarmycins as single agents, all caused severe adverse effects and failed to establish a therapeutic index (62,63). While not suitably selective for systemic therapy, their novel mechanism of action, potent picomolar cytotoxicity in preclinical studies, and potential to be turned into symmetrical dimers make them attractive payloads for ADCs (47,64). Similar to PBDs duocarmycin dimers achieve high-

femtomolar single agent cytotoxicity *in vitro* (**Figure 6**). However, duocarmycins have received less attention due to the success of the mechanistically related PBDs (**Section 1.4.3**). Recently, the investigational ADC [vic-]trastuzumab duocarmazine (SYD985) comprised of the trastuzumab, cleavable linker, and a duocarmycin payload was approved for fast-track designation by the FDA and is currently in advanced clinical trials (65–67). Interestingly, SYD985 is effective against breast cancers which have developed resistance to the anti-HER2 trastuzumab emtansine (66) and unlike trastuzumab emtansine, is able to induce a bystander effect. ADCs carrying duocarmycin dimer payloads have also been explored and have so far reported promising preclinical results *in vivo* (47,64).

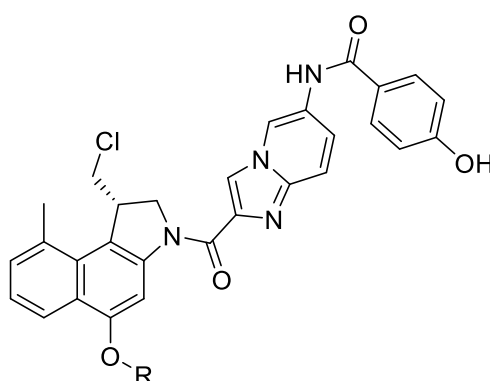


**Figure 12.** Structure of duocarmycin payload of SYD985. R = conjugation site, payload released as a phenol (R= H).

#### 1.4.7 Duocarmycin-PBD heterodimers

Given the success of symmetrical PBD dimers, and the potential for duocarmycin dimers, duocarmycin-PBD heterodimers have also been explored (61,68). These heterodimers form cross-links between adenine and guanine residues in a sequence specific manner at 5'-Cys-Ala-Ala-Thr-Thr-Ala\*-3', the 5'-cysteine provides a complementary guanine for the PBD unit to bind and the 3'-adenine (\*) is alkylated by the duocarmycin unit. These dimers are picomolar cytotoxins in human cancer cell lines *in vitro* (69). There is only one report of *in vivo* antitumour activity of these heterodimers. The heterodimer (**Figure 13**) produced a significant growth delay at its maximum tolerated dose (69). The lack of development of these payloads may be due to their more challenging synthesis versus symmetrical dimers. More examples of the class and insight into their *in vivo* antitumour activity and safety profile are required to clarify if this class offers an advantage over their symmetrical counterparts.

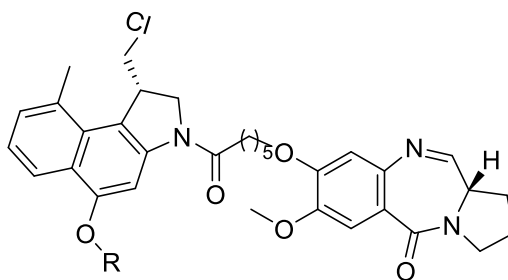


**Figure 13.** Structure of a duocarmycin-PBD dimer.

#### 1.4.8 Non-cancer drugs

The potential of ADCs extends beyond their use as cancer therapies. Indeed, the development of ADCs targeting other indications has already begun. ADCs DSTA4637A and ABBV-3373 are in clinical trials carrying small molecule payloads that treat *Staphylococcus aureus* infection and rheumatoid arthritis, respectively (70,71). As the development of ADCs targeting non-cancer indications grows, so too will the range of payloads.

### 1.5 Linkers

The linker is a crucial component of ADCs. The nature of the linker is central to the safety, efficacy, and composition of ADCs (30,72). Linkers have two essential functions, attachment to the mAb, and attachment to the payload. The linker-mAb attachment defines the composition of ADCs and the number of species present in a dose. The drug-linker attachment defines the nature of the active payload and the timing of its release (30). Development of ADC linkers has focused on producing ADCs with homogenous DAR, high stability in plasma and which release an effective payload following target identification. Additionally, development has aimed to actively introduce groups to reduce the hydrophobic character of the ADC, allowing higher DARs to be achieved without modification to established payloads (30).

#### 1.5.1 Homogeneity in bioconjugation

As discussed in **Section 1.3.2.4**, the DAR significantly influences both efficacy and pharmacokinetics of ADCs. The attachment site for each drug-linker to the mAb is just as significant, with preference for a site distal to the CDR so as not to affect antibody binding (**Figure 14**) (73). Additionally, the attachment site influences linker stability and thus should be taken into consideration. Ideally, each individual ADC in a batch would have homogenous DAR and attachment sites (73–75). ADCs varied attachment sites have different physical

## Introduction

properties, pharmacokinetics, and pharmacodynamics, and heterogenous DAR further increases the variability between heterogenous species. For example, DAR populations containing unconjugated antibodies (DAR = 0) suffer from competition between these antibodies and higher DAR ADCs for the limited number of target antigens. At the same time, species at the other end of the DAR distribution may present significantly different pharmacokinetics. Importantly, high DAR is only a liability for hydrophobic drug-linkers as illustrated by the success of the less hydrophobic trastuzumab deruxtecan and sacituzumab govitecan, each achieving DARs >7 (35,45,76). These less hydrophobic ADCs can achieve higher DARs without causing antibody aggregation or clearance.

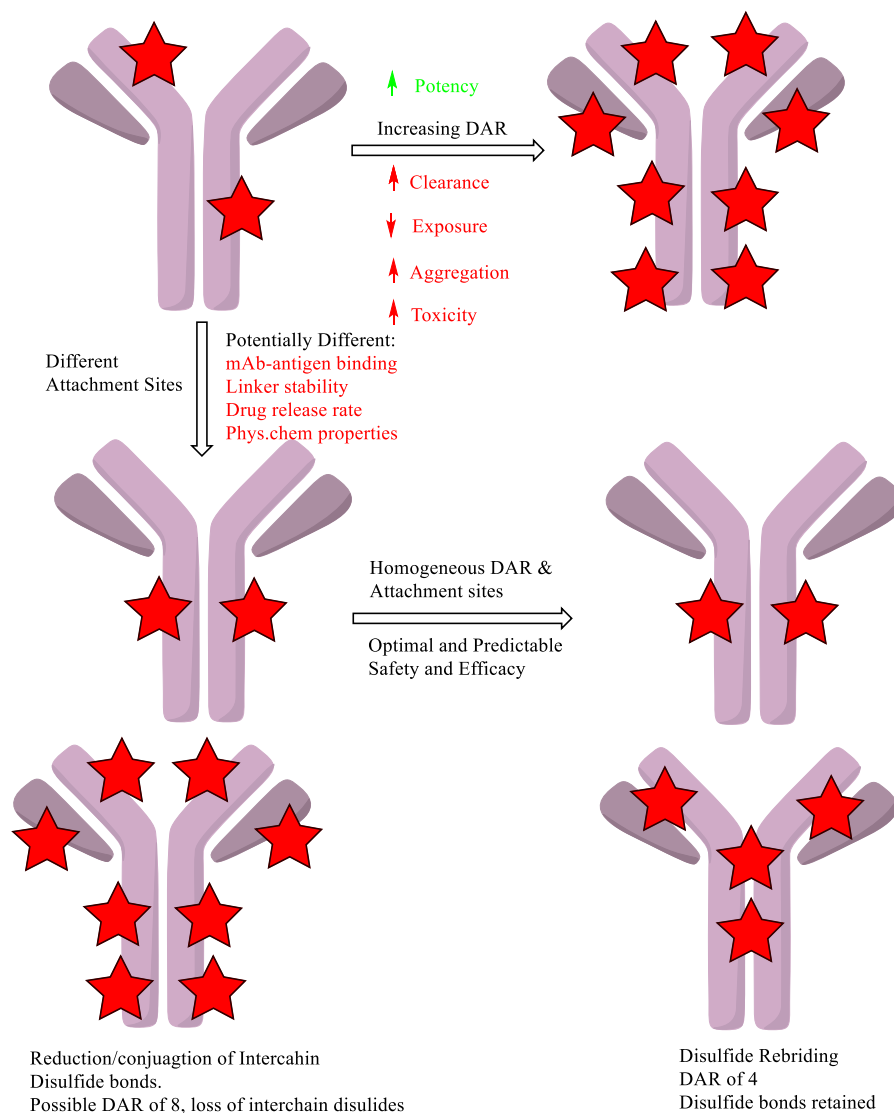


**Figure 14.** Effects of DAR, attachment site and homogeneity on the characteristics of ADCs.

## 1.5.2 Conjugation Methods

### 1.5.2.1 Naturally occurring amino acids

Drug-linkers are conjugated to antibodies through reaction with amino acid side chains (**Figure 15**) (75). There are approximately thirty accessible lysine residues on IgG antibodies for conjugation. When targeting these amino acids, the average DAR of a batch can be controlled by stoichiometry and reaction conditions; however, controlling the conjugation site is impossible. This results in a distribution of DARs and conjugation sites within a batch. A study using the common conjugation motif, *N*-hydroxysuccinimide (NHS)-ester, yielded an ADC mixture containing around 4.5 million different species with DARs ranging from 0-6 (77). Gemtuzumab ozogamicin, ado-trastuzumab emtansine and inotuzumab ozogamicin all employ lysine bioconjugation methods and are administered as heterogeneous mixtures. Highlighting this characteristic, gemtuzumab ozogamicin consists of a remarkable 50% unconjugated mAb with the remaining 50% averaging a DAR of 6 to afford an overall average DAR of ~3 despite almost no species being found at this DAR (13).

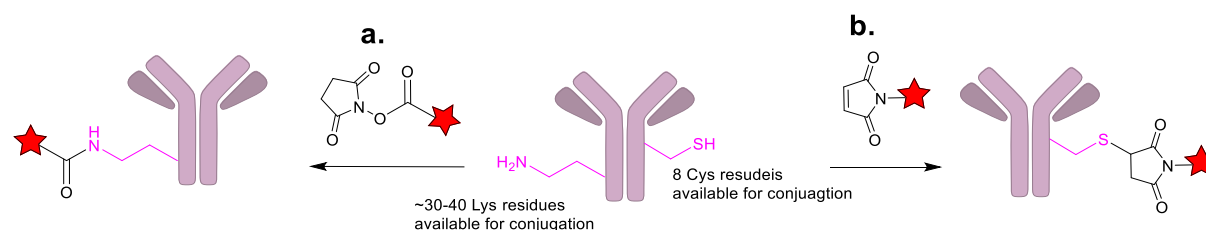


**Figure 15.** Conjugation by **a.** the reaction of NHS-ester reagent with Lysine residues and **b.** the reaction of maleimide reagents with cysteine residues.

Cysteine residues offer a more attractive target for bioconjugation due to their lower natural abundance and unique nucleophilicity among amino acids. The reduction of four interchain disulfide bonds on IgG antibodies unmask eight cysteine residues as reactive thiol species while retaining the antibody's quaternary structure (78). Reaction with soft electrophiles affords a means of selective bioconjugation at these eight sites. However, conjugation of all cysteines would result in a DAR of 8 being too high with many hydrophobic drug-linkers. In this system, DAR is still controlled through stoichiometric bioconjugation chemistry, whereby the quantity of reductants and drug-linker are used to afford a heterogeneous mixture with a controlled average DAR. This method produces ADCs with average DARs of 2-4, although as fewer conjugation sites are available (relative to lysine) a less heterogeneous mixture is

## Introduction

produced (75). Cysteine conjugation is typically mediated *via* a 1,4-conjugate addition to *N*-substituted maleimides. Maleimides are especially attractive reagents due to their synthetic accessibility and mild conjugation conditions. Indeed, most approved and developmental ADCs employ maleimide conjugation chemistry (**Figure 4**). A disadvantage of this technique is that the resulting thiosuccinimide conjugates are liable to a retro-Michael addition in solution to release the payload-linker prematurely (**Figure 16.a**) (79).

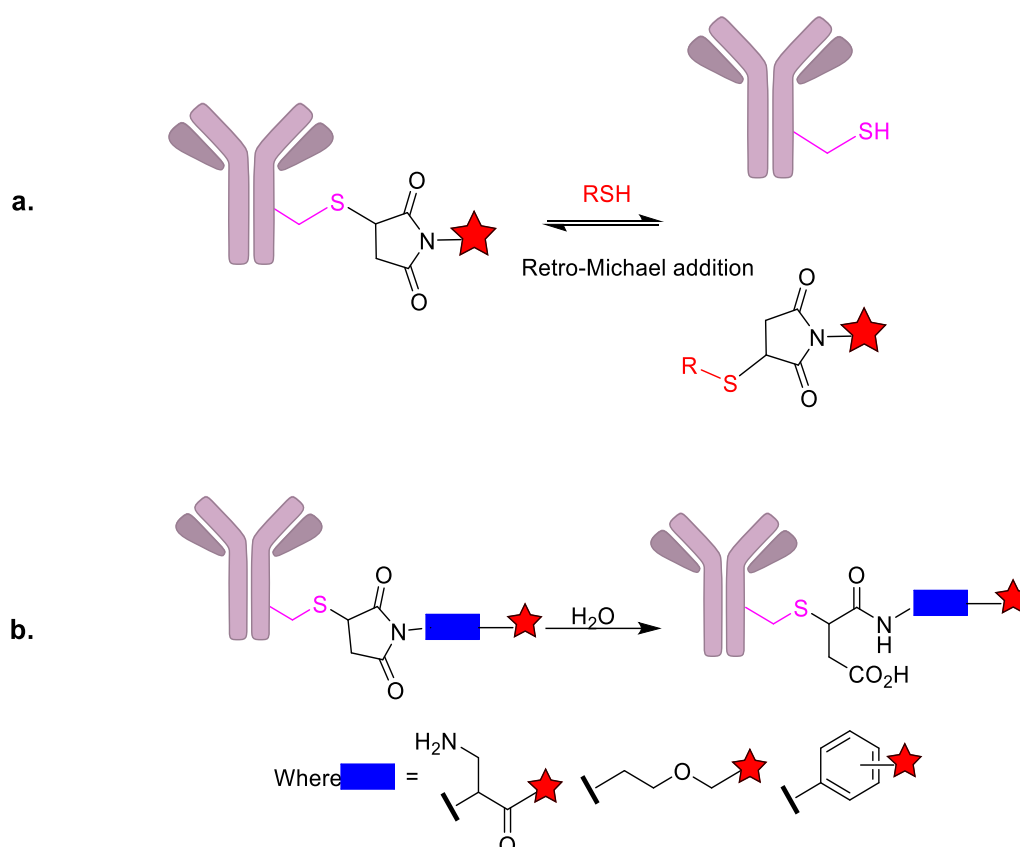


**Figure 16.** Illustration of, and strategies to overcome maleimide linker liabilities **a.** Thiosuccinimide linker retro-Michael addition releases the ADC payload. **b.** self-hydrolysing maleimide linkers form of a product highly stable to payload release, as promoted by nearby amine, PEG or *N*-aryl functional groups (Blue).

This instability can be mitigated by post-conjugation hydrolysis of the thiosuccinimide ring to form a more stable linker (**Figure 16**). A series of rapidly self-hydrolysing maleimides utilising amine, PEG and *N*-aryl functional groups have been described (79–81). Disulfide re-bridging offers a more controlled approach to cysteine conjugation (**Figure 17**). Here interchain disulfide cleavage is followed by reaction with specially designed linkers that participate in new interchain covalent bonds. This method yields highly homogenous products with DARs up to 4 and retains interchain bonds, useful in developing homogeneous ADCs at appropriate

## Introduction

moderate DARs. Several cysteine rebridging agents have been developed, including *bis*-sulfones, dibromomaleimides, divinylpyrimidines, and pyridazinediones (82–85).

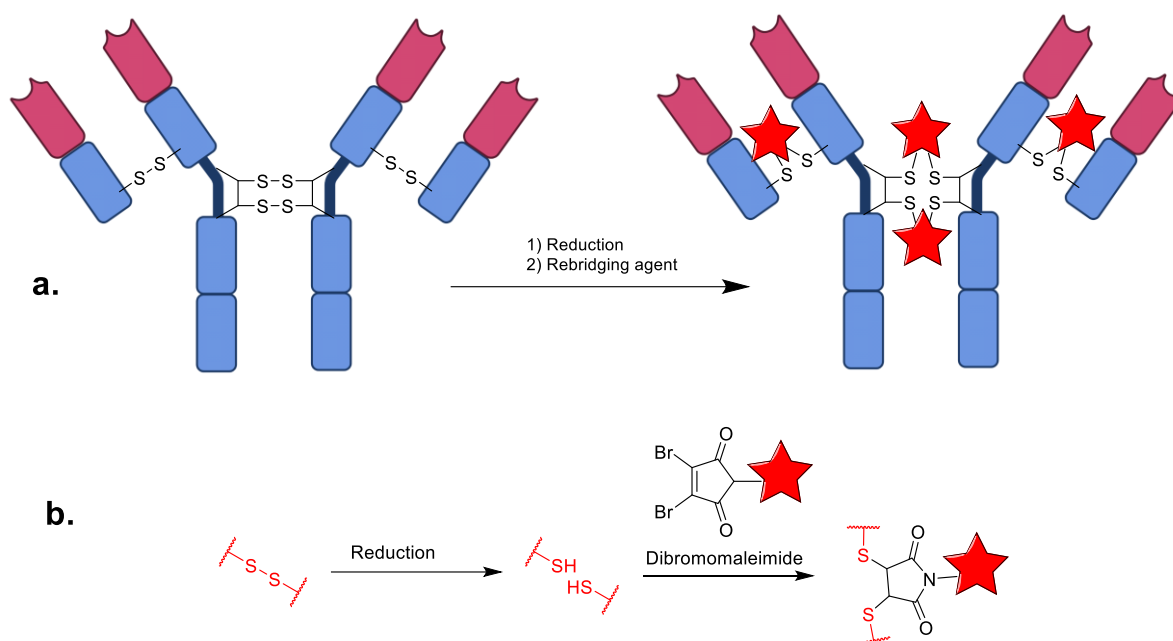


**Figure 17.** Use of disulfide rebridging using bis-reactive rebridging reagents. **a.** Illustration of disulfide rebridging. **b.** Use of dis-reactive dibromomaleimide rebridging agent. The reduction of disulfide bonds is followed by reaction with dibromomaleimide re-joining the strands via a maleimide linker.

### 1.5.2.2 Engineered antibodies

Rather than rely on naturally occurring amino acids, reactive residues can be engineered into the primary structure of the antibody, thereby providing specific functionalities for conjugation. This strategy improves versatility and selectivity over natural antibodies; however, it is more expensive and potentially immunogenic (86). The most prevalent method used in producing engineered antibodies is THIOMAB<sup>TM</sup>, in which cysteine residues are installed at desired points by site-directed mutagenesis (87). These engineered cysteines can be selectively cleaved to allow conjugation while leaving interchain disulfide bonds intact. Maleimide retro-Michael reaction instability is largely governed by solvent accessibility and may be limited by conjugation at sterically hindered sites (79,88). ADCs with >90% homogeneity have been produced with this method, retaining efficacy with decreased toxicity compared to ADCs produced with natural antibodies. Almost all THIOMAB<sup>TM</sup> ADCs are produced with a moderate DAR of 2, however, a DAR of 4 has been achieved (89). Non-canonical amino acids with bioorthogonal reactive handles can also be engineered into proteins (75,86). For example, azide containing amino acids have been introduced, allowing site-selective payload attachment



via azide-alkyne click reactions. Although these approaches offer unrivalled selectivity and versatility, the expression yields tend to be lower than natural proteins and bear an increased immunogenic risk.

### 1.5.3 Drug-linker attachment

Drug-linker attachment is a crucial component of ADCs. The properties of the drug-linker define the nature of the active species and the timing of its release (30). Consequently, significant effort has been placed into developing a variety of linkers aiming for the “Goldilocks zone” of plasma stability and selective release at the target. Three major classes of linkers exist, non-cleavable, chemically cleavable, and enzyme-cleavable linkers.

#### 1.5.3.1 Non-cleavable linkers

Non-cleavable linkers, as their name implies, contain no trigger to release the payload. Instead, following antibody degradation in the lysosome, the payload is released with the linker and a charged amino acid still bound (90). This strategy benefits from potentially improved plasma stability over cleavable linkers and reduced efflux through multidrug-resistance transporters due to the hydrophilic charged appendage, however, it is dependent on payload efficacy not being hindered by the residual linker. Furthermore, these payloads can typically only affect antigen-positive cells as the charged species prevent passive diffusion (bystander effect).

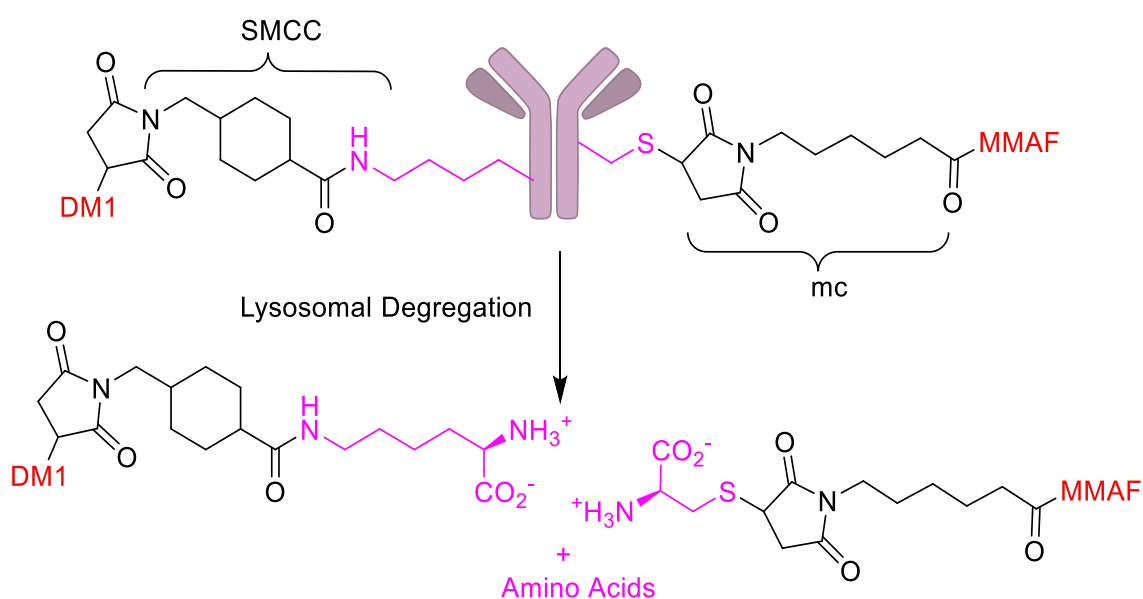


**Figure 18.** Noncleavable SMCC and mc linkers are released with an additional charged Lys or Cys appendage respectively following enzymatic degradation of the mAb within lysosomes.

There are two commonly used non-cleavable linkers, succinimidyl-4-(*N*-maleimidomethyl)cyclohexane-1-carboxylate (SMCC) and maleimidocaproyl (mc), used with DM1 and MMAF payloads, respectively. Degradation of the ADC releases these drug-linkers with either charged cysteine (mc) or lysine (SMCC) appendages (**Figure 18**). Ado-trastuzumab emtansine is comprised of a SMCC-DM1 drug-linker that, despite the additional attachment, retains excellent intracellular cytotoxicity comparable to free DM1 (91). However, the drug-linker payload cannot elicit a bystander effect by diffusing into neighbouring cells (92). The sulfo-SMCC-MMAF drug-linker, employing an additional sulfate monoester to reduce hydrophobicity has achieved approval with belantamab mafodotin, however, this ADC was recently removed from the market due to a lack of efficacy (17,21,22).

### 1.5.3.2 Cleavable linkers

Cleavable linkers exploit specific conditions to trigger payload release at the target cell. Typically these conditions are met in lysosomes following endocytosis due to the uniquely low pH or high concentration of hydrolytic enzymes (30). Alternatively, cleavable linkers may be susceptible to extracellular conditions in the tumour-microenvironment or exogenous stimuli, thereby avoiding antibody internalisation requirements. Importantly, cleavage from these linkers does not leave residual charged moieties, instead yielding the unmodified payload. Being released unmodified allows suitable payloads to elicit a bystander effect, potentially benefiting activity against heterogeneous tumours. The effectiveness of these strategies is reflected in their predominance among approved ADCs and those in clinical development (30).

### 1.5.3.3 Acid cleavable linkers

Acid cleavable linkers aim to exploit the acidity of lysosomes (pH 4.5-5) to trigger payload release while remaining stable in circulation at pH 7.4. Gemtuzumab ozogamicin and inotuzumab ozogamicin contain the same acid cleavable “ozogamicin” drug-linker. This drug-linker contains an acid sensitive *N*-acyl hydrazone linkage, which undergoes hydrolysis to release a hydrazide-payload and a ketone (**Figure 19.b**) (93). Analysis of Inotuzumab ozogamicin stability *in vivo* revealed hydrolysis in circulation occurs at a rate of only 1.5-2% a day (94), whereas other hydrazone containing linkers have demonstrated significant discrepancies between buffer and plasma stability (95). The tumour microenvironment is also slightly acidic (pH 6), providing an opportunity for extracellular drug release at the target site (96). Indeed, an ADC comprised of non-internalising mAb rituximab and an ozogamicin drug-

## Introduction

linker was more efficacious than unconjugated mAb, yet ineffective when replaced with a non-cleavable linker (97).

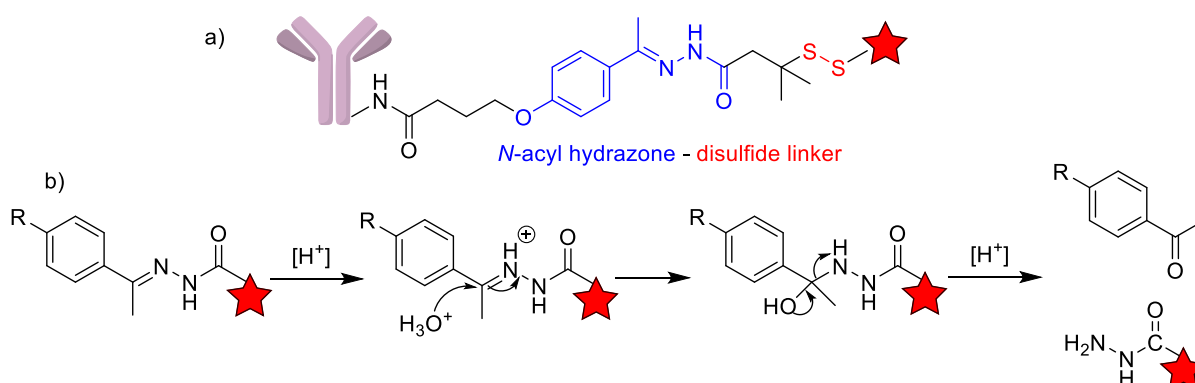


**Figure 19.** a. Hydrazone containing “ozogamicin” drug-linker delivers a *N*-acyl calicheamicin payload. b. Hydrolysis of the *N*-acyl hydrazone occurs at acidic pH.

Alternatively, acid-sensitive carbonates have been explored as cleavable motifs. Simple alkyl-carbonates are too unstable for use, however, introducing a *para*-amino benzyl (PAB)-spacer (**Figure 20**) improves ADC serum stability (98). The recently approved ADC sacituzumab govitecan employs this more stable carbonate linker (36).

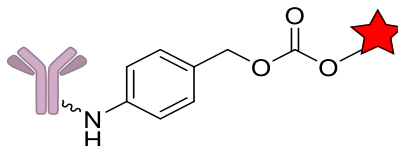


**Figure 20.** Acid-cleavable *para*-aminobenzyl carbonate employed in sacituzumab govitecan.

Despite their clinical success, acid cleavable linkers have fallen out of favour in ADC development. The requirement for selectivity between pH 5 and 7.4 is inherently difficult, and development now focuses on other approaches with superior tumour selectivity (30).

### 1.5.3.4 Reducible disulfides

Disulfides are the most prominent class of chemically cleavable ADC linkers. Disulfide bonds are stable to hydrolysis at pH 7.4 but are susceptible to nucleophilic attack by thiols (**Figure 21**) (30,99). Disulfide-containing linkers exploit the high intracellular glutathione (GSH) concentrations (1-10 mM) compared to the limited availability of GSH or other thiols in plasma (<1% of whole blood GSH found in plasma) to achieve selective release following internalisation (100). Furthermore, cancer cells often express elevated GSH levels to cope with increased oxidative stress, potentially offering additional tumour selectivity (101).

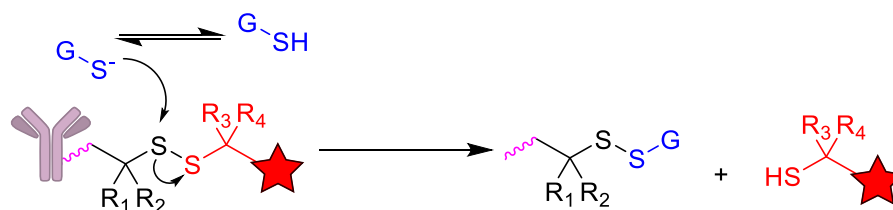


**Figure 21.** Reduction of disulfide linkers by glutathione (represented as GSH). Increasing the steric bulk around the disulfide (R1-4) increases circulatory stability but decreases release efficiency. The optimal composition of R1-4 varies for specific ADCs *in vivo*.

### 1.5.3.5 Extracellular disulfide reduction

Reducible disulfide linkers have been applied to non-internalising ADCs combining tumour vascular targeting mAbs with "linker-less" disulfide technology (102,103). Payload release is triggered by high concentrations of reductants released by dying cells into the extracellular space and the often-hypoxic microenvironment associated with tumours. This way, initial cell death causes a chain reaction, increasing the concentration of reductants in the extracellular tumour microenvironment, triggering further payload release. Non-internalising ADCs of this type have not yet attained clinical approval.

### 1.5.3.6 Cleavage by exogenous stimuli

Rather than rely on an innate physical or biological liability of the linker, cleavage can be triggered by exogenous stimuli administered after the ADC. As this strategy is not dependent on factors intrinsic to individual patients, it has the potential to decrease interpatient variations in payload release. However, this strategy requires co-administration of an additional component to act as a trigger, complicating therapy. An example of this approach is an alkynyl thioether-containing ADC linker which releases an amine-linked payload upon exposure to Pd<sup>0</sup>. While effective and selective *in vitro*, appropriate Pd complexes are not yet available for systemic therapy (104). Photocleavable linkers do not require an additional reagent. Instead, light is applied to the target site to trigger payload release. Photosensitive protecting groups such as *o*-nitrobenzyl groups and their derivatives are commonly used in chemical and biological research and have been investigated as potential ADC linkers (105,106). An example of this is a 4,5-dimethoxy-2-nitrobenzyl (DMNB) linker that following irradiation by light at 360 nm forms a highly active diradical species triggering payload release (**Figure 22**) (106).

## Introduction

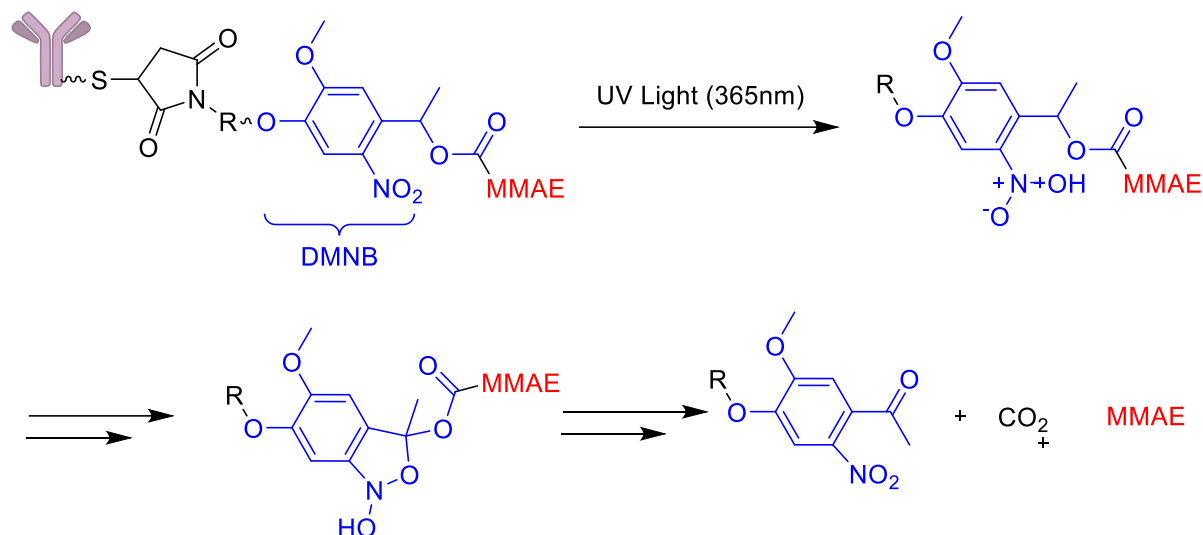


**Figure 22.** UV-cleavable DMNB linker. Following irradiation by light at 365 nm, the linker undergoes a self-immolation to release an MMAE payload, a ketone and CO<sub>2</sub>.

These linkers have been applied to ADCs, affording promising stability, binding capacity, and selectivity *in vitro* (106). Payload release was effectively triggered by irradiation with light at 365 nm, while the unirradiated drug-linker was 7-fold less cytotoxic and poorly cell permeable, providing an added benefit by limiting off-target toxicity due to non-specific uptake. In cell growth assays these ADCs were 100-fold more cytotoxic against antigen positive than antigen negative cells. However, the use of UVA irradiation ( $\lambda=315\text{-}400\text{ nm}$ ) at high dosage does cause toxicity, while lower wavelength UV blue light poorly penetrates through skin/tissue preventing exposure deep within the tumour area. Further *in vivo* development is required to progress these treatments (106). As an alternative for photoactivation, infrared (IR) light is less toxic and penetrates deeper into tissues. Linkers based on heptamethine cyanine dyes (HMCDs) have been applied to ADCs carrying duocarmycin payloads (107). Cyanine-based linkers undergo a two-step cleavage following exposure to IR light (**Figure 23**). The use of HMCDs has two additional advantages: HMCDs accumulate in tumours, a property that has been investigated as a standalone delivery vehicle for cancer drugs (108), and HMCDs fluoresce at a near IR wavelength (690 nm), which could allow ADCs with these linkers to be monitored *in vivo*. A key downside of HMCD linkers is a significantly more complex synthesis versus their *o*-nitrobenzyl counterparts. Development of photocleavable linkers for ADCs is ongoing.

## Introduction

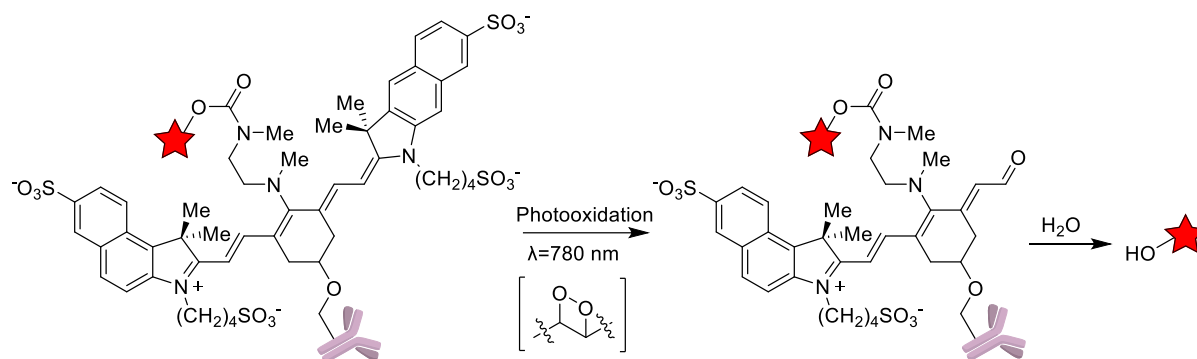


**Figure 23.** IR-cleavable HMCD linker. Exposure to light at 780 nm causes photooxidation cleaving the cyanine via dioxetane intermediates, and a following cyclisation hydrolyses the linker carbamate to release an alcohol payload.

### 1.5.3.7 Enzyme cleavable linkers

Enzyme-cleavable linkers comprise the most widely used group of ADC linkers (30). This linker class aims to exploit the high concentrations of unique hydrolysing enzymes found within lysosomes or hydrolases in the extracellular tumour microenvironment to trigger selective payload release. The general lack of metabolising enzymes in circulation and the diverse range of potential functional groups available to enzyme cleavable linkers make them attractive options in ADC development. Unlike established non-cleavable and chemically cleavable linkers, enzyme cleavable linkers have achieved “traceless release”, in which payloads are released without residual chemical matter from the linker.

### 1.5.4 Enzyme cleavable linkers

#### 1.5.4.1 Cathepsin-cleavable

Cathepsin-cleavable linkers are the most prevalent linkers in ADCs reaching clinical development, including the approved ADCs brentuximab vedotin, polatuzumab vedotin-piiq, enfortumab-vedotin-ejfv and trastuzumab deruxtecan. There are eleven members in the cysteine-cathepsin family of proteolytic lysosomal enzymes, with cathepsin B (CatB) being the most highly expressed, presenting a particularly attractive target for enzyme cleavable linkers (109,110). Proteolysis is an important process in cell signalling pathways, such as activation of growth factors and is required for both angiogenesis and tumour invasion into surrounding tissues. Unsurprisingly cathepsins are implicated in cancer progression and metastasis, and CatB is often found overexpressed in tumours, particularly in advanced or metastatic solid tumours (111,112). The increased expression among advanced tumours potentially provides

## Introduction

additional tumour selectivity to these ADC therapies (110,111). Although CatB is the primary target, evidence suggests the linkers are substrates across various cathepsin family members (113–115). Indeed gene suppression of CatB-expression does not affect payload release *in vitro* (114). Therefore, these linkers are not CatB specific and are more accurately labelled "cathepsin cleavable".

The first cathepsin cleavable linkers developed were valine-citrulline (Val-Cit) and phenylalanine-lysine (Phe-Lys) dipeptides separated from the payload by a self immolative *para*-aminobenzyl carbamate (PABC) spacer (**Figure 24**) (116–118). Following enzymolysis, a 1,6-elimination releases CO<sub>2</sub>, aza-quinone methide and the free unmodified payload (**Figure 25**). Development of these linkers is complicated by long term instability in mouse plasma ( $t_{1/2}$  = 12.5 h) due to a susceptibility to cleavage by rodent carboxylesterase 1C (Ces1C). The instability of Val-Cit-PABC linkers in rodent plasma presents a major problem in drug development by complicating accurate modelling of the safety and efficacy of Val-Cit-containing ADCs *in vivo*. Regardless, high *in vivo* activity, therapeutic index and impressive human plasma stability have led to the Val-Cit-PABC linker being employed across a broad range of payloads and antibodies. Seattle Genetics' Val-Cit-PABC-MMAE drug-linker, under the name "vedotin", is present in four approved ADCs: Brentuxumab vedotin, Polatuzumab vedotin-piiq, Enfortumab-vedotin-ejfv and tisotumab vedotin-tftv (14,19,30,119,120). Val-Cit dipeptide linkers are highly hydrophobic, resulting in ADCs employing the hydrophobic vedotin drug-linkers being limited to DAR of around 4.

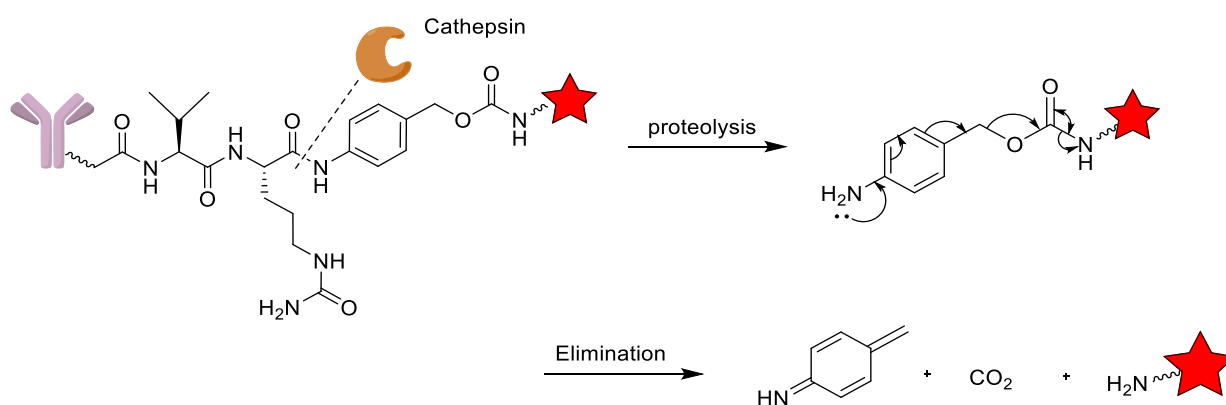


**Figure 24.** Structure and mechanism of cleavage of dipeptide (Val-Cit) cleavable linkers. Proteolysis releases a self-immolative *para*-aminobenzyl carbamate which undergoes a 1,6-elimination to release the payload.

The clinically approved ADC trastuzumab deruxtecan utilises a glycine (Gly), Gly-Gly-Phe-Gly linker cleaved by most cathepsin family members (121). Importantly, trastuzumab deruxtecan is able to achieve a maximal DAR of 8 without significant aggregation due to the reduced hydrophobic nature of the drug-linker (122). However, CatB and cathepsin H (CatH) primarily cleave the sequence incorrectly, leaving a Gly appendage on the payload the resulting modified payload is 20-190 times less potent than the free payload.

### **1.5.4.1.1 Other Cathepsin cleavable linkers**

Val-Alanine(Ala)-PABC dipeptide linkers have emerged as an effective, less hydrophobic alternative to their Val-Cit counterparts (123–125). For this reason, Val-Ala-PABC linkers are often employed alongside PBD-dimer payloads due to the exceptionally high hydrophobicity of these payloads. Val-Ala linkers have substantially slower CatB cleavage rates compared to their Val-Cit analogues. The Val-Ala motif also has a Ces1C liability in mouse plasma (126). More recently, CatB selective linkers have been reported (127). Given CatB's implications in cancer metastasis, an ADC whose release mechanism depends entirely on CatB may have enhanced selectivity against cancers with increased CatB expression.

Non-internalising Val-Cit ADCs have also been explored as cathepsins have been found in the secretomes of a range of cancers (128). Impressively, non-internalising ADCs with Val-Cit-PABC linkers were efficacious *in vivo* against two xenograft models. Later reports found Val-Ala-PABC linkers imparted the best antitumour efficacy of all the linkers considered (129). While evidence suggests that payloads are being released selectively in the tumour microenvironment, no evidence has yet been provided as to which enzymes are responsible. Without this knowledge, it is difficult to predict efficacy in primates (130). Given the pharmacogenetic complications of selectively targeting enzymes and the success of general cathepsin cleavable linkers, further development of CatB selective and other cathepsin-cleavable strategies is unclear. Instead, the development of new strategies is focused on novel mechanisms of payload release.

### **1.5.4.2 Glycosidase cleavable linkers**

#### **1.5.4.2.1 $\beta$ -glucuronidase-cleavable linkers**

$\beta$ -glucuronidases are lysosomal enzymes that catalyse the hydrolysis of  $\beta$ -glucuronic acid residues in polysaccharides. As with cathepsins,  $\beta$ -glucuronidases are overexpressed and secreted in some tumours and have been the target of drug delivery therapies as early as 1998



(128,131). The use of  $\beta$ -glucuronidase as a release trigger for ADCs was first reported in 2006, with a benzyl spacer bearing an additional carboxamide substituent for bioconjugation (132). Following metabolism by  $\beta$ -glucuronidase, the benzyl spacer undergoes a self-immolative 1,6-elimination to release an amine payload (**Figure 25.a**). Benefiting from improved hydrophilicity over other linkers, this motif has been employed with a wide range of hydrophobic payloads to achieve high DARs without significant antibody aggregation (30). Furthermore, this linker has illustrated outstanding stability in rodent and primate blood, with an extrapolated half-life of 81 days in rat plasma (132). ADCs employing these linkers have typically been as efficacious as Val-Cit-PABC analogues and have been shown to be equally capable of eradicating heterogeneous tumours (31,133).

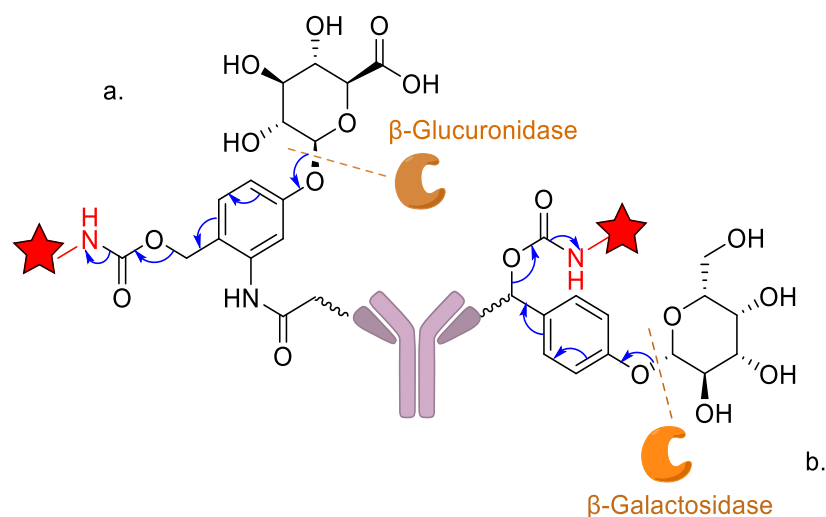


**Figure 25.** Structure and mechanism of release of examples of a.  $\beta$ -glucuronidase and b.  $\beta$ -galactosidase cleavable linkers.

#### 1.5.4.2.2 $\beta$ -galactosidase-cleavable linkers

$\beta$ -galactosidase ( $\beta$ -gal) prodrugs have been described in other targeted cancer therapies including as linkers in ligand directed prodrug monotherapy. More recently, this  $\beta$ -galactosidase prodrug strategy has been applied to linkers for ADCs (**Figure 25.b**) (134,135). These linkers achieved higher efficacy in linking trastuzumab and MMAE than a Val-Cit-PABC analogue. Further, this drug-linker combination illustrated superior efficacy against HER2+ mammary tumours in mice than the clinically approved trastuzumab emtansine.

### 1.5.4.3 Phosphatase-cleavable linkers

Pyrophosphatase and acid phosphatase are lysosomal enzymes capable of hydrolysing pyrophosphates and terminal monophosphates respectively. Targeting these enzymes for drug release offers two advantages over cathepsins: the substrates are naturally hydrophilic, and the payloads are able to be released as either alcohols or amines, broadening the scope of potential payloads (30). The initial use of phosphatases employed terminal phosphates as leaving groups for known Val-Cit-PAB linkers (136). The improved hydrophilicity allowed for conjugation to lipophilic glucocorticoids to produce potent and selective ADCs. The proteolysis of the Val-Cit group and immolation of the PAB spacer release the payload monophosphate, which is rapidly hydrolysed by acid phosphatases to reveal the glucocorticoid drug (**Figure 26.a**). Although potent and selective, the plasma stability of the linker is modest (half-life = ~6 h), and *in vivo* data has yet to be reported.

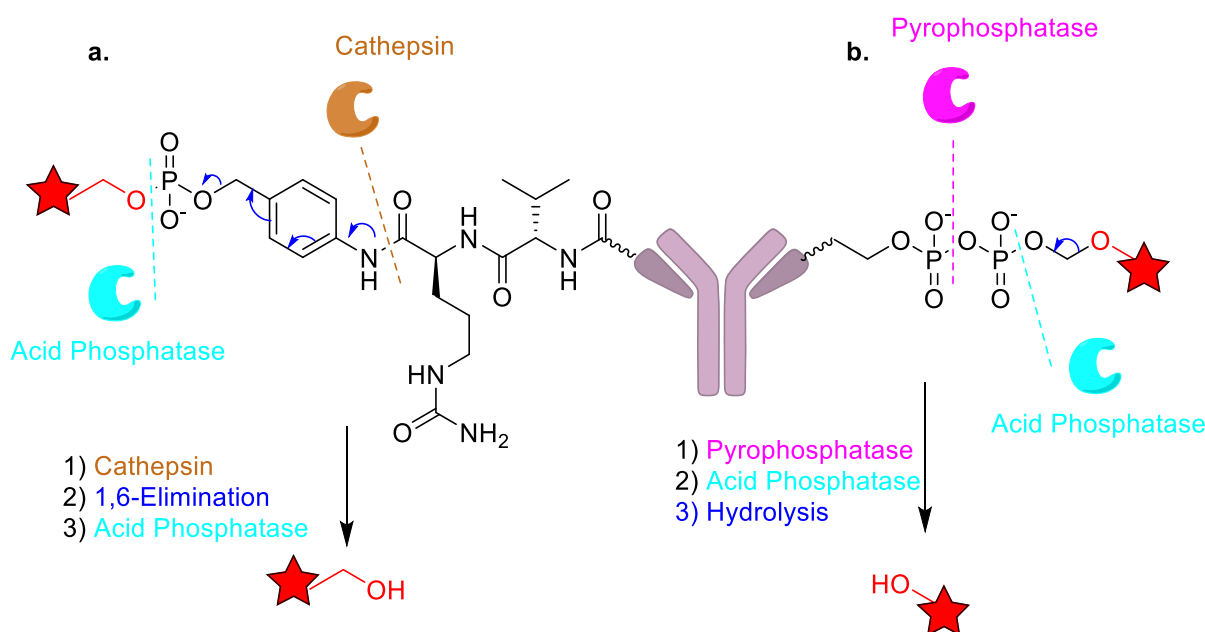


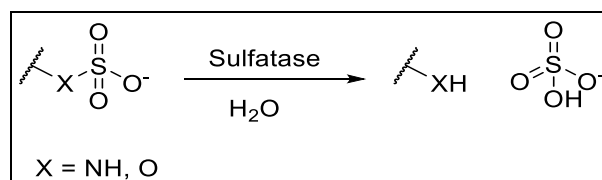
**Figure 26.** Structure and mechanism of release of dual enzyme Cathepsin/phosphatase and Pyrophosphatase/phosphatase cleavable linkers.

More recently, simple pyrophosphate containing linkers have been reported that release alcohol payloads (137). Here lysosomal pyrophosphatase first cleaves the phosphate-diester revealing the payload monophosphate. The phosphate is then cleaved by acid-phosphatase followed by hydrolysis of the resulting acetal to release formaldehyde and the free payload (**Figure 26.b**). Crucially these drug-linkers were soluble in water above 5 mg/mL, facilitating conjugation to lipophilic glucocorticoids in aqueous media, where other linker technologies have failed.

## 1.6 Sulfatase-cleavable linkers

Recently Bargh *et al.* reported the development of novel sulfatase-cleavable linkers (138). These linkers illustrate several attractive properties for application to ADCs.

Sulfatases are hydrolytic enzymes responsible for the hydrolysis of sulfate monoesters and sulfamates to alcohols and amines respectfully (see **Section 1.7**) (**Scheme 1**) (139).



**Scheme 1.** Sulfatase hydrolysis of sulfate monoesters (X= O) and sulfamates (X = NH).

Sulfatases are attractive targets for enzyme-cleavable linkers as their activity is almost absent in circulation and highest within lysosomes. Further, sulfatases are reportedly over expressed in several cancer cell lines (140), potentially improving the tumour selectivity of sulfatase-dependent ADCs. Sulfate monoesters are a highly polar functional group which exist as anions at physiological pH. The inclusion of this charged group improves the aqueous solubility of drug-linkers aiding conjugation and minimising antibody aggregation (138,141).

Simple *para*-sulfoxy benzyl carbamate “arylsulfatase-cleavable” linkers release amine payloads following sulfate-hydrolysis and subsequent 1,6-elimination (**Figure 27.a**). These linkers take advantage of sulfatases substrate tolerance for small synthetic aryl sulfate esters. Indeed, all eight lysosomal sulfatases illustrate some degree of activity against arylsulfates, four of which are described by the generic name “arylsulfatase”, reflecting their high activity against small arylsulfates monoesters (139,142). Arylsulfatase activity is highest within lysosomes. Ultimately this provides significant enzymatic redundancy for these “arylsulfates-cleavable” linkers. An initial report indicates these linkers are stable in both human and rodent plasma and efficiently released their payload in the presence of snail and human arylsulfatases. When the arylsulfatase-cleavable linkers were incorporated into ADCs, they produced effective conjugates which killed antigen positive cancer cells with similar efficacy to Val-Cit-PABC analogues and were inactive against antigen-negative cell lines (138). In this report by Bargh *et al.*, (138) only three linker analogues were prepared, two with differing sites of antibody conjugation (**Figure 27.b-c**) and a third with an additional electron-withdrawing nitro group that produced the most efficacious ADC in cell assays (**Figure 27.d**). The improved

## Introduction

efficacy observed with the third linker analogue could be due to an increased rate of sulfate hydrolysis and payload release caused by the electron withdrawing effect of the nitro group; however, this nitro analogue was not investigated in enzyme assays. Therefore, what factors make the inclusion of the nitro substituent favourable remains unclear and could be linked to other aspects of ADC pharmacology. Interestingly sulfatases are found across all domains of life with a remarkably conserved active site and common arylsulfatase activity (**Section 1.7**) (139,143). Therefore, arylsulfatase-cleavable linkers have the potential to be applied to ADCs across indications outside of cancer such as against infectious bacteria.

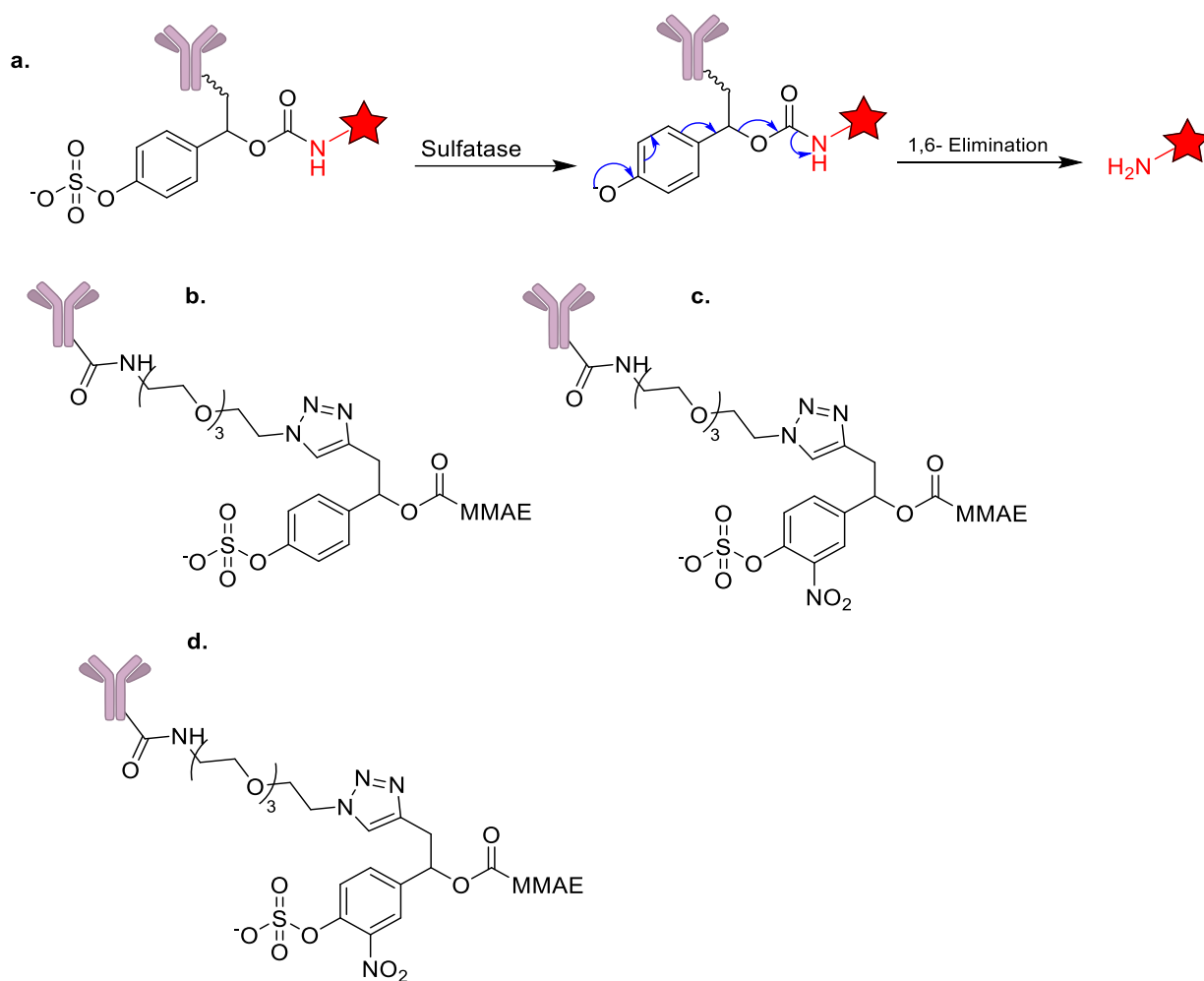


**Figure 27.** a. Structure and mechanism of release of *para*-sulfoxy-benzyl carbamate sulfatase cleavable linkers. b-d. Arylsulfatase-cleavable linker structures investigated by Bargh *et al.*, (138).

A follow-up publication from this same group reported the development of sulfatase  $\beta$ -galactosidase dual enzyme cleavable linkers (141). These linkers mimic the natural metabolic pathway of sulfatide, the natural substrate of human arylsulfatase A (ARSA). First, the sulfate ester is hydrolysed by ARSA followed by cleavage by  $\beta$ -gal and subsequent 1,6-elimination mediated release of the payload (**Figure 28**). These linkers were stable in plasma and readily

## Introduction

cleaved in the presence of both enzymes *in vitro*. The addition of the anionic sulfate monoester improved aqueous solubility over analogous  $\beta$ -gal cleavable linkers lacking this functionality. When these linkers were applied to ADCs, the resulting conjugates were found to be as cytotoxic as arylsulfatase cleavable- and dipeptide-linked analogues at equal DAR implying similar efficiency of payload release between strategies, although no rate of release experiments to compare the linkers and other factors may be influencing efficacy.

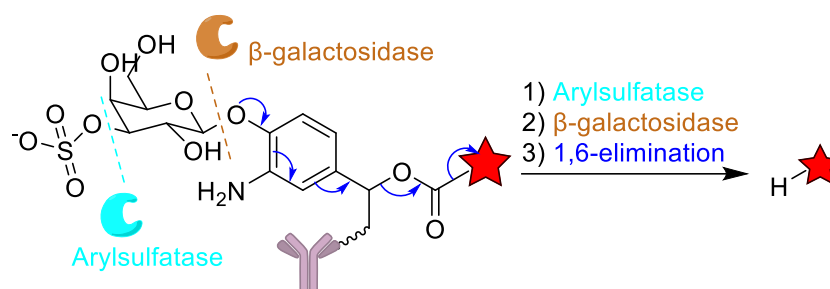


**Figure 28.** Structure and mechanism of release of dual enzyme cleavable sulfatase/ $\beta$ -galactosidase cleavable linkers.

The ARSA/ $\beta$ -gal ADCs benefit from the hydrophilic character provided by both the anionic sulfate monoester and pyranose functionalities and additional lysosomal targeting by relying on two lysosomal enzymes. However, this approach comes at the expense of the enzymatic redundancy of its arylsulfatase-cleavable counterpart. Further development of these strategies, including higher DAR ADCs and *in vivo* data, is required before conclusions can be drawn on either strategy. The use of prodrug strategies to improve hydrophilicity is well established in drug development, however, prior attempts to develop small molecule sulfatase prodrugs were unsuccessful (144,145). Sulfate prodrugs of phenytoin were stable in plasma and readily converted to the active species in the presence of sulfatases, although, no activity was achieved *in vivo*. Blood samples from rats found no conversion to the active species. Instead, the sulfate prodrug was rapidly cleared from circulation achieving a half-life of only 34 minutes, leading to the strategy being abandoned. Alternatively, sulfatases have been explored for antibody directed enzyme prodrug (ADEPT) strategies (146). Here antibody bound sulfatases were used to selectively activate circulating sulfate prodrugs in the extracellular tumour environment. Although preliminary studies reported that the sulfate prodrugs were activated in the target environment the strategy was not pursued further, likely due to rapid clearance of the sulfate prodrug. Charged species like anionic sulfates have poor cell permeability stranding the prodrugs in circulation away from sulfatase activity and tagging them for renal elimination. Indeed, sulfation is a physiological mechanism for clearing exogenous compounds such as

xenobiotics (147). However, these traits provide an excellent opportunity for application to ADCs. ADCs are not cleared renally due to the size of the mAb limiting this liability while intact, therefore, any sulfate-drug-linker released in circulation would be rapidly cleared limiting the risk of instability related toxicity.

### 1.7 Sulfatases

Sulfatases are a family of hydrolytic housekeeping enzymes found across all domains of life that hydrolyse sulfate monoesters and sulfamates to alcohols and amines respectively (139). In humans, sulfatases play key roles in glycolipid metabolism, hormone regulation, and cell signalling. There are 17 known human sulfatases, eight of which are lysosomal (142). These enzymes are highly selective for their physiological substrates and have little functional redundancy; indeed, eight distinct disorders are caused by deficiencies in single sulfatases (148). The known human sulfatases all have alkyl sulfate and sulfamate substrates except arylsulfatase C (ARSC) which hydrolyses an aryl substrate (**Figure 29**) (139,149). Despite this, all sulfatases are active against small xenobiotic arylsulfates such as *para*-nitrocatechol sulfate (*p*NCS) and 4-methylumbelliferyl sulfate (MUFS) (139). In some cases, this activity was discovered *in vitro* prior to the identification of the enzyme's physiological substrates, and as a consequence, many sulfatases carry the generic name “arylsulfatase” (ARS). The degree of arylsulfatase-activity across the family is quite varied, and some sulfatases such as idurinate-2 sulfatase (IdoA2S) and glucosamine-6-sulfatase (GalN6S) have only negligible activity towards aryl substrates earning the moniker non-arylsulfatases. Indeed, ARSA and arylsulfatases (ARSB) mediate a 4000-fold and 3000-fold higher turnover of MUFS than the non-arylsulfatase GalN6S (150). To date interest in sulfatases has been primarily driven by their roles in various physiological conditions, including lysosomal storage diseases and hormone dependent cancers (148).

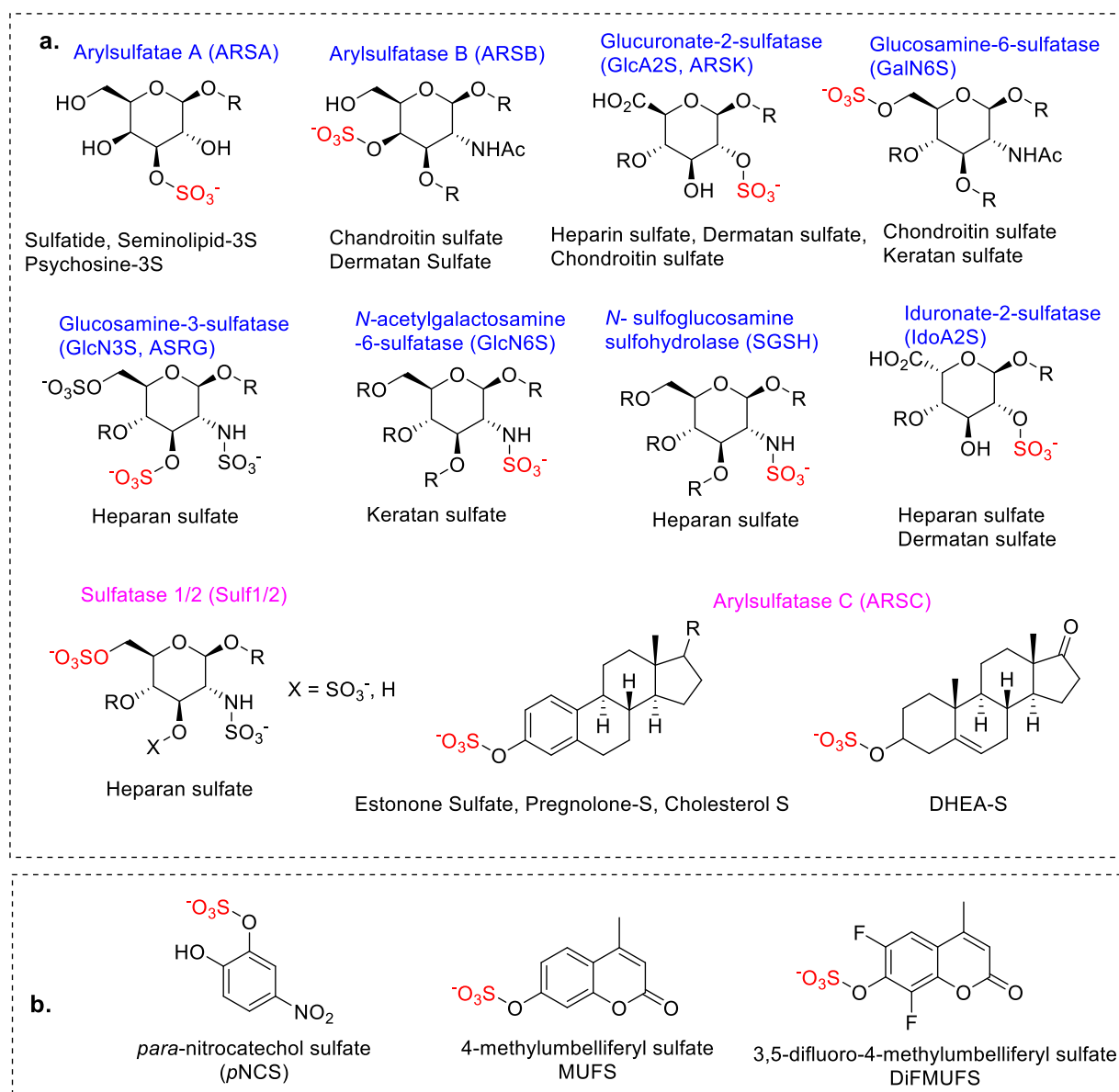


**Figure 29.** Known human sulfatase substrates. The substrates target sulfate are highlighted in red, lysosomal sulfatases are listed in blue; non-lysosomal sulfatases are listed in purple. **a.** physiological substrates. **b.** Synthetic arylsulfate monoester probes. R is varied between substrates.

### 1.7.1 Structure

To date, the structures of six human sulfatases have been solved by X-ray crystallography ARSA (151), ARSB (152), ARSC (149), IdoA2S (153), GalN6S (154), and SGSH (155) (**Figure 31**). All share significant sequence and three-dimensional structural similarities. Each sulfatase is a globular enzyme of mixed  $\alpha\beta$  topology comprised of a conserved *N*-terminal domain and a more varied *C*-terminal “substrate specific” domain. The *N*-terminal domain comprises several  $\alpha$ -helices surrounding a larger mixed  $\beta$ -sheet (**Figure 30**). The active site cavity is found at the *C*-terminal end of the large  $\beta$ -sheet. The  $\beta$ -sheet comprises ten strands for

## Introduction

most family members yet is shortened to seven and eight strands in IdoA6S and SGSH respectively. The C-terminal is comprised of a four stranded antiparallel  $\beta$ -sheet packed against a long  $\alpha$ -helix. Some sulfatases also present a “meander” motif that helps define the active sites of ARSA, B, and GlcN6S but is absent in other family members. The C-terminal domain has higher structural diversity between sulfatases and presumably plays the most significant role in substrate discrimination between these selective enzymes. A stretch of high sequence similarity between the C-terminal domain of human GlcN6S and GlcNAc transferase from *Arabidopsis thaliana* supports this, suggesting this homologous region is responsible for substrate recognition of their shared substrate GlcNAc (156).

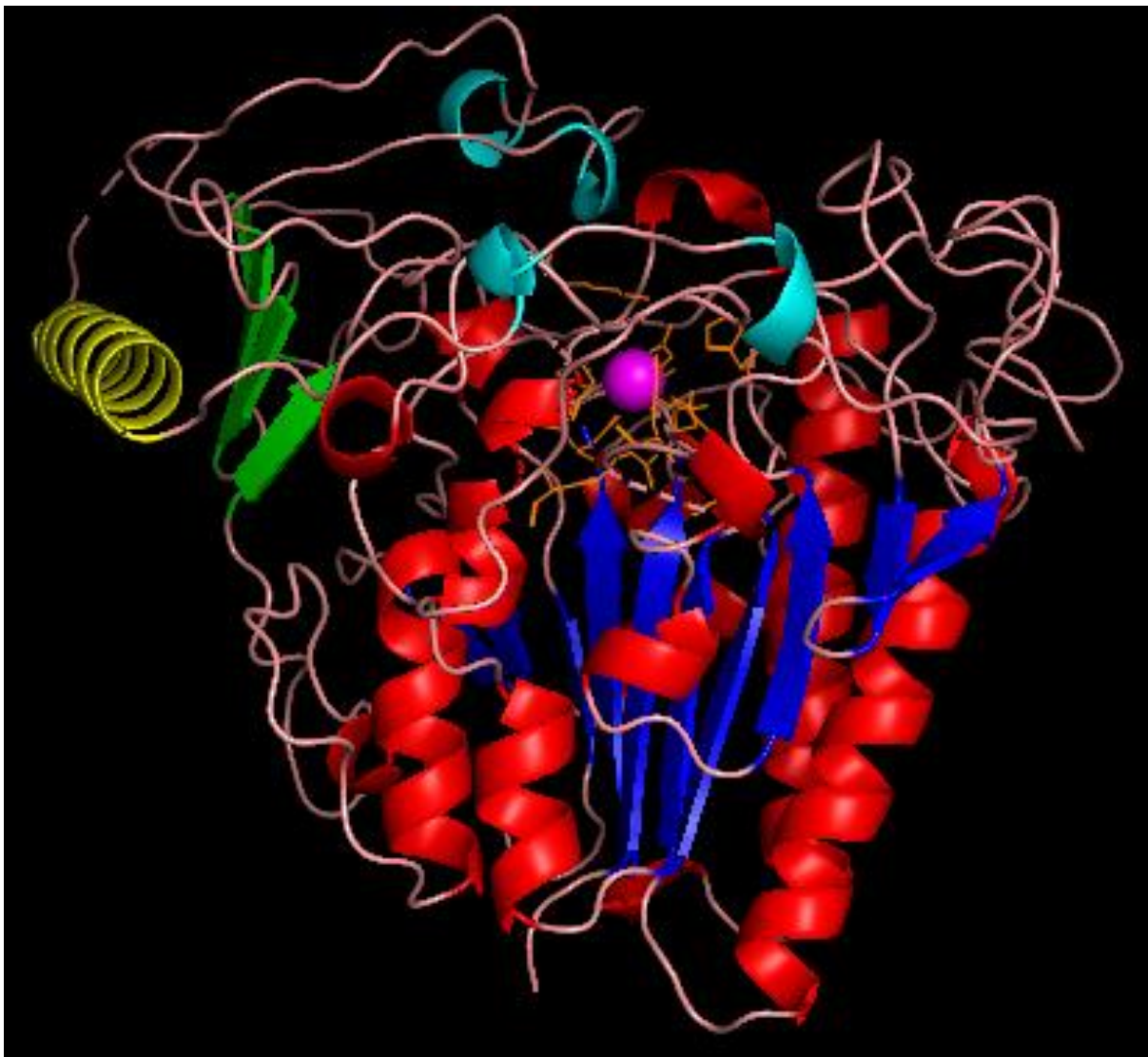


**Figure 30.** Cartoon representation of human arylsulfatase A (PDB: 1AUK). The C-terminal domain is comprised of a long  $\alpha$ -helix (yellow), an antiparallel  $\beta$ -sheet (green) and meander motif (cyan). The N-terminal domain is comprised of  $\alpha$ -helices (red) and a large  $\beta$ -sheet (blue). The conserved active site residues are represented in orange; the metal cation is illustrated in purple.



### 1.7.2 Sulfatase active site

The active site is highly conserved across the enzyme family and is found at the bottom of a narrow cleft lined with charged residues leading to a unique formylglycine (FGly) residue (139,151,157). All sulfatases contain a 5'-C/S-X-P-S/X-R-X-X-X-L/X-T/X-G/X-R/X-3' (Single letter amino acid codes where X is any amino acid) sequence motif. This motif is believed to direct the formation of this unique residue through post translational modification of the active site cystine by formylglycine generating enzyme (FGE) (139,158). This modification is essential to sulfatase activity; inactivation of FGE results in the fatal global inactivation of all sulfatases found in multiple sulfatase deficiency (MSD) (159). Further, the core motif C/S-X-P-X-R is conserved across nature from eukaryotic to prokaryotic organisms suggesting a common mechanism of sulfate hydrolysis is conserved. A crystal structure of ARSA at resting state solved the FGly in a two-fold electron density pattern suggesting the FGly naturally exists as a formyl glycine hydrate (FGH) at resting state (discussed in **Section 1.7.3**) (151). As well as the unique FGly several other key residues contribute towards substrate binding and hydrolysis (139). Ten interconnected polar residues and a divalent metal cation are conserved in the active site. In the case of ARSA, the importance of these residues was further established in a mutational scanning experiment (157). Their identity and proposed function are outlined in **Table 1**.

**Table 1.** Identity and proposed function of conserved active site residues.

<b>Residue</b>	<b>Function</b>
FGly	Catalytic nucleophile (as FGH)
Metal cation (Ca <sup>2+</sup> )	Substrate binding/activation Stabilisation of FGH
AsnA (Gln in ARSC)	Metal co-ordination Activation of FGH
AspA	Metal co-ordination
AspB	Metal co-ordination
AspC	Metal co-ordination
ArgA	Metal co-ordination
HisA	Stabilization of FGH Elimination of enzyme-sulfate intermediate
HisB	Substrate binding/activation Alcohol protonation
LysA	Substrate binding/activation Stabilization of FGH
LysB	Substrate binding/activation Alcohol protonation

## Introduction

The residues AspA, AspB, AspC, and AsnA (Gln in ARSC) form the metal binding region. This region, alongside an oxygen from the FGH and an oxygen from the sulfate ester substrate coordinate to form a divalent metal cation. Initially, a study of ARSA's crystal structure found the cation to be an octahedrally coordinated  $Mg^{2+}$ , however, subsequent studies have instead found a hepta-coordinated  $Ca^{2+}$  (151,157,160). It is likely the initially observed  $Mg^{2+}$  cation was an artifact caused by the high concentration of  $Mg^{2+}$  used in the enzyme purification process displacing the native  $Ca^{2+}$  cation. Mutation of any residues in the metal binding region severely decreased substrate binding and activity (157). This underscores the importance of this region to catalysis, presumably by binding the substrate in the active site and priming it for nucleophilic attack. The charged LysA, LysB, HisB, and metal cation act to neutralise the anionic sulfate, withdraw electron density to create an electrophilic sulfur centre, and position the tetrahedral sulfate for nucleophilic attack by FGH (see below). The expression and geometry of these essential active site residues are tightly conserved across the family, suggesting a shared mechanism of sulfate hydrolysis. While the sequence and geometry of the key active site residues are tightly conserved, the overall size, shape, and electrostatics of the active site pockets are extensively varied across the family, reflecting their selectivity towards their physiological substrates. The active site pocket of IduA2S is relatively wide and shallow, compared to ARSA/B, shortened by the three fewer strands of IduA2S's central  $\beta$ -sheet (153). While the active site of ARSA/B are both described as deep narrow clefts, the ASRB active site holds a higher positive charge than ARSA to accommodate its polyanionic substrate. Visual analysis of the active sites illustrates significant variation in the substrate binding pockets across the family (**Figure 31**), however, literature describing the pockets can be inconsistent. For example, the active site of ARSB is described as deep and narrow by Demydchuk *et al.*, yet "flat and open" by Rivera-Colon *et al.* (153,154). Due to their rapid activity, no co-crystal structures of sulfatases binding their natural substrates have been solved, limiting the conclusions which can be drawn on substrate binding. Therefore, while proposals for sulfatase-substrate binding have been put forward, they await experimental confirmation.

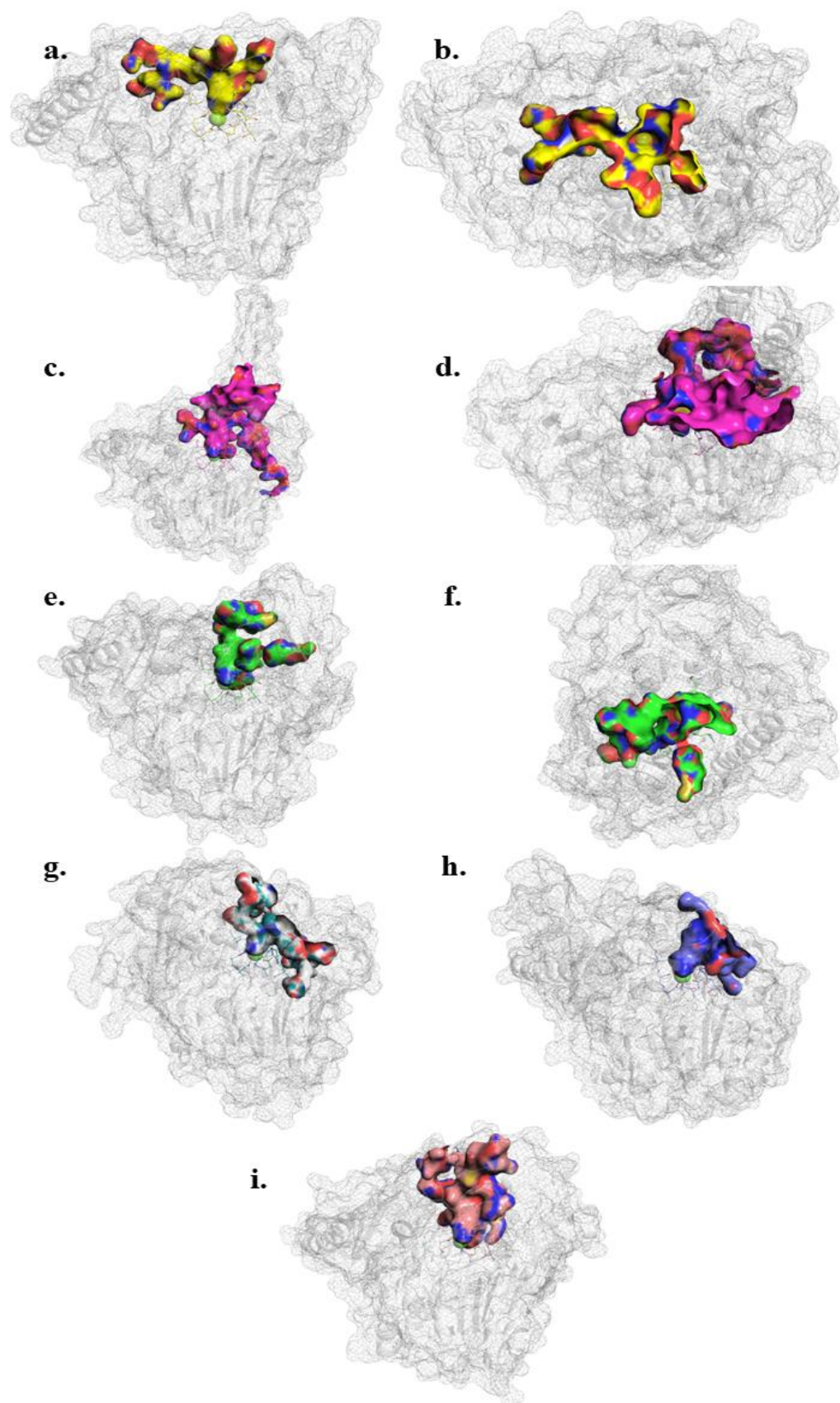
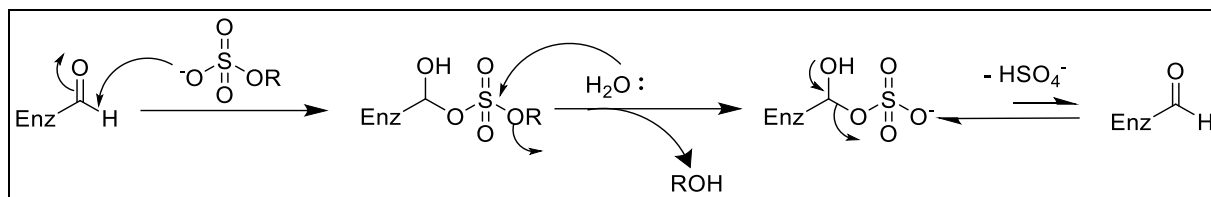


**Figure 31.** Illustrations of the contiguous substrate binding pockets of human sulfatases generated using Pymol®. **a.** ARSA (1E2S) **b.** ARSA top view. **c.** ARSB (1FSU) **d.** ARSB top view **e.** ARSC (1P49) **f.** ARSC top view **g.** IduA2S **h.** SGSH **i.** GlcN6S.

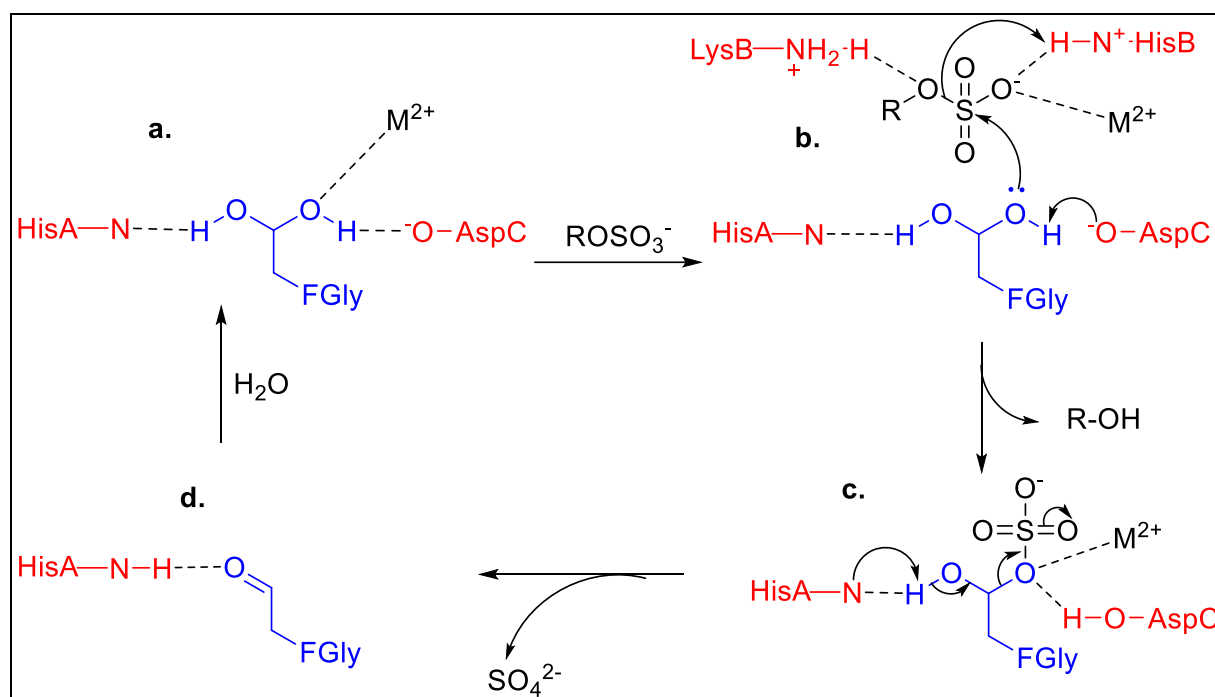
### 1.7.3 Mechanism

Initially, sulfatases were hypothesised to share an “addition-hydrolysis” mechanism (**Scheme 2**) similar to that of alkaline phosphatases (APs) due to structural similarities between these enzyme families. APs are the only known non-sulfatase enzymes containing an active site FGly, and as with sulfatases, the formation of this FGly group is directed by a core C/S-X-P-R active site sequence (161).



**Scheme 2.** Proposed Addition-Hydrolysis mechanism of sulfate hydrolysis.

The elucidation of an FGH, not FGly at resting state, suggested an alternative mechanism in which FGH acts as a nucleophile, attacking the sulfate substrate to form an intermediate and release the alcohol product in an  $S_N2$  reaction (**Scheme 3.b**). The cleavage of the sulfate-enzyme intermediate was more unclear. It was speculated to either progress through an E2 elimination by deprotonation of the remaining FGH hydroxyl group by the conserved HisA (**Scheme 3 c**) or through an  $S_N2$  substitution at the sulfur by hydroxide/water (151,152). Mutant ARSA and ARSB carrying serine in the place of FGly were exposed to radiolabelled *p*-NCS containing a  $^{35}\text{S}$  atom to probe these proposed mechanisms (162). Both mutant enzymes could bind the substrates to form the sulfate-enzyme intermediate and release *p*-nitrocatechol. However, unlike wild-type enzymes, the Ser-mutants could not cleave the labelled sulfate-enzyme intermediate. If the sulfate-enzyme intermediate was cleaved by an  $S_N2$ -like attack by water, then the serine mutant would be expected to retain at least partial activity. Additionally, a study using chiral substrates found that the substrates are stereochemically inverted when metabolised by *Aspergillus* sulfatases suggesting the substrate passes through a single  $S_N2$  transition state (163). Chiral substrates undergoing hydrolysis by an  $S_N2$ - $S_N2$  mechanism would have their stereochemistry retained. It is now generally accepted that sulfatases employ the E2 “transesterification-elimination” mechanism of sulfate hydrolysis as outlined in **Scheme 3** (139,162).



**Scheme 3.** Transesterification-elimination mechanism of sulfate hydrolysis. The FGly is illustrated in blue, and other participating residues are illustrated in red. **a.** Resting state, FGly exists as FGH (diol). The FGH is primed for nucleophilic attack by AspC. **b.** Enzyme attacks sulfate forming the sulfate-enzyme intermediate, and an alcohol product is released. **c.** E2 elimination of the remaining FGly hydroxyl group cleaves the sulfate-enzyme intermediate. **d.** Reformation of the FGly, FGH is reformed upon the addition of  $H_2O$ .

#### 1.7.4 Arylsulfatase activity

The co-crystal structure of an inactive mutant ARSA lacking the FGly modification was solved bound to the small arylsulfate *p*-NCS (162). Here, the phenyl ring of the substrate sits disordered outside the binding pocket. Therefore, suggesting that the binding site on the enzyme surface that discriminate and align their large natural substrates, does not select for, but also does not exclude small arylsulfates such as *p*-NCS.

The significant differences between human sulfatases active site pockets influences activity towards aryl substrates. The rate of hydrolysis of both *p*-NCS and MUFS varies significantly between arylsulfatase ARSA, ARSB, and ARSC **Table 2**. ARSA metabolises *p*-NCS 80-fold faster than ARSB, while the rate of MUFS hydrolysis is similar between the enzymes (139). Similarly, ARSC hydrolyses *p*-NCS at a faster rate than ARSB yet hydrolyses-MUFS significantly slower. Inclusion of two *ortho* fluorine substituents to MUFS (3,5-difluoro-4-methylumbelliferyl sulfate, DiFMUFS) influences the activity from ARSA, ARSB, and ARSC significantly differently (164). DiFMUFS has >10-fold higher affinity than its unfluorinated analogue MUFS for all three arylsulfates. The influence on rate ( $V_{max}$ ) varies significantly.

## Introduction

ARSA achieves a ~200-fold higher  $V_{\max}$ , while its lysosomal counterpart ARSB only achieves a relatively modest four-fold rise, and the  $V_{\max}$  for the non-lysosomal ARSC is reportedly 3.4-fold slower relative to MUFS despite the higher affinity (**Table 2**) (164). Clearly the structure of the arylsulfate substrates influences interaction with the varied enzymes, however very little work has focused on this arylsulfatase SAR.

**Table 2.** Rate (nM/min/mg enzyme) and affinity ( $K_m$ ) of arylsulfate probes against human arylsulfatase A-C.

Enzyme	<i>p</i> -NCS		MUFS		DiFMUFS	
	Rate (nM/min/mg enzyme)	$K_m$ ( $\mu$ M)	Rate (nM/min/mg enzyme)	$K_m$ ( $\mu$ M)	Rate (relative to MUFS) (164)	$K_m$ ( $\mu$ M)
ARSA	160,000	400	40,000	12,500	~200	503
ARSB	2,000	60	48,500	1,180	~4	190
ARSC	4,000	400	7,000	800	-3.4	85

*Rate and affinity for MUFS and pNCS taken from (139), primary literature inaccessible. Due to differences in experimental design DiFMUS  $V_{\max}$  is described relative to MUFS.*

The most significant exploration of human arylsulfatase SAR focused on development of ARSC inhibitors (165–169). These irreversible inhibitors undergo the initial  $S_N2$  transesterification step but instead form a sulfamate-enzyme intermediate that cannot be cleaved. Importantly, this initial reaction is the rate limiting step for sulfatase activity. Various inhibitor structures have been explored, demonstrating remarkably non-specific binding interactions for arylsulfamates. Analysis of a series of phenol sulfamates ( $Ar-OSO_2NH_2$ ) found that the most potent inhibitors contained phenolic leaving groups with an optimal  $pK_a$  of 8 for the series (166,167). Hydrophobicity also improved activity, potentially due to increased non-polar interactions on the enzyme's surface (165,169). However, the influence of hydrophobicity may be heightened in the case of the membrane bound ASRC. The selectivity of these inhibitors against other arylsulfatases has not been reported. Therefore, given the general arylsulfatase activity across the family, it can be speculated this pharmacophore would have activity outside of ARSC alone. However, ARSC is especially different to other arylsulfates. ARSC is a non-lysosomal sulfatase, instead existing bound within the membrane of the rough endoplasmic reticulum. Consequently, the pH optimum of ARSC (pH 7) is significantly higher than the lysosomal sulfatases (pH 4-6). The active site pocket of ARSC is significantly less polar than other family members. The active pocket is lengthened by two transmembrane regions, potentially acting as gatekeeping domains by recognising substrates and directing them to the active site gorge close to the membrane surface (139,149). ARSC is the only human

## Introduction

sulfatase to target arylsulfates as their physiological substrates (**Figure 29**). Ultimately, ARSC is significantly different to other arylsulfatases in structure, substrate selection and cellular location.

Studies of bacterial sulfatases and isolated *Helix pomatia* (garden snail) arylsulfatase against various aryl substrates concluded electron withdrawal away from the arylsulfate enhanced activity (139,143). Presumably, electron withdrawal increases the rate of the initial S<sub>N</sub>2 reaction by both priming the sulfate for nucleophilic attack and decreasing the pK<sub>a</sub> of the released phenol making it a better leaving group. The snail arylsulfatase also favoured larger bi- and tri-cyclic substrates, perhaps due to increased hydrophobic binding. However, the snail arylsulfatase is characterised by its substrate promiscuity potentially making it a poor model for the more selective human sulfatases

The arylsulfatase SARs described to date have highlighted the importance of the pK<sub>a</sub> of the phenolic leaving group however, these reports have been carried out on sulfatases which poorly represent the general features of human arylsulfatases as described above. Given the significant differences in the substrate binding pockets (**Figure 31**), and the efficacy against arylsulfates probes (**Table 2**), suggest that aryl-substrate SARs may differ significantly between enzymes and exploration of other human sulfatases is required.

### 1.7.5 Human arylsulfatase A (ARSA)

ARSA was among the first sulfatases discovered and has been extensively characterised (139,142,151). As a lysosomal sulfatase, its activity is optimum under acidic conditions at pH 5 where the enzyme exists as a highly stable octamer. ARSA illustrates the highest activity towards the arylsulfate probes *p*-NCS and 4-MUS among human sulfatases (139,170,171). Consequently, ARSA is of particular interest to the development of arylsulfatase prodrugs, including ADC linkers, given its especially high arylsulfatase activity and lysosomal location. To date, there is a current knowledge gap in understanding the SAR of ARSA arylsulfate ester metabolism that is yet to be explored.

The structure of ARSA is well defined as several crystal structures of the enzyme have been solved (151,157,160,162). The structure is generally consistent with the class (**Section 1.7.1**), ARSA is a globular enzyme of mixed  $\alpha\beta$  topography and includes a C-terminal meander motif which helps to define the substrate binding pocket. Unique among the human lysosomal sulfatases, hARSA hydrolyses lipid substrates cerebroside-3-sulfate (sulfatide), seminolipid-

3S, and psychosine-3S (**Figure 29**). All other lysosomal sulfatases act on glycosaminoglycans (GAGs) (139). Sulfatide is an essential sphingolipid component of myelin, and ARSA deficiency is responsible for the demyelination and leukodystrophy observed in metachromatic leukodystrophy disorder (139,172). Unlike other sulfatases, ARSA requires a co-factor, Saponin B, to aid the proper binding and metabolism of its natural hydrophobic lipid substrates to the hydrophilic enzyme, although this co-factor is not necessary for arylsulfate substrates (173). Despite its non-aryl substrate ARSA retains the generic name arylsulfatase due to its initial characterisation. However, this remains somewhat fitting as ARSA had the highest arylsulfatase activity towards common synthetic arylsulfate ester probes *p*-NCS, MUFS and DiFMUFS (**Table 2**) (170).

### 1.8 This work

The evolution of targeted drug delivery therapies such as ADCs creates a need for development of new mechanisms to achieve selective drug release. Enzyme cleavable linkers are an attractive approach due to their selectivity towards specific enzymes in their target environment, however, established linkers such as dipeptide linkers have shortcomings including hydrophobicity and instability in rodent plasma (30). Sulfatase cleavable linkers are a promising lead in the development of novel enzyme cleavable linkers due to their hydrophilic character, prolonged plasma stability, variety of potential activating enzymes, and efficacy when applied to ADCs *in vitro* (138). However, the factors that influence sulfate hydrolysis and payload release have not been explored and the arylsulfatase activity of this family of enzymes is poorly understood. Knowledge of the ARSA arylsulfate ester SAR could be applied to development of more effect sulfatase cleavable linkers or other ARSA arylsulfate prodrugs.

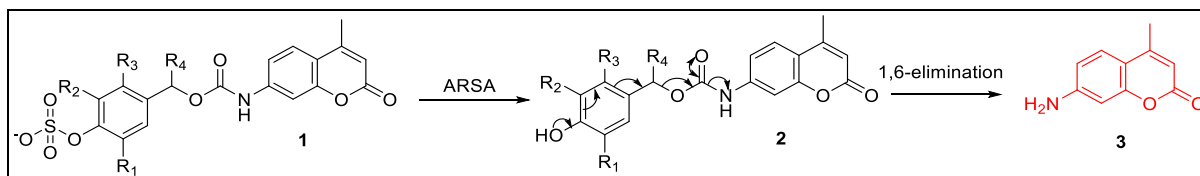
This study aims to synthesise a library of related model sulfatase cleavable linkers with the general structure **1** (**Scheme 4**). The fluorescent probe 7-amino-4-methylcoumarin (**AMC**, **3**) employed as a model payload allowing release to be monitored by fluorimetry and UV-vis spectroscopy. **AMC** is a commonly used fluorescent probe in proteolytic enzyme assays. Fluorescence is quenched by functionalisation of the aniline with electron-withdrawn groups (e.g., as part of the model linker **1**) and returned once released as a free **AMC**.

This library will be applied to an enzyme activity assay using ARSA in the aim of developing an empirical structure activity relationship between the rates of sulfate hydrolysis and payload



## Introduction

release. Hydrolysis of sulfate **1** by ARSA will ignite by the 1,6-elimination of phenol **2** to release the **AMC** payload (**3**).



**Scheme 4.** Hydrolysis and fragmentation of model arylsulfatase cleavable linkers.

It is hypothesised that structural features of the linkers will influence sulfate hydrolysis and payload release independently. It is expected that the electronic character of the parent phenol will influence both the sulfate hydrolysis and subsequent fragmentation. It is also expected that strong electron withdrawing substituents in the R<sub>1</sub>, R<sub>2</sub>, and R<sub>3</sub> positions may accelerate sulfate hydrolysis but hinder the rate of elimination.

It is envisaged that this empirical SAR against a human arylsulfatase will aid in the development of more efficacious sulfatase cleavable linkers for application to a variety of ADCs or indeed other targeted drug-delivery strategies.

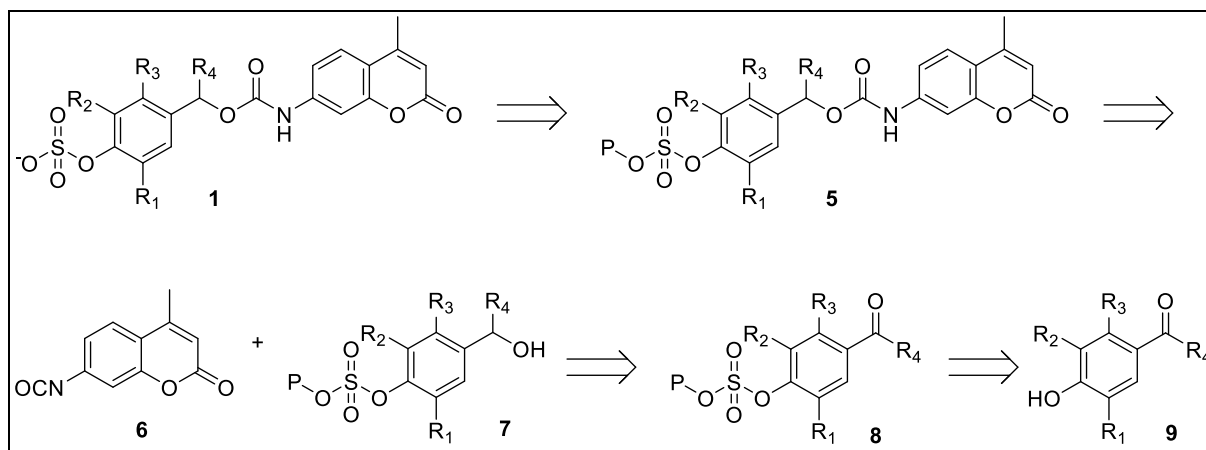
# Chapter 2: Discussion

## 2. Discussion

### 2.1 Synthesis

#### 2.1.1 Synthetic objectives

This project aims to synthesise a series of substituted *para*-sulfoxybenzyl carbamate linkers **1** as model sulfatase cleavable linkers. The retrosynthesis of **1** is shown in **Scheme 5**.



**Scheme 5.** Retrosynthesis of sulfates **1a-z** from phenols **9a-z**.

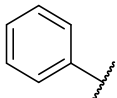
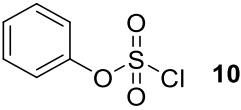
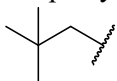
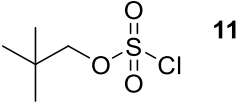
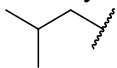
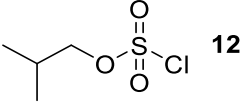
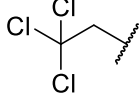
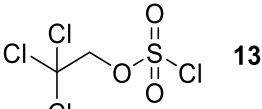
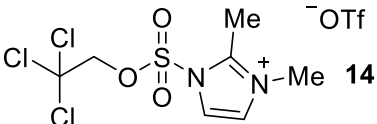
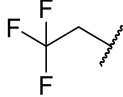
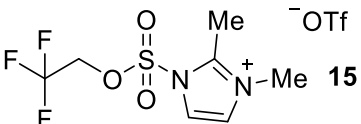
The sulfate functionality is typically installed in the final step of synthesis as their anionic nature limits solubility in organic solvents and hinders purification by normal phase silica gel chromatography. In this project, the sulfate functionality must be installed prior to the formation of the carbamate linker, as the *para*-hydroxy benzyl carbamate **2** is, by design, unstable (**Scheme 4**). Instead, an approach was envisioned whereby the sulfate functionality is introduced as a protected diester earlier in synthesis, followed by deprotection to unveil the sulfate monoester in the final step. Following this approach, a disconnection can be made through the carbamate creating two fragments: the known coumarin isocyanate **6** (138,174–176) and the other benzyl alcohol **7**. Benzyl alcohol **7** can be prepared from commercially available phenols **9** following the introduction of the protected sulfate diester and subsequent deprotection of the benzaldehyde or ketone **8**.

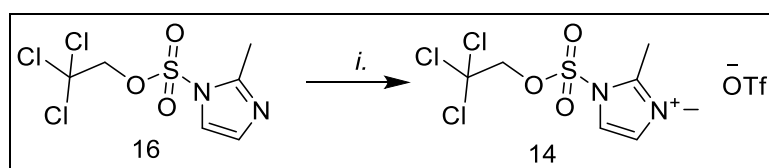
Several strategies have been reported for the conversion of alcohols to sulfate diesters as precursors in the synthesis of sulfate monoesters (**Table 3**). Phenyl-protected sulfate diesters have been employed in the synthesis of aliphatic sulfates; however, they are incompatible with the synthesis of arylsulfate monoesters due to their deprotection conditions (177). Here the

## Discussion

diester is cleaved by hydrogenation of the benzyl ring using PtO<sub>2</sub>/H<sub>2</sub> followed by treatment with a strong base (177). Widlanski *et al.* reported the use of neopentyl chlorosulfate **11** and isobutyl chlorosulfate **12** to prepare sulfate diesters, followed by deprotection to afford arylsulfates in good yields (178). Neopentyl sulfate diesters are stable to acidic and basic conditions, hydrogenation, and storage at room temperature. Isobutyl sulfate diesters are stable to hydrogenation but unstable to acids, bases, and storage at room temperature. The isobutyl-protecting group can be deprotected with sodium iodide in hot (55 °C) acetone. Due to their higher stability, neopentyl sulfate diesters are deprotected with harsher conditions, requiring azide or cyanide in hot (60-70 °C) DMF overnight. Bargh *et al.* successfully applied the neopentyl protecting strategy to prepare their sulfatase cleavable linkers. More recently, Desoky *et al.* reported using 2,2,2-trichloroethyl (TCE) and trifluoroethyl (TFE) sulfate diesters to synthesise arylsulfate monoesters (179–181). TCE-sulfate diesters are stable to acids and weak bases but are reactive towards nucleophiles and strong acids. TCE-protected sulfates can be deprotected in >80% yields by either zinc or 10% Pd/C and ammonium formate; however, this strategy may not be compatible with functional groups sensitive to reducing reagents (182). TCE-protected sulfate diesters can be prepared by reaction of alcohols with TCE-chlorosulfate **13** (182), or sulfuryl imidazolium salt **14** (179), the latter providing selectivity over aliphatic alcohols. TFE-sulfate diesters can be prepared from pyridine/SO<sub>3</sub> followed by 2,2,2-trifluorodiazaoethane; however, this reagent must be freshly prepared, is highly toxic, and potentially explosive (183). Deprotection with strongly basic KO*t*-Bu is incompatible with the synthesis of arylsulfate monoesters. Instead, Desoky *et al.* have prepared an alternative strategy employing a TFE-sulfurylimidazolium salt **15** and deprotection with NaN<sub>3</sub> in hot (65-70 °C) DMF suitable for the synthesis of arylsulfate monoesters (179,180). TFE-protected sulfates were stable in the presence of organic acids, are thermally stable but are unstable in the presence of mineral acids and hydrogenation conditions. It was envisioned that TCE protection would apply to most of the library due to the mild deprotection conditions. The neopentyl protecting strategy could be employed for targets including functional groups sensitive to reducing agents such as nitro functionality.

**Table 3.** Arylsulfate ester protecting strategies. Conditions from respective references above.

Protecting strategy (Pg)	Installation Conditions
Phenyl 	 <b>10</b> <b>10</b> , NaH, N <sub>2</sub> , oxolane, rt, 20 h, 75%
Neopentyl 	 <b>11</b> <b>11</b> , NaH or NAHMDS, DMPU, THF, -75 °C, 80%
Iso-butyl 	 <b>12</b> <b>12</b> , NaHMDS, THF, -10 °C, 95%
TCE 	 <b>13</b> <b>13</b> , Et <sub>3</sub> N, 4-DMAP, THF, rt, 10 h, 90%
	 <b>14</b> 1.2 eq. <b>14</b> , DBU, THF, rt Phenol selective >80%
TFE 	 <b>15</b> 2 eq. <b>15</b> , 2.5 eq. 1,2-dimethylimidazole, DCM, 24 h, 78%

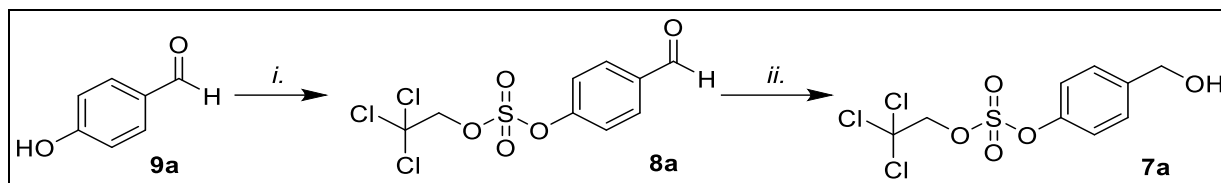
**2.1.2 Synthesis of sulfonyl imidazolium salt 14**

**Scheme 6.** Methylation of imidazole sulfonate **14**. *i.* MeOTf, Et<sub>2</sub>O, 0 °C, 2 h, 90%.

Given the potential for selective phenol sulfation, **14** was synthesised from the precursor imidazole **16**, which had previously been prepared in-house following literature procedures (181). Imidazole **16** was readily methylated with methyl triflate following conditions set out in Ingram *et al.* (**Scheme 6.**) (181).

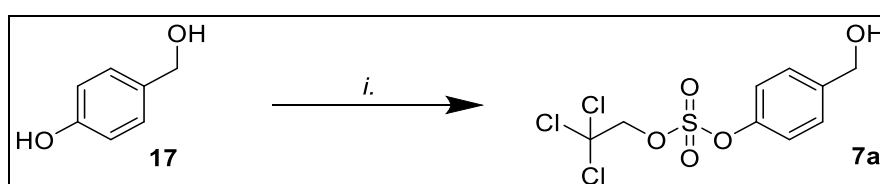
### 2.1.3 Synthesis of 7a

The first synthetic target was the unsubstituted ( $R_{1-3}=H$ ) analogue **7a**. Two different routes were used to prepare this compound.



**Scheme 7.** Preparation of **7a** from **9a**. *i.* 1.2 eq. **14**, 2.5 eq. 1,2-dimethylimidazole, 0 °C DCM, 89%.  
*ii.* 2 eq. NaBH<sub>4</sub>, MeOH, 70%.

Aldehyde **9a** was reacted with **14** and 1,2-dimethylimidazole in 0 °C DCM as set out in Ingram *et al.* (**Scheme 7.**) (181). Following aqueous workup, aldehyde **8a** was purified by column chromatography to give the desired product an 82% yield. The <sup>1</sup>H NMR spectrum was consistent with the expected structure, including the presence of a characteristic two-proton singlet at 4.87 ppm arising from the methylene of the trichloroethyl group. The subsequent reduction with sodium borohydride (NaBH<sub>4</sub>) was challenging to monitor by TLC analysis as alcohol **7a** was not readily visualised under UV light. Following an aqueous workup, **7a** was purified by column chromatography to give the desired product in a lower-than-expected yield (40%) (179). Staining the TLC plate with potassium permanganate bleached the desired product allowing the reaction and purification to be more readily monitored. A repeat reaction with a longer reaction time improved the yield to 70%.



**Scheme 8.** Preparation of alcohol **7a** from **17**. *i.* 1.2 eq **14**, 2.5 eq. DBU, DCM, 0 °C to rt, 2 h, 46%.

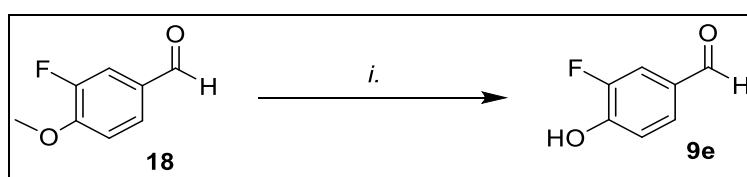
Next, the phenol selectivity of reagent **14** was assessed. Alcohol **7a** was prepared from hydroxymethyl phenol **17** with **14** and 1,8-diazabicyclo[5.4.0]undec-7-ene (DBU) in DCM as set out in Taylor and Desoky (179) (**Scheme 8.**). Following aqueous workup, the crude material was purified by column chromatography to give **7a** in a 46% yield. The product was confirmed to be **7a** by comparison of TLC analysis and the <sup>1</sup>H NMR spectrum with the authentic product produced from **9a**.

## Discussion

Overall, the yield starting from benzaldehyde **9a** (57%) proved higher than via the reaction with phenol **15** (46%). No by-products were isolated from the reaction with **17**, suggesting the low yield was not due to the side reaction of the aliphatic alcohol. Taylor and Desoky (179) reported a significantly higher yield (84%) preparing **7a** from phenol **17**, suggesting the lower yield was likely due to a technical error and could be optimised.

### 2.1.4 Synthesis of 7b-h

**8b-h** were prepared from their corresponding commercially available phenols **9a-d,f-h**. **9e** was prepared *via* demethylation of **18** in aqueous HBr (Scheme 9).



**Scheme 9.** Preparation of phenol **9e** from methoxy benzaldehyde **18**. *i.* 48% HBr, 82%.

Experimentation employing DBU in preference to 1,2 dimethylimidazole provided comparable yields with a significant advantage in handling the reagent in liquid form versus 1,2- dimethylimidazole, a low melting point solid. Reaction yields are summarised in **Table 4**.

**Table 4.** Summary of reactions in preparation of **7a-k**.

Compound	Sulfation yield	Reduction yield
<b>a</b> ( $R_1 = R_2 = R_3 = R_4 = H$ )	82%	76%
<b>b</b> ( $R_1 = Me, R_2 = R_3 = R_4 = H$ )	72%	74%
<b>c</b> ( $R_1 = OMe, R_2 = R_3 = R_4 = H$ )	78%	76%
<b>d</b> ( $R_1 = F, R_2 = R_3 = R_4 = H$ )	55%	88%
<b>e</b> ( $R_1 = NO_2, R_2 = R_3 = R_4 = H$ )	64%	88%
<b>f</b> ( $R_1 = R_2 = F, R_3 = R_4 = H$ )	62%	72%
<b>g</b> ( $R_1 = CF_3, R_2 = R_3 = R_4 = H$ )	73%	36%
<b>h</b> ( $R_2 = Me, R_1 = R_3 = R_4 = H$ )	74%	NA
<b>i</b> ( $R_2 = OMe, R_1 = R_3 = R_4 = H$ )	65%	89%
<b>j</b> ( $R_2 = F, R_1 = R_3 = R_4 = H$ )	NC	NA
<b>k</b> ( $R_1 = R_2 = R_4 = H, R_3 = Me$ )	0%	NA

NA – reaction not attempted, NC- reaction not characterised due to time constraints.

*i.* 1.2 eq. 43, 2.5 eq. DBU, DCM, rt, 2 h. *ii.* 2 eq. NaBH<sub>4</sub>, MeOH, rt, 2 h. Percentages represent isolated yields.

## Discussion

Generally, these reactions were easily monitored by TLC with permanganate staining and could be readily purified by column chromatography.  $^1\text{H}$  NMR, attached proton test (APT)  $^{13}\text{C}$  NMR and 2D NMR (heteronuclear multiple quantum correlation (HSQC) and heteronuclear multiple bond correlation (HMBC) analysis or analogy confirmed the identity of the sulfate diesters. All sulfate diesters included a characteristic peak corresponding to the methylene of the trichloroethyl group at  $\sim 5$  ppm ( $^1\text{H}$  NMR) and  $\sim 80$  ppm ( $^{13}\text{C}$  NMR), as well as signals between 6.9 and 8 ppm consistent with the aromatic substituents. All attempts to collect high-resolution mass spectra of these compounds were unsuccessful. However, low-resolution mass spectra of these compounds were obtained, reporting masses  $\sim 35$  g/mol higher than expected with the appropriate splitting for chlorine isotopes included in the trichloroethyl moiety. This suggests the compounds were flying as chlorine adducts.

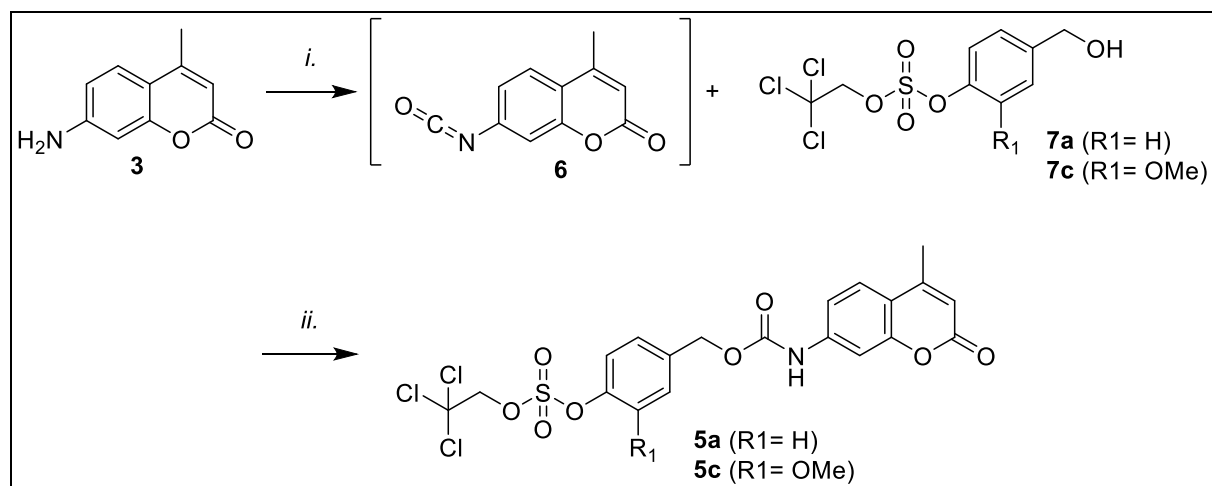
Not every reaction progressed without issue. The first attempt to synthesise benzaldehyde **8d** yielded a by-product for which retention by TLC and signal in the low-resolution mass spectrum were consistent with expectations. However, the  $^1\text{H}$  NMR spectrum analysis showed the product lacked the characteristic trichloroethylene singlet at  $\sim 5$  ppm. Only a small amount of the desired product could be isolated by repeated column chromatography using alternative solvent mixtures. The batch of reagent **14** used for this reaction had been left at ambient conditions for  $>6$  months during the August 2021 Covid-19 lockdown and subsequent leave of absence, and we considered it may have degraded. A repeat reaction with freshly prepared **14** afforded the target **8d** in higher yield without the by-product, although the reaction did not proceed to completion. Sulfation of **9k** produced acetophenone **8k** as the minor product and an unidentified by-product with the same  $R_f$  by TLC analysis. Formation of **8f** progressed slowly and did not run to completion over 4 hours, yielding 27% of the desired product after isolation. The recovered **9f** was returned to the reaction with increased equivalents of **14**, resulting in an improved 62% yield.

All reductions progressed in acceptable yields, and products were purified by column chromatography and structure confirmed by the presence of a characteristic  $\sim 4.7$  ppm ethyl singlet. The exception was benzyl alcohol **7g**, where co-eluting impurities impeded isolation of the desired product resulting in a diminished 37% recovery of the pure product; however, enough mass was collected to progress with the synthesis. Benzaldehyde **8k** was not reduced due to the low mass collected and the analogue was abandoned.



### 2.1.5 Synthesis of **5a** and **5c**

With the alcohols **7a** and **7c** in hand, the arylsulfate triggers were to be conjugated to the payload **AMC** via a carbamate linker. The **AMC** aniline is a poor nucleophile and is unlikely to be competent for reaction with a mixed carbonate. Instead literature precedent suggested that the best method would be exposure of **AMC** to triphosgene **19** to form isocyanate **6** as a highly reactive intermediate, followed by the addition of **7** to form **5** (**Scheme 10.**) (138,174–176).

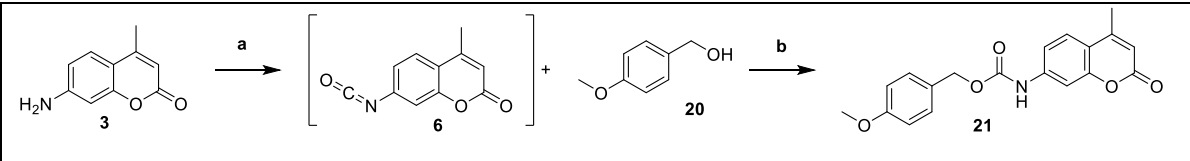


**Scheme 10.** Initial preparation of **5a** and **5c**. *i*. 0.4 eq. triphosgene **19**, dry toluene, reflux, 2 h. *ii*\*. **7**, 0.1 eq., THF, rt, overnight. \* 0.1 equivalents of dibutyltin diacetate included in the synthesis of **5a**.

Formation of the carbamates **5a** and **5c** proved less facile than anticipated. 0.4 equivalents of **19** were stirred in dry toluene at reflux with 1.2 equivalents of **AMC** for 2 hours. Then the reaction was cooled to room temperature and purged of phosgene with N<sub>2</sub>. Alcohol **7c** was added in dry THF, and the mixture was stirred at room temperature overnight. Additional care was taken when handling **19** and when purging due to the risk of phosgene toxicity. LRMS and TLC indicated **5c** was a minor component while both **AMC** and **7c** remained. Previous literature suggested the inclusion of a tin catalyst to facilitate the reaction through an organotin alkoxide intermediate(138,184,185). Including 0.1 equivalents of dibutyltin diacetate in the reaction of **7a** and stirring over three days saw no improvement.

### 2.1.6 Model carbamate formation

To find suitable conditions for the carbamate formation, a model study was conducted employing methoxybenzyl alcohol **20**, **19**, and **3** to prepare carbamate **21** (**Table 5.**). Literature conditions for this type of transformation varied in the solvent employed, the inclusion of a base and catalyst, and order of reagent addition (138,174–176,184,185).

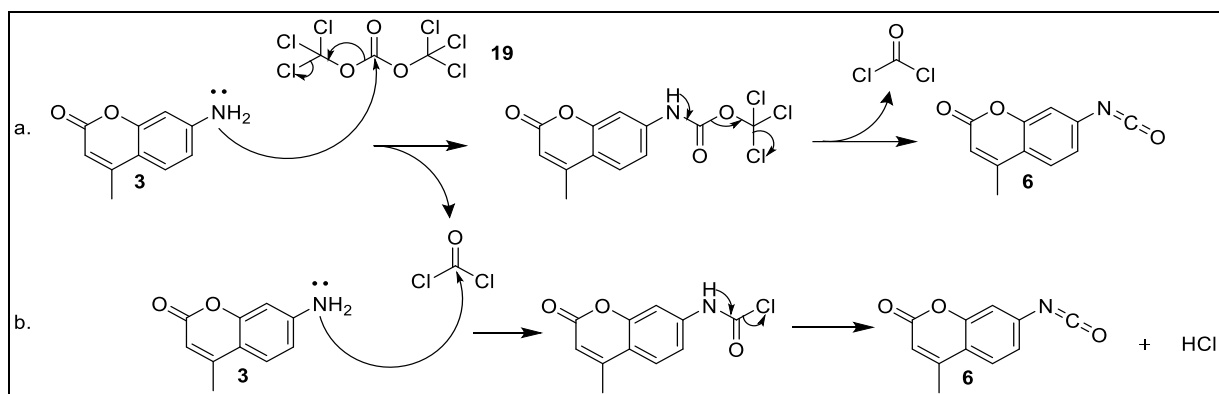
**Table 5.** Summary of reaction conditions for preparation of **21**.


Conditions A	Conditions B	Yield
1.1 eq. <b>AMC</b> , 0.4 eq. <b>19</b> , toluene, reflux	0.1 eq. dibutyltin diacetate, THF	4%
1.1 eq. <b>AMC</b> , 0.4 eq. <b>19</b> , THF, 80 °C	0.1 eq. dibutyltin diacetate, THF	No reaction
1.1 eq. <b>AMC</b> , 0.4 eq. <b>19</b> , THF, 80 °C sealed tube	0.1 eq. dibutyltin diacetate, THF	No reaction
1.1 eq. <b>AMC</b> , 0.4 eq. <b>19</b> , toluene, 117 °C sealed tube	0.1 eq. dibutyltin diacetate, THF	10%
1.1 eq. <b>AMC</b> , 0.4 eq. <b>19</b> , 3 eq. Et <sub>3</sub> N, toluene, 117 °C sealed tube	0.1 eq. dibutyltin diacetate, THF	71%
1.1 eq. <b>AMC</b> , 0.8 eq. <b>19</b> , 3 eq. Et <sub>3</sub> N, toluene, 117 °C sealed tube	0.1 eq. dibutyltin diacetate, THF	82%

*Yields calculated from NMR analysis of crude material following workup.*

*Bargh et al.* prepared similar model linkers with yields up to 92% using a tin catalyst but without a base. **AMC** isocyanate **6** was prepared in refluxing toluene, and the subsequent reaction with alcohol and the catalyst was carried out in THF (138). Repeating the conditions from *Bargh et al.* only achieved a yield of 4%, and no reaction was observed refluxing **3** in THF. Fearing phosgene was escaping the reaction, these reactions were repeated in sealed tubes, increasing the yield in toluene to 10%. *Morihiro et al.*(174) included a base, DIPEA, with **19** to form the isocyanate **6**. Including three equivalents, Et<sub>3</sub>N significantly increased the observed yield to 71%. Presumably, the base buffers the reaction from HCl released as a by-product of the phosgene reaction (**Scheme 11**). Finally, doubling the equivalents of **19** to 0.8 increased the yield to 82%.

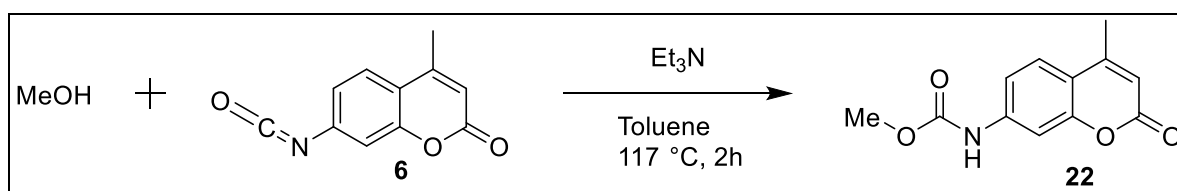
## Discussion



**Scheme 11.** Mechanism of reaction of AMC **3** and triphosgene **19** to prepare isocyanate **6**. **a.** Reaction of one equivalent of **19** produces an isocyanate and two equivalents of phosgene. **b.** Phosgene reacts with **3** to afford isocyanate **6** and HCl.

### 2.1.7 Resynthesis of **5a** and **5c**

These optimised conditions were successfully applied to the synthesis of **5a** and **5c**. **5a** was left stirring at room temperature for 2 months, then rested at room temperature for a further 4 months during the 2021 August Covid-19 lockdown and period of absence. Both reactions were colourless solutions with a thick white precipitate. Both **5a** and **5c** suspensions were filtered through diatomaceous earth and flushed with EtOAc, and the filtrates were then collected and concentrated *in vacuo*. The crude extracts were insoluble suspensions in EtOAc, DCM, and DCM-MeOH, with the desired carbamate present in both the filtrate and precipitate. Attempts to dry load and purify the carbamates by column chromatography were unsuccessful due to the presence of a shared fluorescent impurity streaking through both columns. Removal of this impurity proved difficult. Neither **5a** or **5c** could be purified by repeat chromatography or crystallisation from EtOAc (which had previously been used to purify **5a** in the laboratory). The impurity was removed by trituration in MeOH, and collected as a white solid by filtration. This shared impurity was identified as the methylcarbamate **22** following analysis of an authentic sample (**Scheme 12.**) with  $^1\text{H}$  NMR matching reported literature (186).



**Scheme 12.** Synthesis of an authentic sample of the common impurity methylcarbamate **22**.

## 2.1.8 Synthesis of 5a-i

**Table 6.** Summary of reactions in preparation of **5a-g, i**.

Compound	Yield
<b>5a</b> (R <sub>1</sub> = R <sub>2</sub> = R <sub>3</sub> = R <sub>4</sub> = H)	28%
<b>5b</b> (R <sub>1</sub> = Me, R <sub>2</sub> = R <sub>3</sub> = R <sub>4</sub> = H)	44%
<b>5c</b> (R <sub>1</sub> = OMe, R <sub>2</sub> = R <sub>3</sub> = R <sub>4</sub> = H)	54%
<b>5d</b> (R <sub>1</sub> = F, R <sub>2</sub> = R <sub>3</sub> = R <sub>4</sub> = H)	7%
<b>5e</b> (R <sub>1</sub> = NO <sub>2</sub> , R <sub>2</sub> = R <sub>3</sub> = R <sub>4</sub> = H)	34%
<b>5f</b> (R <sub>1</sub> = R <sub>2</sub> = F, R <sub>3</sub> = R <sub>4</sub> = H)	Impure
<b>5g</b> (R <sub>1</sub> = CF <sub>3</sub> , R <sub>2</sub> = R <sub>3</sub> = R <sub>4</sub> = H)	Impure
<b>5i</b> (R <sub>2</sub> = OMe, R <sub>1</sub> = R <sub>3</sub> = R <sub>4</sub> = H)	39%

*i.* 1.1 eq. AMC, 0.8 eq. **19**, 3 eq. Et<sub>3</sub>N, toluene, 117 °C sealed tube, *ii.* **5a-i**, 0.1 eq. dibutyltin diacetate, THF.

The yields for the synthesis of **5a-i** are summarised in

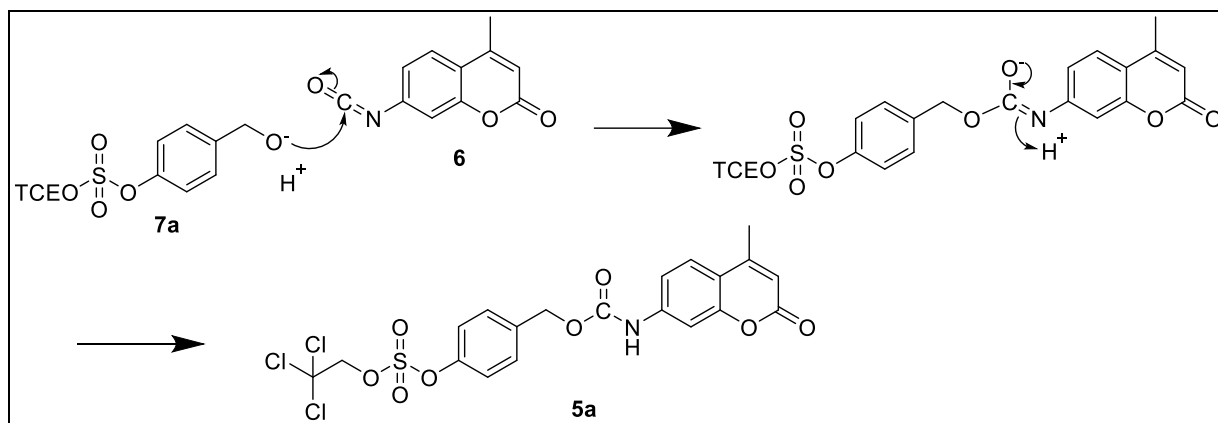
**Table 6.** Modest yields were achieved across the library; however, enough of each compound was obtained to continue to the final step. All reactions generated impurity **22** despite efforts to mitigate its formation. LRMS analysis taken following phosgene purging found **22** had been formed before the addition of **7d-i**. New stocks of triphosgene, dry toluene, and Et<sub>3</sub>N were used without change. For the formation of **5d**, AMC was first suspended in DCM and then the solvent was removed *in vacuo* overnight before this reaction to remove any MeOH present. Following the standard procedure, the reaction yielded a brown suspension, unlike the white suspensions for all previous carbamate formations. Following the workup, residual alcohol **7d** and AMC were recovered as well as impurity **22** with only a small quantity of carbamate **5d**, achieving an overall 7% yield.

There is a negative relationship between the presence of electron-withdrawing substituents and carbamate yield. Indeed, **5d-g** achieved the lowest yields

**Table 6.**) and increased amount of AMC was recovered relative to previous carbamate formation reactions. Low conversion in this step meant **5f** and **5g** could only be isolated as mixtures with AMC, which were carried through to deprotection. Electron-withdrawing groups pull electrons away from the alcohol, reducing its nucleophilicity. The relevance of this effect was illustrated by the increased yield of **5c**, including an electron-donating methoxy substituent

## Discussion

that primed the alcohol for nucleophilic attack by the isocyanate (**Scheme 13**). Interestingly, the movement of the methoxy substituent from the R<sub>1</sub> position (**5c**) to the R<sub>3</sub> (**5i**) position was accompanied by a significant reduction in yield. The **5c** alkoxide is more nucleophilic than the alkoxide of **5i** due to the resonance donation from the **5c** methoxy group increasing electron density around the alkoxide. The methoxy group of **5i** is unable to donate electrons to the alkoxide through resonance from the R<sub>3</sub> position.



**Scheme 13.** Mechanism of carbamate **5a** formation from benzyl alcohol **7a** and AMC isocyanate **6**. TCEO represents the trichloroethyl protecting group.

### 2.1.9 Synthesis of **1a-g,i**

Finally, carbamates **5a-g,i** were deprotected to afford the target sulfates **1a-g,i** as ammonium salts (**Table 7**). Carbamates **5a-c** were readily deprotected with zinc dust and ammonium formate in DMF to afford sulfates **1a-c**. It was presumed that the isolated sulfate esters exist as ammonium salts; however, this was not confirmed. Sulfates **1a** and **1c** were produced in excellent yields and purified by column chromatography (82% and 87%, respectively, **Table 7**). *ortho*-methyl-sulfate **1b** could not be purified by column chromatography, but the concentrated fractions were triturated with EtOAc collecting the target sulfate as a white solid with high purity albeit in a diminished yield (**Table 7**). The structures were confirmed by analysis of the <sup>1</sup>H NMR spectra with loss of the trichloroethylene singlet at ~5 ppm, a key signifier, and the corresponding CH<sub>2</sub> peak at ~80 ppm absent from <sup>13</sup>C NMR spectra. HRMS identified the sulfate ions in negative-mode, and the final purity was confirmed by HPLC.

**Table 7.** Summary of reactions in preparation of **1a-g, i**.

Compound	Deprotection	Purity
<b>a</b> (R <sub>1</sub> = R <sub>2</sub> = R <sub>3</sub> = R <sub>4</sub> = H)	82%	98%
<b>b</b> (R <sub>1</sub> = Me, R <sub>2</sub> = R <sub>3</sub> = R <sub>4</sub> = H)	44%	98%
<b>c</b> (R <sub>1</sub> = OMe, R <sub>2</sub> = R <sub>3</sub> = R <sub>4</sub> = H)	87%	95%
<b>d</b> (R <sub>1</sub> = F, R <sub>2</sub> = R <sub>3</sub> = R <sub>4</sub> = H)	25% <sup>1</sup>	95 %
<b>e</b> (R <sub>1</sub> = NO <sub>2</sub> , R <sub>2</sub> = R <sub>3</sub> = R <sub>4</sub> = H)*	45%	96%
<b>f</b> (R <sub>1</sub> = R <sub>2</sub> = F, R <sub>3</sub> = R <sub>4</sub> = H)	25 <sup>1</sup>	97%
<b>g</b> (R <sub>1</sub> = CF <sub>3</sub> , R <sub>2</sub> = R <sub>3</sub> = R <sub>4</sub> = H)	22%	98%
<b>i</b> (R <sub>2</sub> = OMe, R <sub>1</sub> = R <sub>3</sub> = R <sub>4</sub> = H)	62%	95%
<b>l</b> (R <sub>1</sub> = NH <sub>2</sub> , R <sub>2</sub> = R <sub>3</sub> = R <sub>4</sub> = H)	failed	-

*Yield from impure reagents, calculated accounting all mass to the target reagent. i. 4 eq. Zn Dust, 6 eq. NH<sub>4</sub>HCO<sub>2</sub>, DMF. \* 10% wt. 10% Pd/C, 6 eq. NH<sub>4</sub>HCO<sub>2</sub>, DMF*

Expecting these reductive conditions to reduce the nitro group of **5e**, alternative deprotection conditions using 10% weight, 10% Pd/C and ammonium formate were used (182). Initially, these conditions did not afford any deprotection, although increasing the reaction temperature to 70 °C and adding additional Pd/C to 60% (w/w) and accompanying addition of 36 equivalents ammonium formate rapidly formed sulfate **1e**, which was purified by column chromatography. Following this success, **5e** was submitted to reductive Zn conditions to attempt to afford **1l**; however, even with a large excess of reagents and heat, no reaction product was observed by TLC and LRMS analysis.

## 2.2 Enzyme activity assays

### 2.2.1 Enzyme condition

Purified recombinant human arylsulfatase A, (ARSA) was produced by Dr James Dickson at the School of Biological Sciences, University of Auckland. Protein aliquots were prepared and stored at -4 °C in TRIS buffer. Stock solutions of ARSA were received in 2020 and activity was assessed through conversion of MUFS to the hydrolysis product over time. MUFS (50 μM) and ARSA (50 μM/mL) were incubated in formate buffer at pH 4.5 and 37 °C to model the physiological conditions of the lysosome. During this project this MUFS assay was repeated to compare the enzyme condition between 2020 and 2022. Compared to the 2020 results there was a significant decrease in the percentage of MUFS hydrolysed after 2 hours

( $P=0.045$ ). In 2020 29.8 % (7.45  $\mu\text{M}/\text{h}$ ) MUFS was hydrolysed over two hours, and this dropped to only 12.0 % (3  $\mu\text{M}/\text{h}$ ) in 2022, a 59.8% reduction in activity under the same conditions. The lost activity was attributed to degradation of the enzyme from storage in the freezer over time (**Figure 32.**).

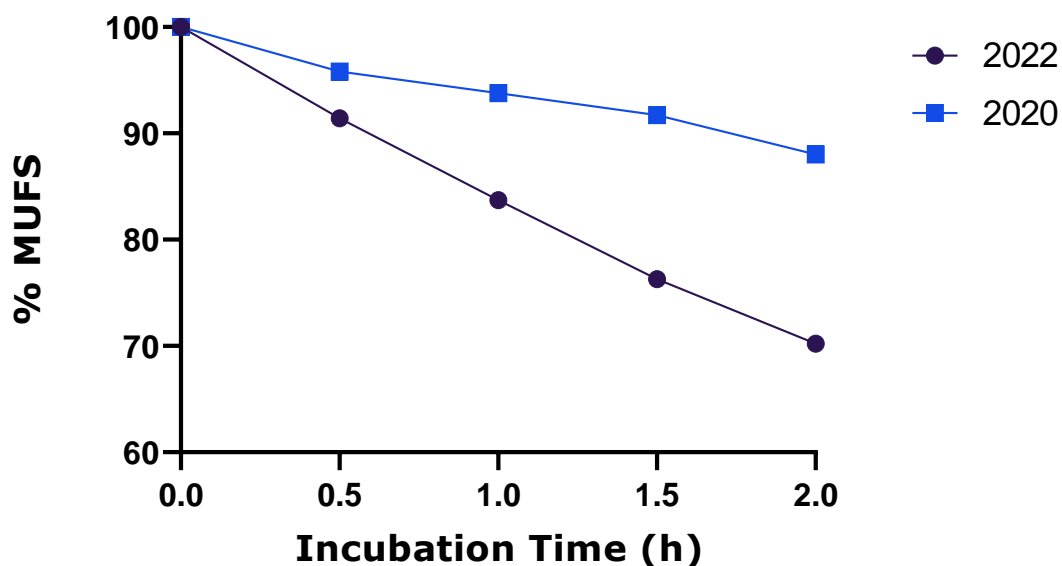


**Figure 32.** Assessment of ARSA activity through conversion of MUFS in 2020 vs. 2022.

### 2.2.2 AMC (3) standard curve

A standard curve of AMC 3 was generated to enable quantification of payload released in model linker metabolism assays. A twofold dilution series from 50  $\mu\text{M}$  to 3.125  $\mu\text{M}$  3 was analysed at 320 nm by a diode array detector, and fluorescence was monitored at 345 nm<sub>ex</sub> 445 nm<sub>em</sub>. Three replicate dilution series were conducted and plotted as the mean peak area. Buffer alone was used as a control for 0  $\mu\text{M}$ . Fluorescence saturated the detector beyond 12.5  $\mu\text{M}$  and was therefore only valid for small amounts of payload release and to confirm the identity of the AMC peak.

## Discussion

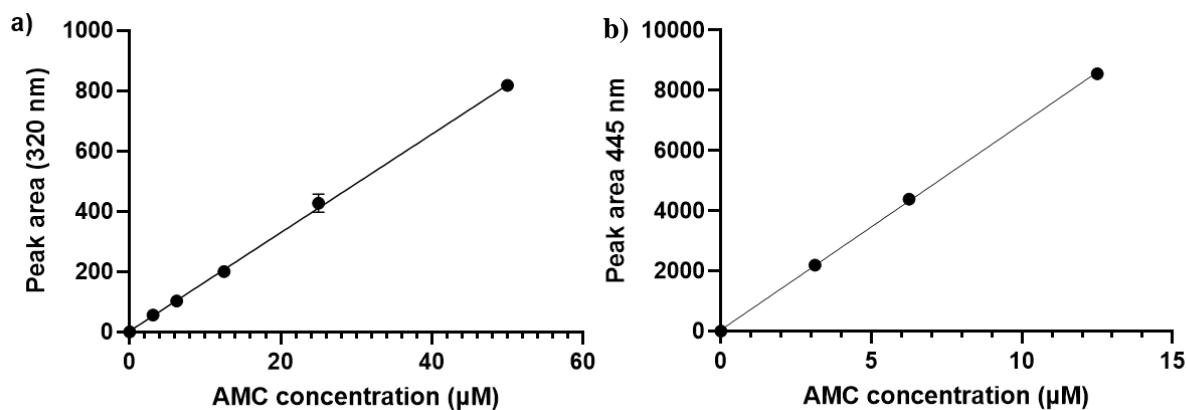


**Figure 33.** a) AMC standard curve at 320 nm for quantification of payload release.  $Y = 16.30 \times X + 4.272$ ,  $R^2 = 9.9987$ ,  $LOD = 3.58$ ,  $-0.04 \mu\text{M}$ ,  $LOQ = 10.86$ ,  $0.4 \mu\text{M}$ . b) AMC fluorescence standard curve for quantification of payload release ( $345 \text{ nm}_{\text{ex}}$ ,  $445 \text{ nm}_{\text{em}}$ ).  $Y = 685.1 \times X + 43.12$ ,  $LOD = 0.04 \mu\text{M}$ ,  $LOQ = 0.25 \mu\text{M}$ . Calculations made using GraphPad, points are mean of three replicates, error bars are the standard deviation and may be obscured by points.

### 2.2.3 Method development

The MUFS assay method was applied to analysis of the model linkers **1**. Three replicate assays were run at  $50 \mu\text{M} **1** and  $50 \mu\text{g/mL}$  ARSA sampling at 0, 2, 4, 6, 8, 12, and 24 hours incubation time, however, this method produced a high degree of variability. The loss of sulfate peak area did not reliably correspond to AMC release within experiments for a given substrate. Replicates from an assay using *ortho*-methoxy sulfate **1c** are illustrated in **Figure 34**. In replicate B hydrolysis of **1c** occurs almost twice as fast as in replicate C (34% loss vs. 66% loss respectively), however this is not reflected in the amount of AMC released achieving a very similar 45% ( $23 \mu\text{M}$ ) and 50% ( $25 \mu\text{M}$ ) release of AMC respectively. The starting peak areas of all assays were completely consistent.$



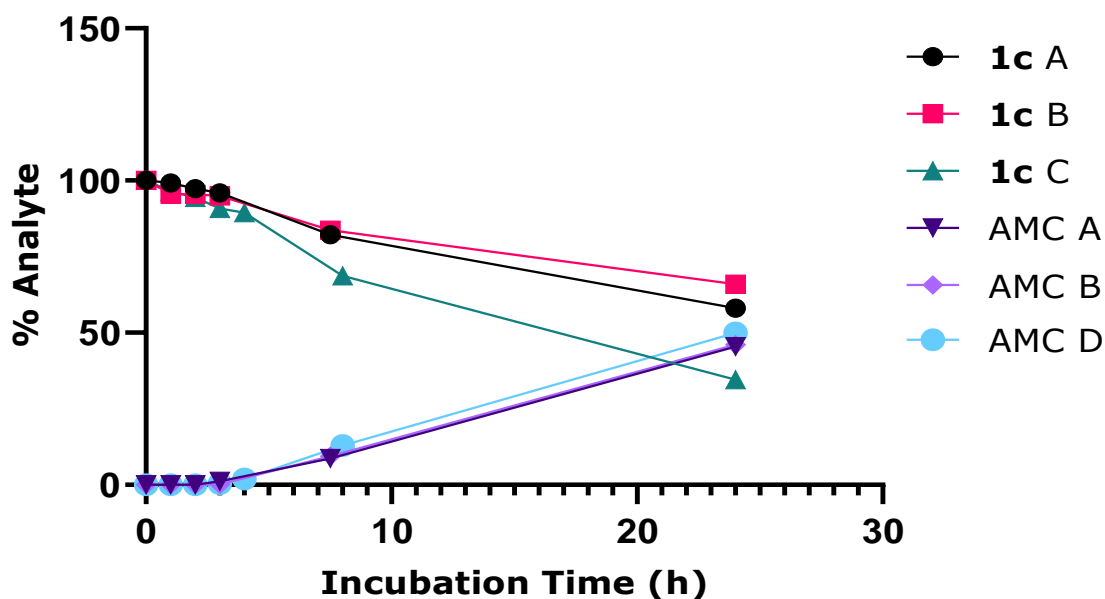


**Figure 34.** Change in % sulfate and % total AMC over time. Results from replicate **1c** assays at 50  $\mu\text{M}$ . Calculations made using graph pad. AMC released calculated AMC concentration from peak area against the standard curve and is plotted as a % of 50  $\mu\text{M}$ .

Further the peak areas for both sulfate and AMC would significantly fluctuate over time. This was typically observed as a gradual rise in sulfate peak area for no enzyme controls, although the sulfates appeared stable in the absence of enzyme by-product formation was not observed – even with extended chromatographic runs. Several strategies were explored to mitigate these issues. Firstly, assays were run with or without reaction vials caps to determine if particulate from the cap interfered with the injection, or if the buffer was evaporating, but no difference was observed. To determine if the issue lay in sulfate insolubility leading to increased dissolution over time assays were conducted at a reduced concentration (25  $\mu\text{M}$ ), along with warming of stock solutions to 37  $^{\circ}\text{C}$  before dilution to assay conditions. Finally, a separate HPLC was used to account for instrument error, however the issues persisted despite these changes.

New assay conditions were developed in an effort to avoid these issues. A higher ratio of enzyme to sulfate was used to increase the speed of reactions and reduce error introduced through the aging of solutions. The substrate concentration was reduced to 25  $\mu\text{M}$  to limit potential problems with solubility. The sampling interval was reduced to every 2 hours conducting three replicates and a MUFS control assay sequentially using a 30-minute run profile. This aimed to reduce the influence of passive factors such as ambient temperature

between assays. Finally, the total volumes were reduced to allow a single frozen aliquot of ARSA to be used across all four experiments with the MUFS assays acting as an external control for enzyme condition. Despite these changes, peak areas of both the sulfates and AMC continued to fluctuate (**Figure 35.**).

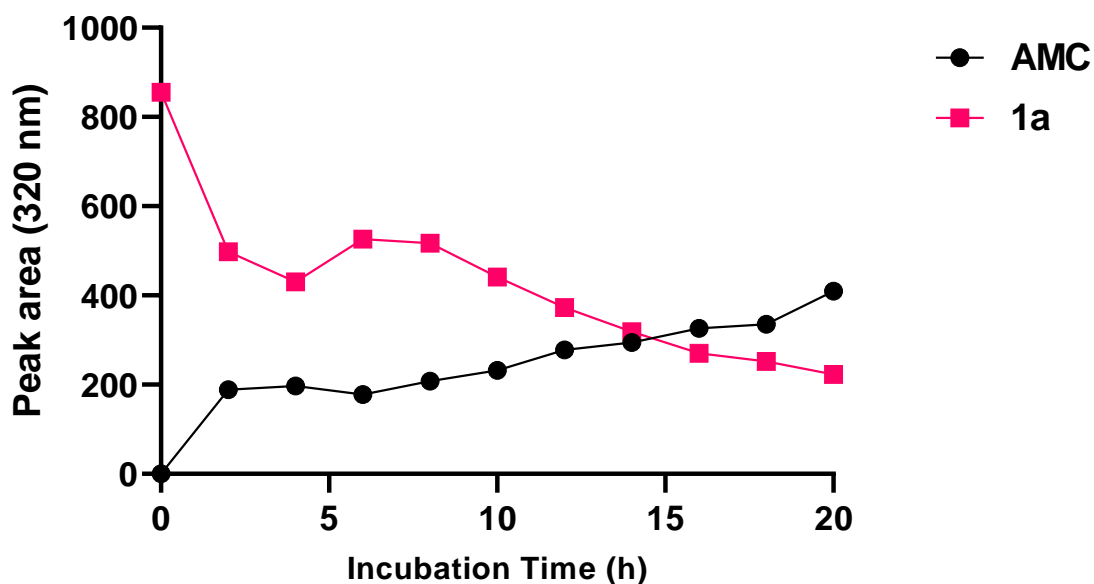


**Figure 35.** Inconsistent peak areas over time under new 25  $\mu\text{M}$  assay conditions with **1a** and **AMC**. 25  $\mu\text{M}$  **1a** was incubated with ARSA. Y-axis reports peak areas.

Assays were continued under these conditions as the number of sulfatase aliquots limited the scope of further investigation. The source of variability remained unclear, however, the assays still provided useable information although some quantitative analysis was not possible.

#### 2.2.4 Assessment of sulfate hydrolysis

Analysis of the data across assays enabled division of the substrates into two groups, *i*) substrates slower than the unsubstituted sulfate **1a** and *ii*) substrates faster than **1a** (**Figure 36.**).

Each assay was run in triplicate, and peak areas were converted to percentages of the no enzyme control peak area. The mean and standard deviation of each time point were calculated and graphed in **Figure 36.**, with error bars representing the standard deviation.

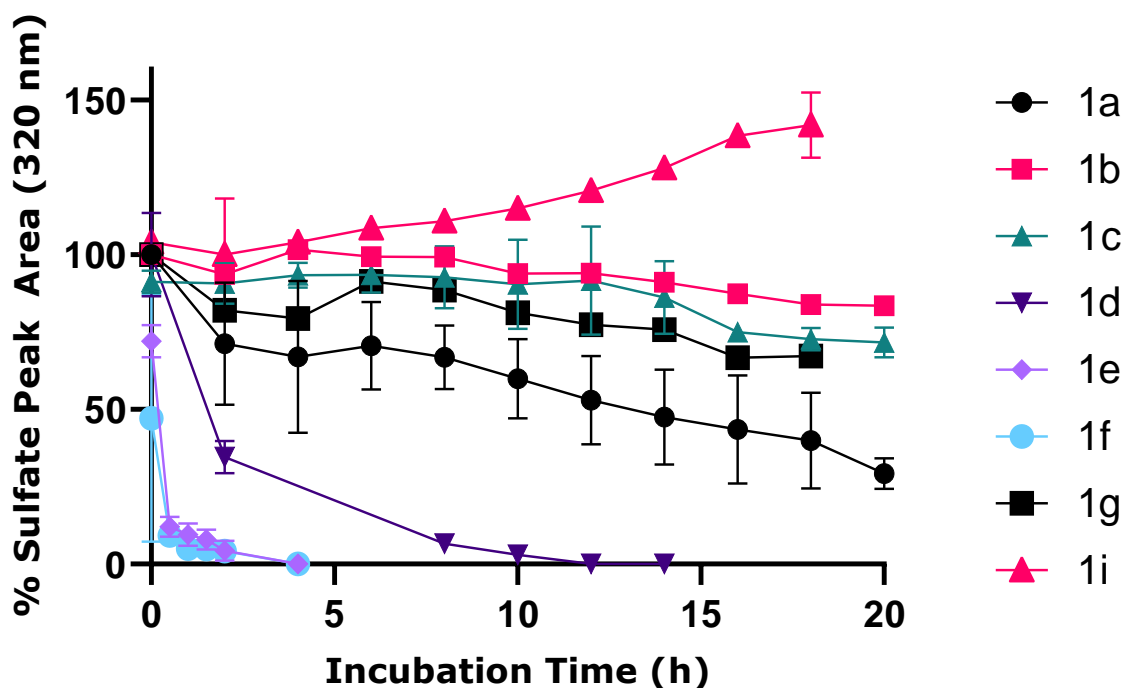
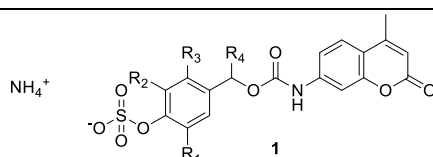


**Figure 36.** Normalised rate of sulfate **1a-g,i** hydrolysis with ARSA. **a.** all substrates. Calculations made using GraphPad, points are the mean of three replicates, error bars are the standard deviation and may be obscured by points. Comparisons made using the mean % sulfate peak area vs **1a** using a one-way ANOVA, P-values vs. **1a** calculated using Dunnett's test to compare means at each time point.

ARSA mediated hydrolysis of all substituted sulfates (**1b-f, i**) was significantly different to the unsubstituted parent **1a** (Error! Not a valid bookmark self-reference.).

**Table 8.** Anova analysis of sulfate hydrolysis of **1b-g,i** and **1a**.

Substrate	Group	Difference of means vs <b>1a</b> (P value)
<b>1b</b> ( $R_1 = \text{Me}, R_2 = R_3 = R_4 = \text{H}$ )	<i>i</i>	0.0020
<b>1c</b> ( $R_1 = \text{OMe}, R_2 = R_3 = R_4 = \text{H}$ )	<i>i</i>	0.0051
<b>1d</b> ( $R_1 = \text{F}, R_2 = R_3 = R_4 = \text{H}$ )	<i>ii</i>	0.0022
<b>1e</b> ( $R_1 = \text{NO}_2, R_2 = R_3 = R_4 = \text{H}$ )	<i>ii</i>	0.0002
<b>1f</b> ( $R_1 = R_2 = \text{F}, R_3 = R_4 = \text{H}$ )	<i>ii</i>	<0.0001
<b>1g</b> ( $R_1 = \text{CF}_3, R_2 = R_3 = R_4 = \text{H}$ )	<i>i</i>	0.0427
<b>1i</b> ( $R_2 = \text{OMe}, R_1 = R_3 = R_4 = \text{H}$ )	<i>i</i>	<0.0001



### 2.2.4.1 Group *i* substrates

Analysis of the group *i* substrates suffered from significant sampling error, limiting the scope of comparisons that can be made between the group. Group *i* substrates suffered from fluctuating peak areas increasing the standard deviation of the means and causing some samples to rise at various points (**Figure 37. 1g, 1b, 1i**). The peak area for *meta*-methoxy analogue **1i** rose 41% above the starting control area despite also reporting release of the **AMC** payload (**Figure 39**). Due to these issues comparisons cannot be made with **1i**. As **1i** was the only R<sub>3</sub> substituted analogues this limited this aspect of our SAR study. Despite the apparent error limited conclusions can still be drawn from this group. The electronic characteristics of the substrates appear to influence their rate of hydrolysis. The *ortho*-trifluoromethyl sulfate **1g** was hydrolysed significantly faster than the non-fluorinated methyl analogue **1b** ( $P = 0.0001$ ), suggesting that an electron withdrawing substituent promotes sulfate hydrolysis. The sulfates with electron donating substituents **1b**, **1c** and **1i** were the slowest three substrates. The reduction in activity from the unsubstituted **1a** to the *ortho*-substituted substrates **1b**, **1c**, and **1g** may result from steric hinderance. suggest that both steric and electronic factors influence substrate binding.

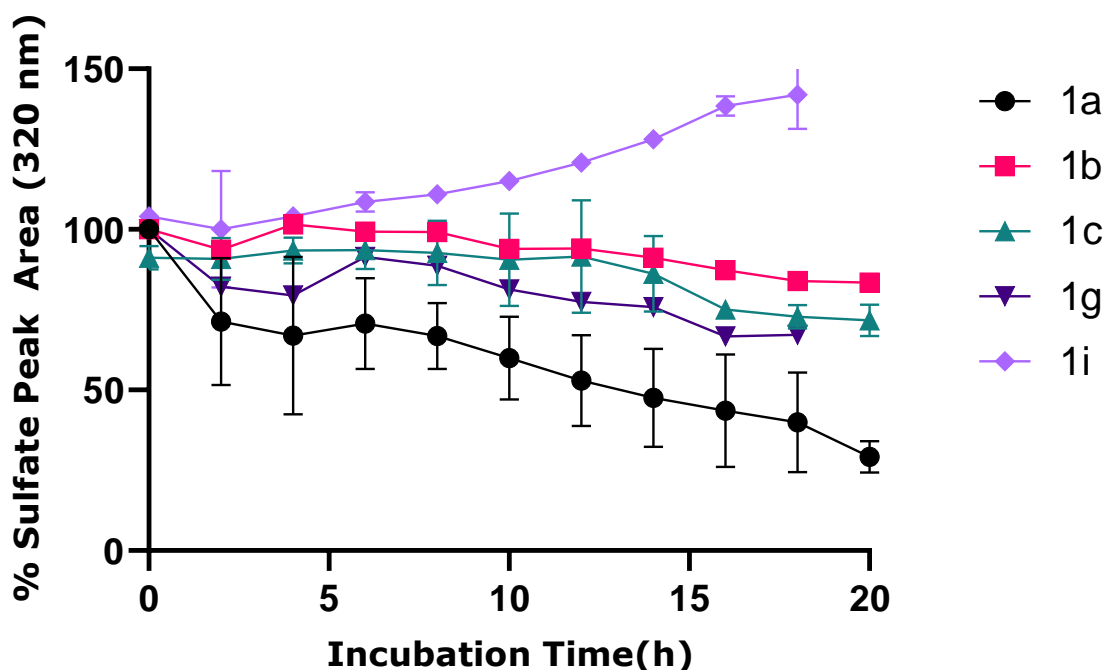


**Figure 37.** Normalised sulfate hydrolysis over time of group *i* substrates. Calculations carried out on GraphPad. Comparison of substrates made using paired t-tests.

### 2.2.4.2 Group *ii* substrates

Analysis of group *ii* substrates did not suffer from variable sulfate peak area (**Figure 38**). The sulfates were rapidly hydrolysed and each group *ii* substrate was consumed within 12 hours, indicating that the issues seen with group *i* substrates may be linked to the rate of hydrolysis, although we were unable to investigate this further.

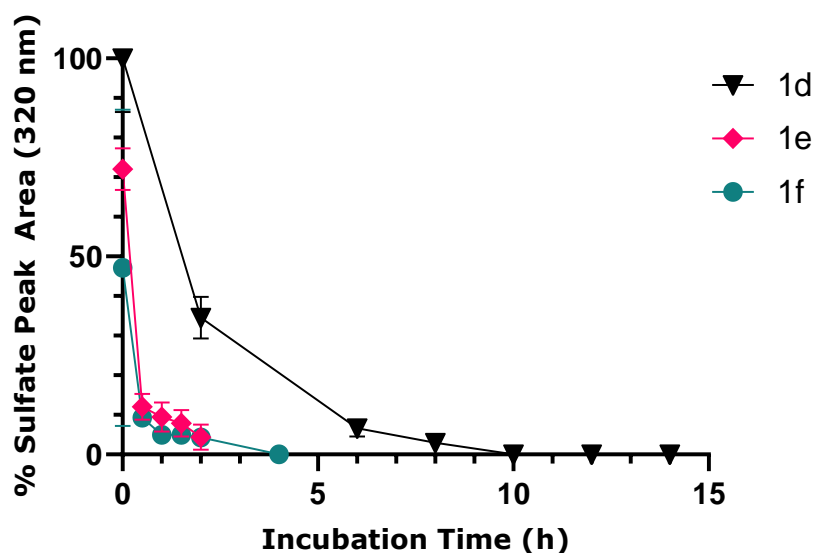


**Figure 38.** Normalised rate of sulfate hydrolysis of group *ii* substrates **1d-f**. Sulfates **1e** and **1f** were assayed with 30-minute time intervals due to their rapid rate of hydrolysis. Calculations were made using GraphPad, Comparison of % sulfate peak area over time were made using paired t-tests.

The *ortho*-difluoro sulfate **1f** and the *ortho*-nitro sulfate **1e** were hydrolysed faster than the *ortho*-fluoro sulfate **1d**. Only trace concentrations of sulfates **1e** and **1f** were present after 2 hours so follow up assays were conducted with 30-minute sampling intervals. Both **1e** and **1f** were rapidly hydrolysed with  $28\% \pm 5.2\%$ , and  $53\% \pm 40\%$  reduction in peak area respectively at the  $t=0$  sampling point, <2minutes after the enzyme was injected. The delay in sampling is unavoidable as it results from the time taken for the autosampler to mediate injection. No significant difference was found between the hydrolysis of **1e** and **1f**, with  $88\% \pm 3\%$  and  $91\% \pm 1\%$  reduction in peak area respectively after 30 minutes of incubation. A method with shorter sampling intervals would be required to determine if there is a difference in the rate of hydrolysis between these two substrates. The results from group *ii* support the conclusions from group *i*. All three group *ii* substrates include electron withdrawing substituents indicating that electron withdrawing substituents positively influence the rate of sulfate hydrolysis. Another contributor to the rate of hydrolysis of the fluorinated substrates **1d** and **1f** may be attributed to the limited steric influence of fluorine substituents as the halogen is a weak

## Discussion

electron withdrawing group. Inclusion of the second fluorine in **1f** appears to increase the rate of hydrolysis at the initial time point over its monosubstituted counterpart **1d**, however these points were not significantly different ( $P > 0.05$ ), although at the 30 minute time point the difference in hydrolysis is clear. Re-assay of **1d** using a shorter sampling interval would be necessary to make this comparison clear, however, this was not possible due to time constraints. The *ortho*-nitro substituted sulfate **1e** is significantly faster than **1d** ( $P = 0.0243$ ) despite including a sterically bulkier nitro group indicating that compromise between steric and electronic effects is accommodated. This may be due to the strongly electron withdrawing negative mesomeric effect of the nitro group. In contrast *ortho*-trifluoromethyl sulfate **1g** (group *i*) is also strongly electron withdrawing however lacks a mesomeric effect.

### 2.2.4.3 Sulfate hydrolysis structure activity relationship

Previous literature SAR of garden snail and bacterial arylsulfatases and SAR of ARSC inhibitors found the  $pK_a$  of the phenol leaving group is an important factor determining a rate of sulfate hydrolysis (139,143,166,167,169). Decreasing the  $pK_a$  makes the phenol a better leaving group, resulting in an increased rate of sulfate hydrolysis. This work did find a relationship between calculated  $pK_a$  of the relevant phenol and the rate of sulfate hydrolysis (**Table 9**). Indeed, the increased activity of substrates with electron-withdrawing groups can be attributed to reduction of the  $pK_a$  through stabilisation of the conjugate base, which exists as a phenolate at pH 4.5. From this perspective the rapid hydrolysis of *ortho*-nitro sulfate **1e** results from a negative mesomeric effect as the nitro group is able to form resonance structures, stabilising the phenolate. We propose that this increased rate of reaction may compensate for any steric effect that could compromise access to the enzyme active site. The *ortho*-nitro sulfate **1e** has the lowest calculated  $pK_a$  of the substrates explored (**Table 9**).

**Table 9.** Sulfate hydrolysis analysis including the calculated pKa, % sulfate loss at 2 hours and group designation.

Substrate	phenol <i>pKa</i>	% Sulfate Loss at 2 h	Group
<b>1a</b> (R <sub>1</sub> = R <sub>2</sub> = R <sub>3</sub> = R <sub>4</sub> = H)	9.401	28.7	-
<b>1b</b> (R <sub>1</sub> = Me, R <sub>2</sub> = R <sub>3</sub> = R <sub>4</sub> = H)	9.637	6.3	<i>i</i>
<b>1c</b> (R <sub>1</sub> = OMe, R <sub>2</sub> = R <sub>3</sub> = R <sub>4</sub> = H)	9.053	9.3	<i>i</i>
<b>1d</b> (R <sub>1</sub> = F, R <sub>2</sub> = R <sub>3</sub> = R <sub>4</sub> = H)	8.102	65.5	<i>ii</i>
<b>1e</b> (R <sub>1</sub> = NO <sub>2</sub> , R <sub>2</sub> = R <sub>3</sub> = R <sub>4</sub> = H)	5.596	95.6	<i>ii</i>
<b>1f</b> (R <sub>1</sub> = R <sub>2</sub> = F, R <sub>3</sub> = R <sub>4</sub> = H)	6.799	95.7	<i>ii</i>
<b>1g</b> (R <sub>1</sub> = CF <sub>3</sub> , R <sub>2</sub> = R <sub>3</sub> = R <sub>4</sub> = H)	7.627	19.9	<i>i</i>
<b>1i</b> (R <sub>2</sub> = OMe, R <sub>1</sub> = R <sub>3</sub> = R <sub>4</sub> = H)	9.236	0	<i>i</i>

Sulfate hydrolysis is not determined by *pKa* alone. The inclusion of an electron withdrawing ortho-trifluoromethyl substituent on **1g** reduced the rate of sulfate hydrolysis relative to the unsubstituted sulfate **1a** despite **1g** having the third lowest calculated *pKa* of the series. This reduction in activity from **1a** to **1g** could be due to steric hindrance limiting the number of orientations the substrates can access ARSA's narrow active site, thereby introducing an entropic barrier. A SAR investigation of garden snail arylsulfatase activity found a trend favouring bi- and tri-cyclic compounds, presumably due to increased hydrophobic binding opportunities on the cells surface (143). These snail sulfatases are notoriously promiscuous and likely do not accurately model the more selective human sulfatases (187). The dramatic increase in hydrolysis of the *ortho*-difluoro sulfate **1f** is consistent with the increased activity illustrated by DiFMUFS (164). Fluorine may be the ideal substituent for ARSA substrates due to their electron withdrawing effect and minimal steric bulk.

### 2.2.5 Assessment of payload release

Payload release was monitored at  $\lambda_{ab}$  320 nm, and concentrations of **AMC** were calculated against the standard curve **Figure 33**. Across these assays the calculated concentrations of **AMC** did not directly correspond to the expected maximum (25  $\mu$ M) derived from the amount of sulfate included in each assay. All three group *ii* substrates were completely hydrolysed and appeared to release more than 25  $\mu$ M of **AMC**. In the *ortho*-nitro sulfate **1d** assay the concentration of **AMC** continued rising hours after all of the sulfate and the intermediate phenol had been consumed eventually reaching 37  $\mu$ M at t = 18 hours (**Figure 39**). We

anticipate that the theoretical achievable concentration of AMC should be lower than 25  $\mu\text{M}$  due to reaction of AMC with the by-product **23** forming minor amounts of **25**, an effect noted during preliminary investigations supporting this project (**Scheme 14**).

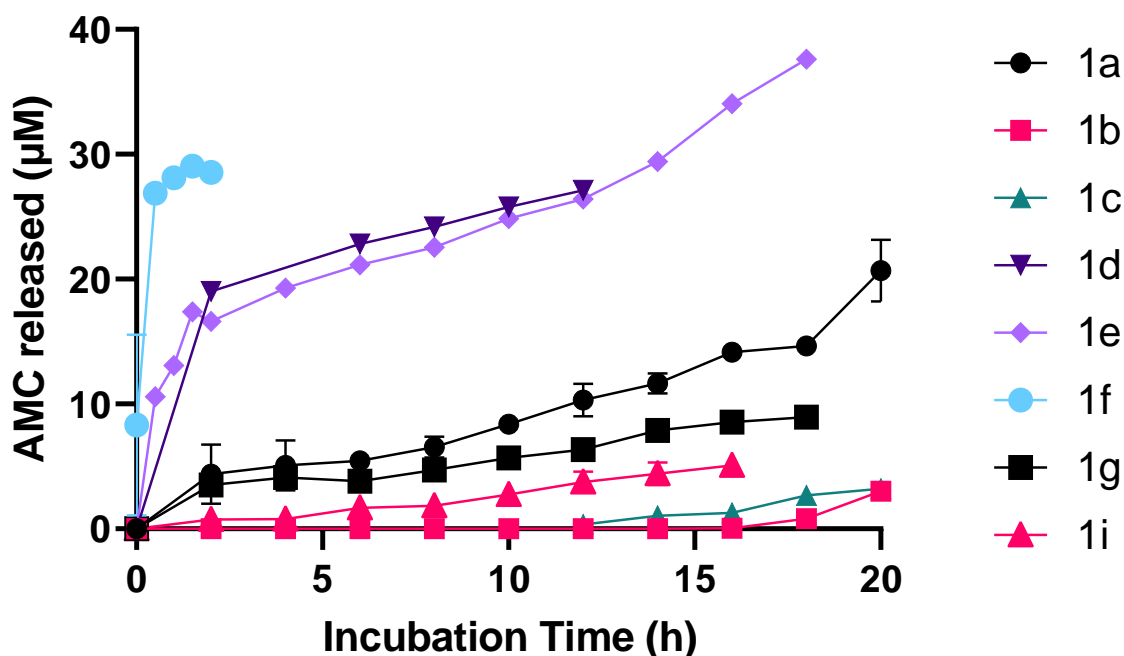
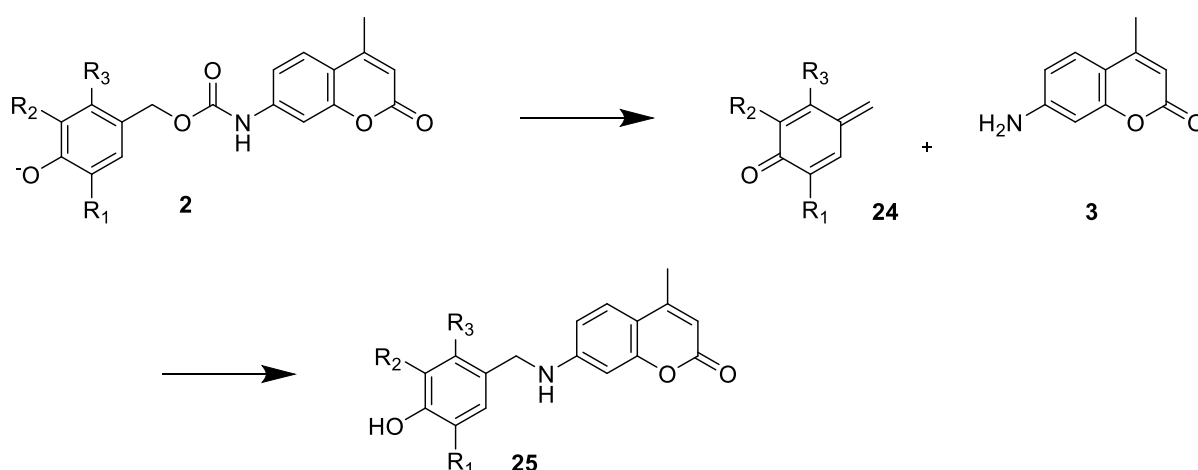


**Figure 39.** Normalised rate of AMC (**3**) release. Calculations made using GraphPad, concentrations derived from the AMC standard curve. Comparisons made using paired t-tests.



**Scheme 14.** Minor reaction of AMC and **2** forming **25**.

Despite this issue, conclusions can still be drawn from this work. The rate of hydrolysis of all group *i* substrates was sufficiently slow that the phenol intermediate did not reach the limit of detection before fragmentation occurred. Therefore, we infer that the rate of payload release from group *i* linkers is limited by the rate of sulfate hydrolysis. Hydrolysis of all three group *ii*



## Discussion

substrates was sufficiently rapid that we could detect accumulation of their phenol intermediates and therefore able to compare their rates of fragmentation. Due to the inherent instability of these intermediate species authentic standards cannot be prepared and a standard curve could not be used to quantify the concentrations of each phenol. With the fluorinated analogues **1d** and **1f** very little **2d** and **2f** was detected (**1f**, **Figure 40**). In fact, the rate of payload release is roughly equal to the rate of sulfate hydrolysis and  $>25 \mu\text{M}$  AMC is released before their respective sulfates have been consumed. Therefore, we infer like the group *i* substrates, the rate of payload release of **1d** and **1f** is limited by the rates of sulfate hydrolysis. The intermediate fragmentation to release the payload is less facile for the nitro analogue **1e** where intermediate accumulation was more pronounced (**Figure 41**).

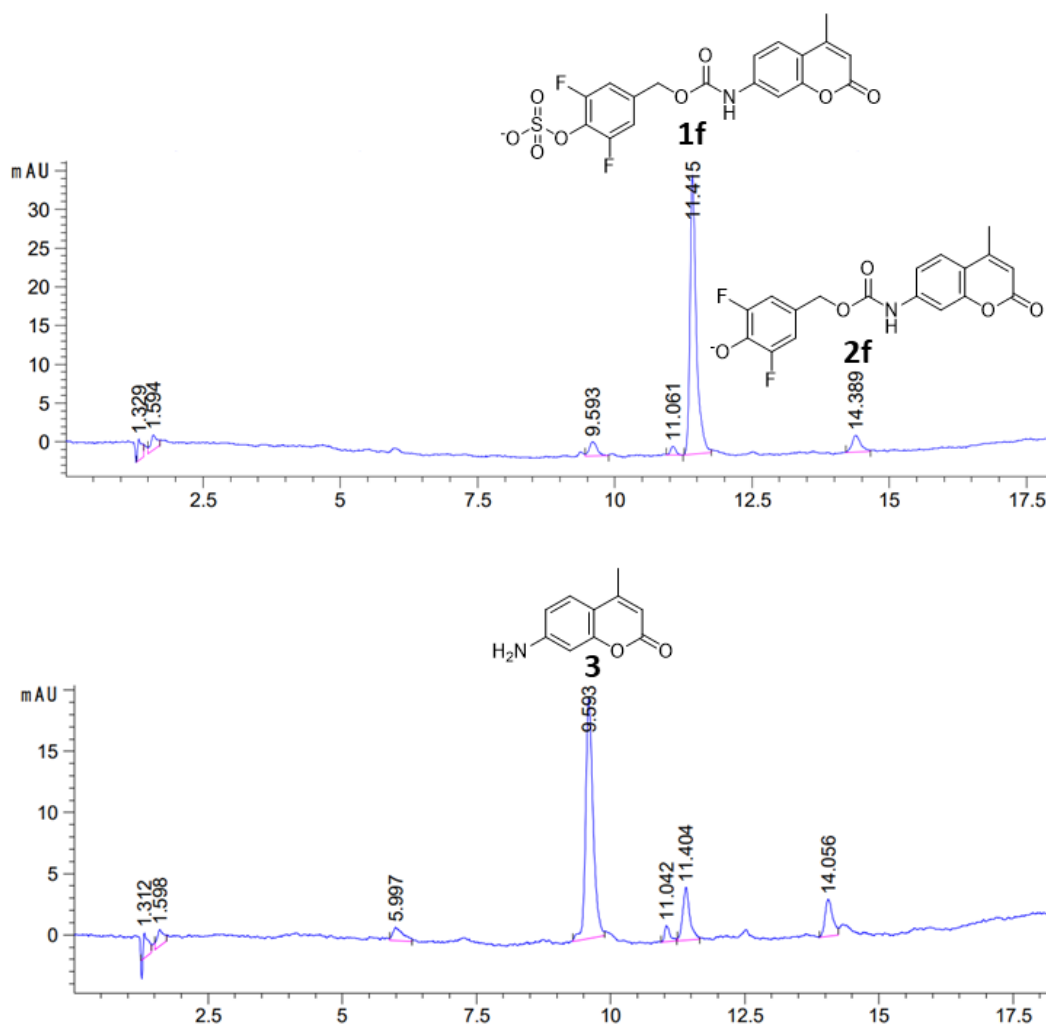


**Figure 40.** HPLC diode array data of **1f** assay, absorbance 320 nm, t = 0, t = 30 mins.

Regardless of having similar rates of sulfate hydrolysis, the **1e** had a significantly slower rate of AMC release ( $P = 0.0008$ ). In fact, phenol **2e** was still present after 10 hours, 8 hours after **1e**

## Discussion

had been completely consumed. Therefore, we infer that unlike all the other substrates the rate of payload release of **1e** is limited by the rate of fragmentation of its intermediate. We attribute the differences in rate of fragmentation to the substituents mesomeric effects. Fluorine is a resonance donor, increasing the electron density around the phenolate and destabilising the intermediate, causing rapid fragmentation (188). Conversely, nitro groups are resonance acceptors, stabilising the phenolate by withdrawing electrons and distributing the anionic charge across the ring and nitro group. This is illustrated by the *pKa* difference of **1d-f** (Table 9), with **1d** having the lowest calculated *pKa* of 5.59. Importantly the **1e** achieves a significantly faster rate of sulfate hydrolysis than the unsubstituted sulfate **1a** ( $P = 0.0125$ ), despite the stabilisation of the intermediate. However, the rates of payload release of **1d** and **1e** are indistinguishable despite **1e** being hydrolysed significantly faster than **1d** ( $P = 0.0243$ ). Thus, we can see the two-step sulfate hydrolysis, fragmentation linker-activation process is influenced by factors that must be balanced creating a complex SAR picture.

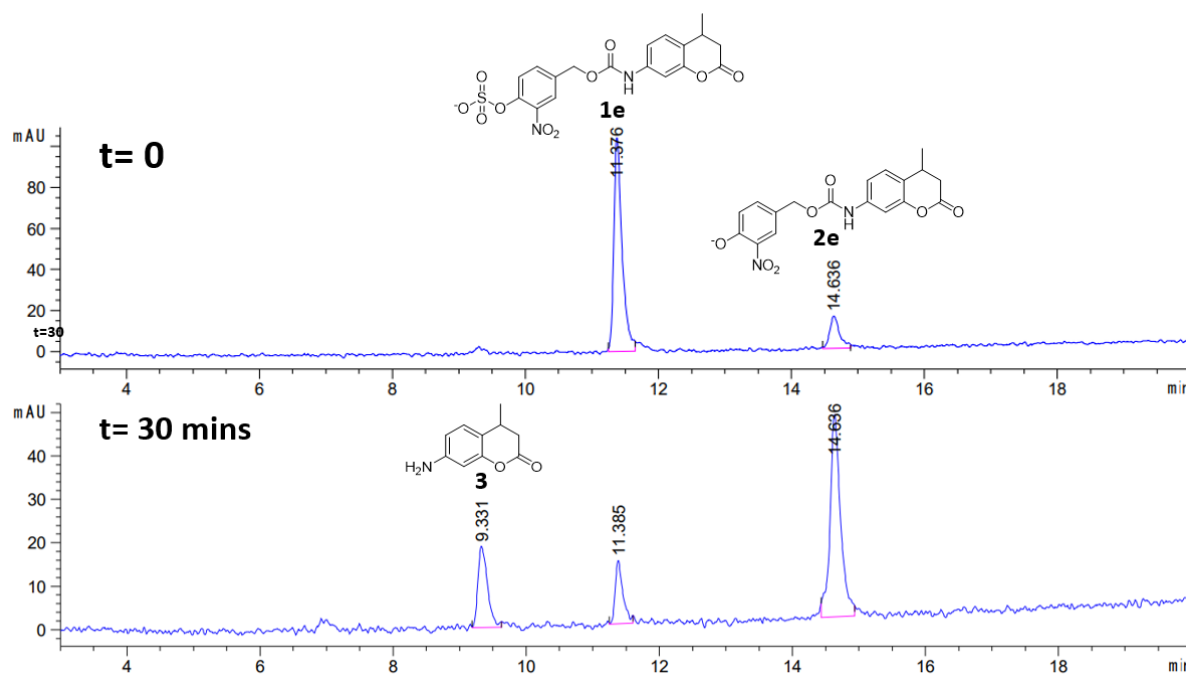


**Figure 41.** HPLC diode array data of **1e** assay, absorbance 320 nm.  $t=0$ ,  $t=30$  mins.

### 2.2.6 Application as ADC linkers

The most promising motifs identified from this library were the *ortho*-difluoro **1f** and *ortho*-nitro **1e** which reported the fastest rates of sulfate hydrolysis against ARSA. Interestingly the rate of payload release was significantly different between these model linkers due to stabilisation of intermediate **2**. Importantly the rate of payload release from **1e** was still faster

than the unsubstituted **1a** supporting the hypothesis the improved efficacy of the nitro analogue (**Figure 39**, **Figure 27d**) over its unsubstituted counterparts is due to an increased rate of payload release (138). Therefore, when applied to ADCs *ortho*-difluoro linkers have the potential to increase efficacy further due to their increased rate of payload release over their nitro-substituted counterparts.

The *ortho*-difluoro linkers may be the ‘Goldilocks’ structure for ARSA specific cleavable linkers due to the unique steric and electronic characteristics of fluorine. Fluorine induces a strong inductive withdrawing effect, and a weaker resonance donating effect. When *ortho* to the sulfate fluorine increases the rate of sulfate hydrolysis through electron withdrawal without adding steric bulk, while then donating electrons to the resulting phenol intermediate through resonance to increase the rate of fragmentation. However, investigation into the effect these properties have on ADCs will be required to determine the optimal characteristics when applied to the multifaceted role of ADC linkers. However, it is unclear if rapid fragmentation itself is desirable, instead the fast sulfate hydrolysis and slow fragmentation as seen with the nitro analogue may be ideal. Indeed, investigation of the effect these properties have when applied to ADCs will be required to elucidate the optimal balance for ADC linkers and potentially allow for the rate of fragmentation to be altered for application to different ADCs.

### 2.3 Limitations and Future work

The chemical synthesis of these linkers progressed with consistently lower yields than reported literature. Only eight of the twelve substrates afforded their final sulfate monoesters. Conducting reactions at larger scale may have facilitated successful synthesis of more substrates that were abandoned as there was not sufficient compound to complete the final steps. The key difficulties were experienced following conjugation of the **AMC** payload and presence of the methylcarbamate **22** impurity. Efforts to identify the source of the impurity **22** were unsuccessful and the problem persisted through synthesis. The problems encountered during assay analysis were also related to the **AMC** payload and its fluorescence was not required to quantify payload release. Therefore, future work could employ a non-coumarin payload potentially avoiding these issues.

The small sample size of substrates ( $n = 8$ ), and sampling error from the HPLC (discussion in **Sections 2.2.3, 2.2.5**) limited the conclusions that can be drawn on ARSA’s aryl substrate SAR. Future work should expand the substrate library to include substrates with  $R_3$  and  $R_4$

## Discussion

substituents as these were not explored in this work. Interrogation of the properties of the lone R<sub>3</sub> substituted linker **1i** suffered from significant sampling error and no sound conclusions could be drawn from its assay results. The sampling interval was too long to compare the rate of hydrolysis of **1e** and **1f**. Follow up assays could reduce the sampling interval by quenching samples with MeOH at the desired time points prior to analysis.

Future work should investigate the best substrates (group *i*) with lysosomal extracts to better reflect the physiological picture. Linker **1f** should be applied to synthesis of ADCs and efficacy compared to dipeptide linkers and the previous nitro-containing arylsulfatase-cleavable linker from Bargh *et al.* under the same conditions to investigate the influence of fragmentation rate (30). Further work could aim to develop explore the effects of these linkers of drug-linker hydrophobicity, including the feasibility of developing ADCs with increased DAR.

## 2.4 Conclusions

This work synthesised a small library of eight *para*-sulfooxybenzyl carbamate linkers **1a-g,i** and assessed their suitability as both ARSA substrates and cleavable linkers for application to ADCs. This thesis found low steric impact and electron withdrawal as beneficial properties for arylsulfate substrates of ARSA. Further, this work described ARSAs strong preference substrates with mesomeric electron withdrawal, as strong inductive withdrawal was unable to overcome the steric effect. Further development of this library is required to investigate this effect further. This work identifies the ortho-difluoro (**1f**) and ortho-nitro (**1e**) sulfate linkers as the most promising sulfate substrates for development of ARSA-cleavable linkers. The electronic characteristics of the substrate must also be considered for application to ADC linkers. The resonance effect of the nitro substituent significantly reduced the rate payload release by stabilising the immolative phenol intermediate. Future development of these arylsulfatase cleavable linkers is required to determine the optimal combination of these properties as applied to ADCs.

# Chapter 3: Experimental

### 3. Experimental

#### 3.1 General details

All reactions were carried out using freshly distilled laboratory grade solvents unless otherwise specified. Dry THF and toluene were purchased from Acros Organics pre-dried and stored over a molecular sieve. Organic solutions were dried over  $\text{MgSO}_4$  and solvents evaporated under reduced pressure on a rotary evaporator. Room temperature (rt) refers to the ambient room temperature. Thin-layer chromatography (TLC) was carried out on an aluminium-backed silica gel plates (Merck 60 F254) with visualization of components by UV light (254, 366 nm). Column chromatography was carried out on Merck 230-400 mesh silica gel, using pre-distilled laboratory grade solvents. DCM refers to dichloromethane, DMF refers to dimethylformamide, EtOAc refers to ethyl acetate, MeOH refers to methanol. X4 refers to petroleum ether, boiling fraction 40 – 60 °C, Et<sub>2</sub>O refers to diethyl ether, Et<sub>3</sub>N refers to triethylamine, DBU refers to 1,8-diazabicyclo[5.4.0]undec-7-ene. Tris buffer refers to trisamineomethane. Eq. refers to molar equivalents. Recombinant human arylsulfatase A (ARSA) was provided by Dr James Dickson from the University of Auckland. ARSA was expressed as a secreted protein on HEK293 cells, purified by IMAC, dialysed and concentrated to afford a 1.61 mg/mL stock (based on A280 nm) in 25 mM Tris buffer (pH 7.5) containing 150 mM NaCl. The stock solution of ARSA was separated into 30  $\mu\text{L}$  aliquot and stored at -4 °C from its arrival in November 2019. Calculations were performed using GraphPad.

#### 3.2 Characterisation

Purity of all final compounds was analysed by reverse-phase HPLC (LUNA-C18 column. 5 $\mu$ , 3.0 X 150mm) using an Agilent Technologies 1260 Infinity equipped with a diode-array detector by Mr Sisira Kumara. Gradients of 80% acetonitrile/20% H<sub>2</sub>O (v/v) in 45 mM buffer, pH 3.5 and 1.0 mL/min were used as the mobile phase. Peak areas were monitored at 330  $\pm$  50nm and were >95% relative to other components. Melting points were obtained on an electrothermal 2300 Melting Point Apparatus by Mr Wilson Sun. NMR spectra were obtained on a Bruker Avance 400 spectrometer at 400 MHz for <sup>1</sup>H and 100 MHz for <sup>13</sup>C spectra using appropriate deuterated solvents. Chemical shifts and coupling constants were recorded in units of ppm (2 d.p. <sup>1</sup>H NMR, 1 d.p. <sup>13</sup>C NMR) and Hz (1 d.p.). Shifts are referenced to the residual non-deuterated solvent peak ( $\text{CDCl}_3$ : 7.26,  $\text{DMSO-}d_6$ : 2.50,  $\text{CD}_3\text{OD}$ : 3.31,  $\text{D}_2\text{O}$ : 4.79 ppm). <sup>13</sup>C NMR experiments conducted as attached proton tests (APT). Assignments supported by

## Experimental

$^1\text{H}$ - $^{13}\text{C}$  HMBC and  $^1\text{H}$ - $^{13}\text{C}$  HSQC spectra or analogy to related analogues unless otherwise stated. Low resolution mass spectra (LRMS) were gathered by direct injection of methanolic solutions into a Agilent 6120 mass spectrometer using atmospheric pressure chemical ionization (APCI) mode with a fragmentor voltage of 50 V and a drying gas temperature of 250 °C. High resolution mass spectra (HRMS) were measured by Mr Sree Bhavan on an Agilent Technologies 6530 Accurate-Mass Quadrupole Time of Flight (Q-TOF) LC/MS interfaced with an Agilent Jet Stream Electrospray Ionization source allowing positive or negative ion detection. Data reported as; chemical shift, multiplicity (s, singlet; d, doublet; t, triplet; m, multiplet; or a combination of thereof. Assignment, mass (observed, expected). The numbering systems do not necessarily follow the IUPAC convention to make clarity easier when assigning  $^1\text{H}$  NMR and  $^{13}\text{C}$  NMR peaks.. Assignments  $n_c$  refer to coumarin peaks as labelled. NMR spectra were processed using TopSpin (Bruker ®).

### 3.2.1 Safety risks

Extreme care was taken when conducting reactions with methyl triflate and triphosgene. All handling was conducted in a fume hood while wearing person protective equipment (Lab coat, glasses, nitrile gloves) and notices placed on the front of the fume hood during operation. Increased fume hood airflow was used when handling triphosgene and when purging the respective reactions of phosgene. Triphosgene was weighed inside a pre-weighed sealed tube.

### 3.3 Assay procedures

Assays were analysed by repeat sampling on a reverse-phase HPLC (L7-C18 column. 5 $\mu$ , 3.0 X 150mm) using an Agilent Technologies 1260 Infinity equipped with a diode-array detector and fluorescence detector. Gradients of 80% acetonitrile/20% H<sub>2</sub>O (v/v) in 45 mM ammonium formate buffer, pH 4.5 and 0.4 mL/min were used as the mobile phase. Peak areas were monitored at 320  $\pm$  50nm and fluorescence  $\lambda_{\text{ex}} = 375$  nm,  $\lambda_{\text{em}} = 475$  nm. The substrates **1** were believed to be ammonium salts, and this mass was considered when preparing stock concentrations. Substrates were weighted on analytical scales and made to concentration in DMSO.

#### 3.3.1 Assay procedure A.

Substrates (3  $\mu\text{L}$ , 10 mM, DMSO) were added to 45 mM ammonium formate buffer (579  $\mu\text{L}$ , pH 4.5) and warmed to 30 °C and sampled to determine purity and peak area. ARSA (18.6  $\mu\text{L}$ ,

## Experimental

1.61 mg/mL, 30mM Tris buffer) was added to a vortexed substrate buffer solution and incubated at 37 °C. Assay was monitored by direct injection at 0-, 1-, 2-, 3-, 4-, 8-, and 24 hour time points. Assays were run in triplicates.

### 3.3.2 Assay procedure B.

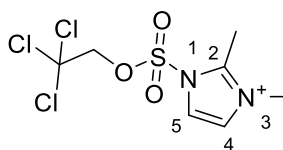
Substrates (25  $\mu$ L, 2 mM, DMSO) were added to 45 mM formate buffer (975  $\mu$ L, pH 4.5) and warmed to 37 °C and sampled to determine purity and peak area. ARSA (7.5  $\mu$ L, 1.61 mg/mL, 25 mM Tris buffer) was added to vortexed aliquot (243  $\mu$ L) of the substrate-buffer solution and incubated at 37 °C. The assay was monitored by direct injection with 2-hour intervals for 20 hours. Where indicated the sampling interval was reduced to 30-minutes. Assays were repeated 3 times with MUFS external control. Assays were carried out simultaneously. Calculations were performed using GraphPad. Comparisons between substrates is made using paired t-tests. Error bars represent the standard deviation, where no error bars are present the standard error is too small to be illustrated graphically.

### 3.3.3 Standard curve

**3** (2.5  $\mu$ L, 5 mmol in DMSO) was added to formate buffer (45 mM ,pH 4.5) at 37 °C and vortexed. Final volume (250  $\mu$ L, 50  $\mu$ M **AMC**) vortexed and a conducted a two-fold dilution series to 3.125  $\mu$ M. The dilution series was conducted in triplicate. Buffer alone was used for 0  $\mu$ M controls. HPLC Analysis was conducted as above. Standard curves were fitted to a liner regression model, limit of detection (LOD) and limit of quantification (LOQ) were calculated using the formulas  $LOD = 3.3 * \left(\frac{\sigma}{a}\right)$  and  $LOQ = 10 * \left(\frac{\sigma}{a}\right)$  where  $\sigma$  = the standard deviation of the Y-intercept and a is the slope of the curve.

## 3.4 Synthesis

### 2,3-Dimethyl-1-((2,2,2-trichloroethoxy)sulfonyl)-1H-imidazol-3-ium (14)



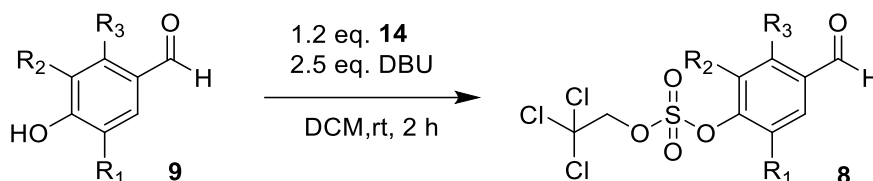
To 2,2,2-trichloroethyl 2-methyl-1H-imidazole-1-sulfonate **13** (2.0 g, 6.8 mmol) in cold (0 °C) Et<sub>2</sub>O (25 mL) was added dropwise methyl trifluoromethanesulfonate (7 mmol, 0.77 mL).



## Experimental

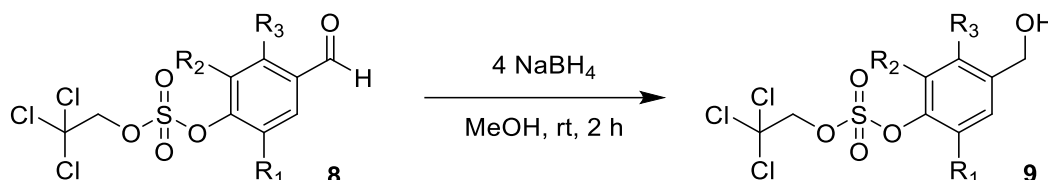
The mixture was stirred at 0 °C for 2 hours forming a white precipitate. Solids were filtered off and washed with cold Et<sub>2</sub>O and dried under vacuum to afford the title product **14**. The filtrate was cooled to -20 °C for 20 minutes and more precipitate was collected. Total yield 2.42 g, 90%. <sup>1</sup>H NMR consistent with reported data. <sup>1</sup>H NMR (CDCl<sub>3</sub>) δ<sub>H</sub> 2.97 (3H, s, H-2), 4.01 (3H, s, H-3), 5.19 (2H, s, CH<sub>2</sub>CCl<sub>3</sub>), 7.53 (1H, d, *J* = 4.33 Hz, H-4), 7.64 (1H, d, *J* = 2.17 Hz, H-5).

### General procedure A. Synthesis of benzaldehydes **8**



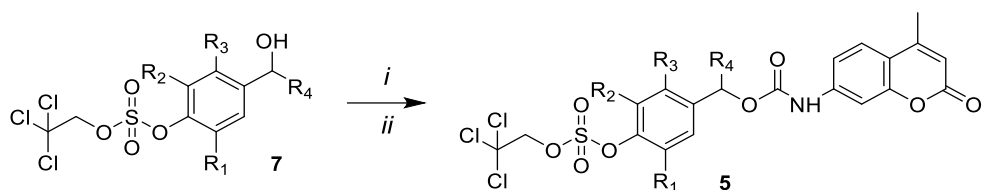
To a solution of hydroxybenzaldehyde **9** in DCM was added **14** (1.2 eq.) and DBU (2.5 eq.) and the mixture was stirred at room temperature for 2 h. The reaction mixture was diluted with H<sub>2</sub>O (25 mL), extracted with DCM (3 x 50 mL) and the extracts were dried over MgSO<sub>4</sub>. The solvent was removed *in vacuo* and the residue was purified by column chromatography to afford the title products. Purification details are given below.

### General procedure B. Synthesis of benzyl alcohols **7** by reduction of benzaldehydes **8**.



To a solution of benzyl alcohol **8** in MeOH was added NaBH<sub>4</sub> (4 eq.) and the mixture was stirred at room temperature for 2 h. The reaction was quenched with H<sub>2</sub>O, and aqueous NH<sub>4</sub>Cl was added dropwise until the solution reached a pH of 6. The mixture was extracted with DCM (3 x 50 mL), and the extracts were dried over MgSO<sub>4</sub> and concentrated *in vacuo*. Purification details are given below.

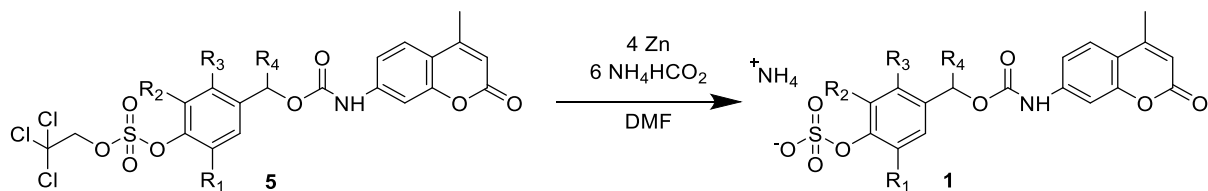
### General procedure C. Synthesis of carbamates **5**.



*i*) 3 eq. **3**, 0.8 eq. **19**, 3 eq.  $\text{Et}_3\text{N}$ , toluene, 117 °C,  $\text{N}_2$  (g). 2h. *ii*) **7**, dibutyltin diacetate (10 % eq.), THF, rt, >48 h.

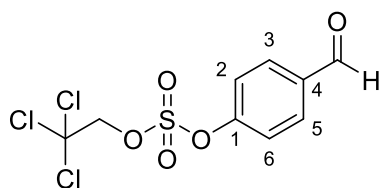
*i*) To a suspension of 7-amino-4-methyl coumarin **3** (1.2 eq.) in dry toluene added triphosgene **19** (0.8 eq.) and  $\text{Et}_3\text{N}$  (3 eq.) and stirred at 117 °C under  $\text{N}_2$  in a sealed tube for 2 h. Reaction cooled to room temperature and purged with  $\text{N}_2$  to remove excess phosgene. Additional care was taken handling triphosgene and bubbling with  $\text{N}_2$  due to the toxicity of phosgene gas. *ii*) Added benzyl alcohol **7**, and dibutyltin diacetate (10 mol%) in dry THF and stirred at room temperature under  $\text{N}_2$  for at least 48 hours in a sealed tube. Purification details are given below.

### General procedure D for sulfate deprotection



To a solution of **5** in DMF (4 mL) was added Zn dust (4 eq.) and ammonium formate (6 eq.) and the mixture stirred vigorously overnight at room temperature. The reaction was monitored by TLC and LRMS. Purification varied between analogues; details are given below.

### 4-Formylphenyl (2,2,2-trichloroethyl) sulfate (**8a**)

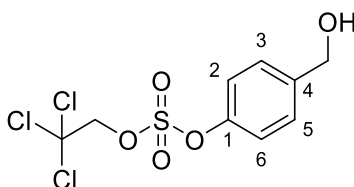


To 4-hydroxybenzaldehyde **9a** (0.10 g, 0.9 mmol) in DCM (8 mL) at 0 °C was added **14** (0.46 g, 1.0 mmol) and 1,2 dimethyl imidazole (0.18 g, 1.8 mmol). The mixture was stirred at room

## Experimental

temperature for 2 hours during which time the solution became pale yellow. The reaction was diluted with H<sub>2</sub>O (25 mL), extracted with DCM (3 x 50 mL) and the extract dried with MgSO<sub>4</sub>. The solvent was removed *in vacuo* and the crude product purified by column chromatography (10 – 20% EtOAc-X<sub>4</sub>) to afford **8a** as a white solid. (0.24 g, 82%). <sup>1</sup>H NMR (CDCl<sub>3</sub>) δ<sub>H</sub> 4.87 (2H, s, CH<sub>2</sub>CCl<sub>3</sub>), 7.54 (2H, ddd, *J* = 1.84, 2.5, 8.6 Hz, H-3,5), 7.99 (2H, ddd, *J* = 2.04, 2.5, 8.83 Hz, H-2,6), 10.04 (1H, s, CHO). <sup>13</sup>C NMR (CDCl<sub>3</sub>) δ<sub>C</sub> 80.8 (CH<sub>2</sub>CCl<sub>3</sub>, 1), 92.3 (CCl<sub>3</sub>, 2) 121.9 (2C, 3, 5), 131.9 (2C, 2,6), 135.6 (C 1), 154.1 (C 4) 190.4 (CHO). Molecular ion not observed by HRMS. LRMS *m/z* [M+H]<sup>+</sup> = 368, C<sub>9</sub>H<sub>7</sub>Cl<sub>3</sub>O<sub>5</sub>S required 333.58.

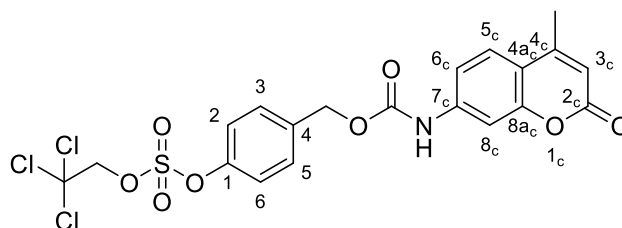
### 4-(Hydroxymethyl)phenyl (2,2,2-trichloroethyl) sulfate (7a)



Following **general procedure B 8a** (0.15 g, 0.40 mmol) was reduced to yield **7a** as a colourless oil (0.08 g, 40%), identical by <sup>1</sup>H NMR to reported literature (179) and the material described below.

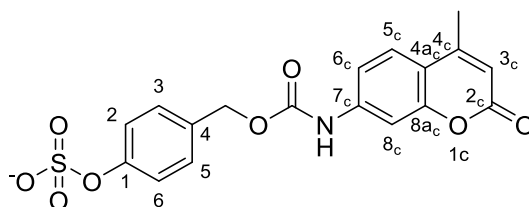
Following **general procedure A**, reaction of 4-hydroxybenzyl alcohol **17** (0.10 g, 0.80 mmol), was incomplete after 2 h. Additional **14** was added (0.27g, 0.70 eq.) and the mixture was stirred for a further 1 hours at room temperature. Following workup **7a** was purified by flash column chromatography (20% EtOAc-X<sub>4</sub>) to afford a colourless oil (0.08 g, 30%). <sup>1</sup>H NMR (CDCl<sub>3</sub>) δ<sub>H</sub> 4.73 (2H, s, CH<sub>2</sub>OH) 4.83 (2H, s, CH<sub>2</sub>CCl<sub>3</sub>) 7.32 (2H, dt, *J* = 2.14, 2.71, 8.74 Hz, H-3,5) 7.44 (2H, dt, *J* = 2.07, 2.71, 8.83 Hz, H-2, 6), OH proton not observed. <sup>13</sup>C NMR (CDCl<sub>3</sub>) δ<sub>C</sub> 64.5 (CH<sub>2</sub>OH), 80.6 (CH<sub>2</sub>CCl<sub>3</sub>), 92.6 (CCl<sub>3</sub>) 121.4 (2C, (C-3, 5), 128.6 (C-2, 6), 140.9 (C 1), 149.5 (C 4). Molecular ion not observed by HRMS. LRMS *m/z* [M+H]<sup>+</sup> = 370, C<sub>9</sub>H<sub>8</sub>Cl<sub>3</sub>O<sub>5</sub>S required 335.58.

**4-(((4-Methyl-2-oxo-2H-chromen-7-yl)carbamoyl)oxy)methyl)phenyl (2,2,2-trichloroethyl) sulfate (5a)**



Following **general procedure C**, benzyl alcohol **7a** (0.11g, 0.33 mmol) reacted to yield carbamate **5a**. The reaction was stirred for 2 months and rested for a further 4 months in a sealed tube under N<sub>2</sub> at room temperature due to the August 2022 Covid19 outbreak and subsequent lockdowns. The attempts to purify the crude product by column chromatography (MeOH-DCM) was unsuccessful affording a mixture of **5a** and **22** (see discussion). The impurity was Trituration with MeOH allowed the insoluble impurity **22** (see discussion) to be filtered off and **5a** was isolated by evaporation of the filtrate to yield the title product (0.05g, 28%). <sup>1</sup>H NMR (d<sub>6</sub>-DMSO) δ<sub>H</sub> 2.38 (3H, s, 4<sub>c</sub>), 5.23 (2H, s, Ar-CH<sub>2</sub>OCN), 5.37 (2H, s, CH<sub>2</sub>CCl<sub>3</sub>), 6.24 (1H, s, H-3<sub>c</sub>), 7.41 (1H, dd, *J* = 2.07, 8.77 Hz, H-6<sub>c</sub>) 7.55 (3H, m, H-3, 5, 8<sub>c</sub>), 7.61 (2H, d, *J* = 8.83 Hz, Ar-H, 2,6), 7.70 (1H, d, *J* = 8.71 Hz, H-5<sub>c</sub>), 10.32 (1H, s, NH). <sup>13</sup>C NMR (d<sub>6</sub>-DMSO) δ<sub>C</sub> 17.9 (CH<sub>3</sub>- 4<sub>c</sub>), 65.2 (CH<sub>2</sub>- 1<sub>c</sub>), 80.0 (CH<sub>2</sub>OCON), 92.9 (CCl<sub>3</sub>), 104.4 (CH, 8<sub>c</sub>), 111.9 (CH, 3<sub>c</sub>), 114.2 (CH, 6<sub>c</sub>), 114.4 (C, 4<sub>ac</sub>), 121.6 (2CH, 3, 5), 126.0 (CH, 5<sub>c</sub>), 130.1 (2CH, 2, 6), 136.5 (C 4), 142.5 (C 7<sub>c</sub>) 149.1 (C 2), 153.0 (C 4<sub>c</sub>), 153.1 (C 8<sub>ac</sub>), 153.8 (C CH<sub>2</sub>OCON), 159.9 (C 2<sub>c</sub>). HRMS *m/z* [M+H]<sup>+</sup> = 535.9729, C<sub>20</sub>H<sub>16</sub>C<sub>13</sub>NO<sub>8</sub>S required 535.9729

**4-(((4-Methyl-2-oxo-2H-chromen-7-yl)carbamoyl)oxy)methyl)phenyl sulfate (1a)**

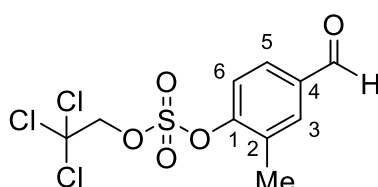


Following **general procedure D**, carbamate **5a** (0.04 g, 0.08 mmol) was deprotected to afford the title product **1a**. After 18 hours with standard conditions the reaction was incomplete and a further portion of Zn dust ( 0.02 g, 0.32 mmol) and ammonium formate (0.03 g, 0.48 mmol) and stirred over 66 h. The reaction mixture was concentrated *in vacuo* and the residue was suspended in MeOH. The insoluble fraction was filtered off and the soluble fraction was

## Experimental

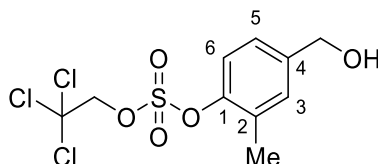
evaporated onto diatomaceous earth and purified by flash column chromatography (0-30% MeOH-EtOAc) to yield **1a** as a white solid (0.025g, 82%, HPLC purity = 99%).  $^1\text{H NMR}$  ( $\text{CD}_3\text{OD}$ )  $\delta_{\text{H}}$  2.44 (3H, d,  $J = 1.15$ , Ar- $\text{CH}_3$ , 4<sub>c</sub>), 5.18 (2H,  $\text{CH}_2\text{OCOR}$ ), 6.19 (1H, d,  $J = 1.13$  Hz, 3<sub>c</sub>), 7.31 (2H, dt,  $J = 2.11$ , 2.49, 8.68 Hz, H-3, 5), 7.55 (3H, m, H-2, 6, 5<sub>c</sub>), 7.62 (1H, d,  $J = 2.05$  Hz, H-8<sub>c</sub>) 7.67 (2H, d,  $J = 8.73$ , H-6<sub>c</sub>).  $^{13}\text{C NMR}$  ( $\text{CD}_3\text{OD}$ )  $\delta_{\text{C}}$  18.6 ( $\text{CH}_3$ , 4<sub>c</sub>), 67.6 ( $\text{CH}_2\text{OCON}$ ), 106.4 (CH, Ar-H, 8<sub>c</sub>), 113.0 (CH, 3<sub>c</sub>), 116.0 (CH, 6<sub>c</sub>), 116.3 (C 4<sub>ac</sub>), 122.6 (2C, H-3, 5), 126.9 (CH, 5<sub>c</sub>), 130.4 (2C, H-2, 6), 134.2 (C 4), 144.6 (C 7<sub>c</sub>), 154.1 (C 2), 155.3 (C 4<sub>e</sub>) 155.6 (C 8<sub>ac</sub>), 155.8 (C, OCON), 163.3 (C 2<sub>c</sub>). HRMS  $m/z$   $[\text{M}]^- = 404.0446$ ,  $\text{C}_{18}\text{H}_{14}\text{NO}_8\text{S}$  required 404.0446.

### 4-Formyl-2-methylphenyl (2,2,2-trichloroethyl) sulfate (**8b**)



Following **general procedure A**, 4-hydroxybenzaldehyde (0.10 g, 0.73 mmol) to afford **8b**. Following workup the crude residue was purified by flash column chromatography (20% EtOAc- $\text{X}_4$ ) to yield **8b** as a colourless oil (0.175 g, 72%)  $^1\text{H NMR}$  ( $\text{CDCl}_3$ )  $\delta_{\text{H}}$  3.99 (3H, s, H-2), 4.97 (2H, s,  $\text{CH}_2\text{CCl}_3$ ), 7.51 (1H, d,  $J = 1.82$  Hz, 3), 7.54 (1H, dd,  $J = 1.72$ , 6.99 Hz, 5), 7.60 (1H, d,  $J = 8.13$  Hz, 6), 9.98 (1H, CHO).  $^{13}\text{C NMR}$  ( $\text{CDCl}_3$ )  $\delta$  56.5 ( $\text{CH}_3$ , 2), 80.7 ( $\text{CH}_2\text{CCl}_3$ , 1), 92.5 ( $\text{CCl}_3$ ), 111.6 (CH 3), 123.9 (CH 5), 124.7 (CH 6), 136.6 (C 4), 143.1 (C 1), 152.0 (C 2), 190.2 (CHO). Molecular ion was not observed by HRMS. LRMS  $m/z$   $[\text{M}+\text{H}]^+ = 382$ ,  $\text{C}_{10}\text{H}_9\text{Cl}_3\text{O}_5\text{S}$  required 347.59.

### 4-(Hydroxymethyl)-2-methylphenyl (2,2,2-trichloroethyl) sulfate (**7b**)

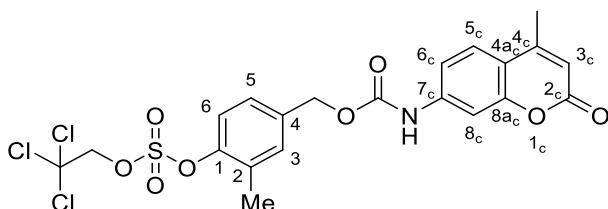


Following **general procedure B**, benzaldehyde **8b** (0.15 g, 0.44 mmol) was reduced to afforded benzyl alcohol **7b**. Following workup, the crude residue was purified by flash column chromatography (20% EtOAc- $\text{X}_4$ ) to yield **7b** as a colourless oil (0.11 g, 74%).  $^1\text{H NMR}$  ( $\text{CDCl}_3$ )  $\delta_{\text{H}}$  2.40 (3H, 2), 4.69 (2H,  $\text{CH}_2\text{OH}$ ), 4.83 (2H,  $\text{CH}_2\text{CCl}_3$ ), 7.24 (1H, dd,  $J = 1.69$ , 8.43

## Experimental

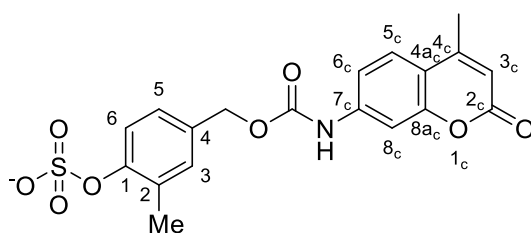
Hz, H-5), 7.30 (1H, d,  $J = 1.09$  Hz, H-3), 7.36 (1H, d,  $J = 8.37$  Hz, H-6). *OH* peak not observed. **LRMS**  $m/z$   $[M+H]^+ = 384$ ,  $C_{10}H_{11}Cl_3O_5S$  required 349.60

### 2-methyl-4-(((4-methyl-2-oxo-2*H*-chromen-7-yl)carbamoyl)oxy)methyl)phenyl (2,2,2-trichloroethyl) sulfate (**5b**)



Following **general procedure C**, benzyl alcohol **7b** (0.16 g, 0.42 mmol) stirred at room temperature under  $N_2$  for 92 h. The reaction was quenched with  $H_2O$  (5 mL) and concentrated *in vacuo*. The residue was suspended in EtOAc and evaporated onto silica for column chromatography (0.5 % MeOH in DCM). **5a** was purified from mixed fractions by trituration with MeOH collecting **5b** in the soluble fraction and concentrated *in vacuo* to yield the **5b** as a white solid (0.11 g 44%). **<sup>1</sup>H NMR** (DMSO)  $\delta_H$  2.35 (3H, s, 2), 2.38 (3H, d,  $J=1.06$  Hz, 4<sub>c</sub>), 5.19 (2H, s,  $CH_2OCON$ ), 5.39 (2H, s,  $CH_2CCl_3$ ), 6.24 (1H, d,  $J = 1.16$ , H-3<sub>c</sub>), 7.41 (2H, m, H-5, 6<sub>c</sub>), 7.49 (1H, s, H-5<sub>c</sub>) 7.50 (1H, d,  $J = 8.44$  Hz, H-6), 7.55 (1H, d,  $J = 2.01$  Hz, H-8<sub>c</sub>), 7.70 (1H, d,  $J = 8.71$  Hz, H-5''') 10.3 (1H, NH). **LRMS**  $m/z$   $[M+H]^+ = 550.9$ ,  $C_{21}H_{18}Cl_3NO_8S$  required 550.78.

### 2-methyl-4-(((4-methyl-2-oxo-2*H*-chromen-7-yl)carbamoyl)oxy)methyl)phenyl sulfate (**1b**)

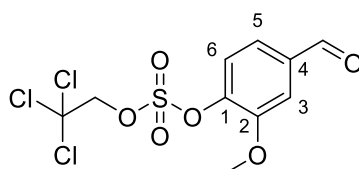


Following **general procedure D**, carbamate **5b** (0.04 g, 0.07 mmol) was reduced in 2 hours to afford **1b**. After 16 hours the reaction was concentrated *in vacuo* and the residue suspended in MeOH. The insoluble fraction was filtered off the filtrate was evaporated silica. **1b** was unable to be purified by flash chromatography (0 - 30% MeOH/ EtOAc). Attempts to purify by the mixed fractions by trituration with MeOH or acetone were unsuccessful. **1b** was purified by

## Experimental

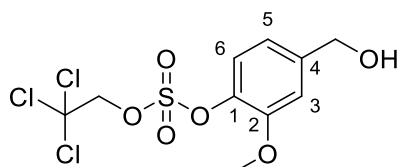
trituration in EtOAc filtering off the filtrate to collect **1b** as a white solid (0.01 g, 44%, **HPLC** purity = 98%). **<sup>1</sup>H NMR** (CD<sub>3</sub>OD)  $\delta_{\text{H}}$  2.34 (3H, s, 4<sub>c</sub>), 2.45 (3H, s, 2), 5.15 (2H, s, CH<sub>2</sub>OCON), 6.19 (1H, d,  $J = 1.43$ , H-3<sub>c</sub>), 7.22 (1H, dd,  $J = 2.18, 8.41$  Hz, H-5), 7.40 (1H, dd,  $J = 2.13, 8.73$  Hz, H-6<sub>c</sub>), 7.42 (1H, d,  $J = 8.19$  Hz, H-5<sub>c</sub>), 7.63 (1H, d,  $J = 2.05$ , H-3), 7.67 (1H, d,  $J = 8.74$ , H-6). **<sup>13</sup>C NMR** (d<sub>6</sub>-DMSO),  $\delta_{\text{C}}$  18.0 (CH<sub>3</sub>, 4<sub>c</sub>), 56.6 (CH<sub>3</sub>, 2), 66.2 (CH<sub>2</sub>), 104.4 (CH, 8<sub>c</sub>), 111.9 (CH, 3<sub>c</sub>), 114.3 (CH, 3), 114.3 (CH 6<sub>c</sub>), 114.4 (C 4<sub>ac</sub>), 120.2 (CH, 5), 122.3, 122.3 (CH, 6), 126.1 (CH, 5<sub>c</sub>), 130.1 (C 4), 132.2 (C 1), 142.8 (C 7<sub>c</sub>), 149.1 (C 2), 153.2 (C, 4<sub>c</sub>), 153.3 (C 8<sub>ac</sub>), 153.8 (C, OCON), 160.1 (C 2<sub>c</sub>). **HRMS**  $m/z$  [M]<sup>-</sup> = 418.0602, C<sub>19</sub>H<sub>16</sub>NO<sub>8</sub>S required 418.0602.

### 4-formyl-2-methoxyphenyl (2,2,2-trichloroethyl) sulfate (**8c**)



Following **general procedure A**, hydroxybenzaldehyde **9c** (0.290 g, 0.72 mmol) reacted to afford **8c**. Following workup, the crude residue was purified by column chromatography (20% EtOAc-X<sub>4</sub>) to yield **8c** as a yellow oil (0.300 g, 78%). **<sup>1</sup>H NMR** (CDCl<sub>3</sub>)  $\delta_{\text{H}}$  3.99 (3H, s, 2), 4.97 (2H, s, CH<sub>2</sub>CCl<sub>3</sub>), 7.51 (1H, d,  $J = 1.82$  Hz, H-3), 7.54 (1H, dd,  $J = 1.72, 6.99$  Hz, H-5), 7.60 (1H, d,  $J = 8.13$  Hz, 6), 9.98 (1H, CHO). Molecular ion not observed by **HRMS**. **LRMS**  $m/z$  [M+H]<sup>+</sup> = 398, C<sub>11</sub>H<sub>9</sub>Cl<sub>3</sub>O<sub>6</sub>S required 363.59.

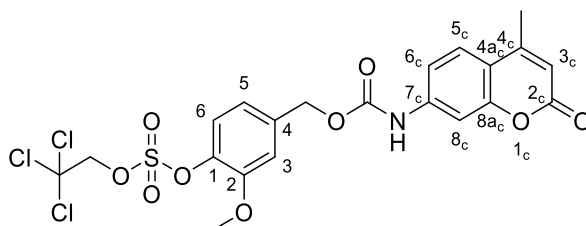
### 4-(hydroxymethyl)-2-methoxyphenyl (2,2,2-trichloroethyl) sulfate (**7c**)



Following **general procedure B**, benzaldehyde **8c** (0.290 g, 0.72 mmol) was reduced to yield **7c**. Following workup, the crude residue was purified by column chromatography (30% EtOAc-X<sub>4</sub>) to yield **7c** as a colourless oil (0.230 g, 77%). **<sup>1</sup>H NMR** (CDCl<sub>3</sub>)  $\delta_{\text{H}}$  3.92 (3H, s, 2), 4.71 (2H, s, CH<sub>2</sub>OH), 4.96 (2H, s, CH<sub>2</sub>CCl<sub>3</sub>), 6.95 (1H, dd,  $J = 1.91, 7.27$  Hz, H-5), 7.08 (1H, d,  $J = 1.79$  Hz, H-6), 7.37 (1H, d, 8.27 Hz, H-3), OH peak not observed. Molecular ion not observed by **HRMS**. **LRMS**  $m/z$  [M+H]<sup>+</sup> = 401, C<sub>10</sub>H<sub>11</sub>Cl<sub>3</sub>O<sub>6</sub>S required 365.60.

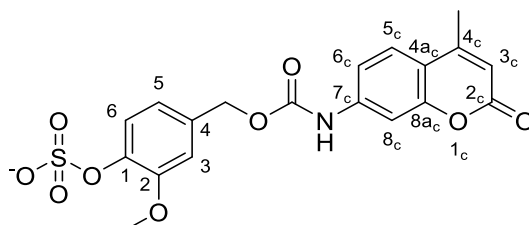
## Experimental

### 2-methoxy-4-((((4-methyl-2-oxo-2H-chromen-7-yl)carbamoyl)oxy)methyl)phenyl (2,2,2-trichloroethyl) sulfate (**5c**)



Following **general procedure C**, benzyl alcohol **7c** (0.16 g, 0.42 mmol) was reacted to afford carbamate **5c**. *ii*) benzyl alcohol **7c** stirred in the reaction mixture at room temperature for 70 h. The reaction quenched with H<sub>2</sub>O (5 mL) and the mixture concentrated *in vacuo*. The crude residue was suspended in EtOAc (50 mL) and filtered through diatomaceous earth and collecting the filtrate. The solution was washed with H<sub>2</sub>O (20 mL) and extracted with EtOAc (3x 50 mL) then dried and concentrated *in vacuo*. The crude residue was purified by repeat trituration (3x 5 mL) in MeOH to afford the title product **5c** (0.12 g, 54%). <sup>1</sup>H NMR (d<sub>6</sub>-DMSO) δ<sub>H</sub> 2.38 (3H, s, H-4<sub>c</sub>), 3.90 (3H, s, H-2), 5.20 (2H, s, CH<sub>2</sub>OCON), 5.30 (2H, s, CH<sub>2</sub>Cl<sub>3</sub>), 6.23 (1H, s, H-3<sub>c</sub>), 7.13 (1H, d, *J* = 7.86 Hz, H-5), 7.37 (1H, s, H-3), 7.41 (1H, d, *J* = 8.72, H-6<sub>c</sub>), 7.51 (1H, d, *J* = 8.29 Hz, 6) 7.55 (1H, s, H-8<sub>c</sub>), 7.69 (1H, d, *J* = 8.67 Hz, H-5<sub>c</sub>), 10.32 (1H, s, NH). <sup>13</sup>C NMR (d<sub>6</sub>-DMSO), δ<sub>C</sub> 17.9 (CH<sub>3</sub>, 4<sub>c</sub>), 56.2 (CH<sub>3</sub>, 2), 65.6 (CH<sub>2</sub>OCON), 79.9 (CH<sub>2</sub>CCl<sub>3</sub>), 92.8 (CCl<sub>3</sub>), 104.5 (CH 8<sub>c</sub>) 111.9 (CH, 3), 113.6 (CH, 3<sub>c</sub>), 114.3 (CH, 6<sub>c</sub>), 114.4 (C 4<sub>ac</sub>), 120.4 (CH, 5), 122.8 (CH, 6), 126.0 CH, 5<sub>c</sub>), 137.6 (C, 4), 138.0 (C, 1), 142.5 (C, 7<sub>c</sub>), 150.8 (C, 2), 153.0 (C, 4<sub>c</sub>), 153.1 (C, 8<sub>ac</sub>) 153.8 (C, OCON), 159.9 (C, 2<sub>c</sub>). LRMS *m/z* [M+H]<sup>+</sup> = 567, C<sub>21</sub>H<sub>18</sub>Cl<sub>3</sub>NO<sub>9</sub>S required 566.78

### 2-methoxy-4-((((4-methyl-2-oxo-2H-chromen-7-yl)carbamoyl)oxy)methyl)phenyl sulfate (**1c**)



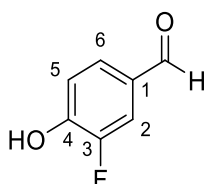
Following **general procedure D**, carbamate **5c** (0.05 g, 0.09 mmol) was reduced to **1c** over 18 h. The reaction mixture was and concentrated *in vacuo* and the crude residue was suspended in MeOH, evaporated onto silica and purified by flash column chromatography (0 -20% MeOH



## Experimental

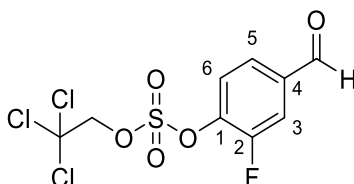
in EtOAc) to yield **1c** as a white powder (0.04 g, 87%, HPLC purity = 99%).  $^1\text{H NMR}$  ( $\text{CDOD}_3$ ),  $\delta_{\text{H}}$  2.45 (3H, d,  $J = 1.09$  Hz, 4<sub>c</sub>), 3.85 (3H, s, 2), 5.17 (2H, s,  $\text{CH}_2\text{CCl}_3$ ), 6.19 (1H, s, H-3<sub>c</sub>), 6.98 (1H, dd,  $J = 2.0, 8.32$  Hz, H-5), 7.11 (1H, d,  $J = 1.94$  Hz, H-3), 7.40 (1H, dd,  $J = 2.13, 8.7$  Hz, 6<sub>c</sub>), 7.45 (1H, d,  $J = 8.21$  Hz, 6), 7.63 (1H, d,  $J = 2.06$  Hz, 8<sub>c</sub>), 7.68, (1H, d,  $J = 8.73$  Hz, 5<sub>c</sub>). 10.29 (1H, s, NH).  $^{13}\text{C NMR}$  ( $\text{d}_6\text{-DMSO}$ )  $\delta_{\text{C}}$  17.9 ( $\text{CH}_3$ , 4<sub>c</sub>), 55.7 ( $\text{CH}_3$ , 2), 66.4 ( $\text{CH}_2\text{OCON}$ ), 104.4 (CH, 8<sub>c</sub>), 111.8 (CH, 3), 113.1 (CH, 3<sub>c</sub>), 114.2 (CH, 6<sub>c</sub>), 114.2 (C 4<sub>a</sub>), 120.4 (CH, 5), 120.7 (CH, 6), 126.0 (CH, 5<sub>c</sub>), 130.9 (C 4), 142.7 (2C 7<sub>c</sub>,1), 150.4 (C 2), 153.2 (2C 4<sub>c</sub>,8<sub>a</sub>), 153.8 (OCON), 160.0 (C 2<sub>c</sub>). HRMS  $m/z$   $[\text{M}]^- = 434.403$ ,  $\text{C}_{19}\text{H}_{16}\text{NO}_9\text{S}^-$  required 434.403.

### 3-fluoro-4-hydroxybenzaldehyde (**9d**)



4-methoxybenzaldehyde **18** (0.800, 5.2 mmol) in  $\text{HBr}_{(\text{aq})}$  (48%, 30 mL) was stirred at 110 °C under reflux for 48 h. The reaction was diluted with  $\text{H}_2\text{O}$  (50 mL) and extracted in DCM (4 x 100 mL) dried and concentrated *in vacuo* to afford the crude residue as a red powder. The crude residue was purified by column chromatography (20-40% EtOAc- $\text{X}_4$ ) to yield the title product **9d** as a colourless oil crystallising in DCM (0.648 g, 82%).  $^1\text{H NMR}$  ( $\text{CDCl}_3$ ),  $\delta_{\text{H}}$  7.07 (1H, d,  $J = 8.6$  Hz, H-2), 7.57 (2H, m, H-5, 6), 9.76 (1H, d,  $J = 2.0$  Hz, CHO), OH proton not observed. Melting point 120-124 °C. LRMS  $m/z$   $[\text{M}+\text{H}]^+ = 140$ ,  $\text{C}_7\text{H}_5\text{FO}_2$  required 140.11.  $^1\text{H NMR}$  and melting point consistent with characterisation by previously reported literature (189).

### 2-fluoro-4-formylphenyl (2,2,2-trichloroethyl) sulfate (**8d**)

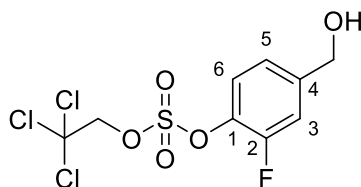


Following general procedure A, benzaldehyde **9d** (0.04 g, 0.28 mmol) reacted to yield benzaldehyde **8d**. Following work up the crude residue was purified by flash column

## Experimental

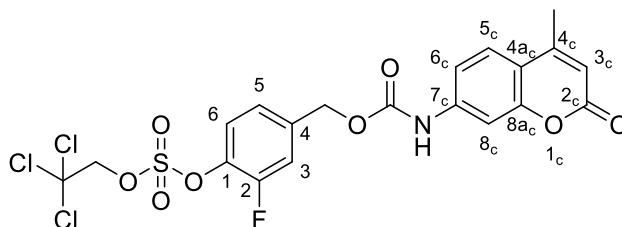
chromatography (30% EtOAc-X<sub>4</sub>) to afford **8d** as a white solid (0.055 g, 55%). <sup>1</sup>H NMR (CDCl<sub>3</sub>), δ<sub>H</sub> 4.9 (2H, s, CH<sub>2</sub>CCl<sub>3</sub>), 7.64 (1H, m, H-3), 7.77 (2H, m, H-5, 3), 10.0 (1H, d, *J* = 2.0 Hz, CHO). LRMS *m/z* [M+H]<sup>+</sup> = 386, C<sub>9</sub>H<sub>6</sub>Cl<sub>3</sub>FO<sub>5</sub>S required 351.55.

### 2-fluoro-4-(hydroxymethyl)phenyl (2,2,2-trichloroethyl) sulfate (7d)



Following **general procedure B**, benzaldehyde **8d** (0.090g, 0.25 mmol), was reduced to afford **7d**. After workup the crude residue was purified by column chromatography (20% EtOAc-X<sub>4</sub>) to yield the title product **7d** as a clear oil (0.090g, 99%). <sup>1</sup>H NMR (CDCl<sub>3</sub>) δ<sub>H</sub> 4.73 (2H, d, *J* = 5.3 Hz, CH<sub>2</sub>OH), 4.91 (2H, s, CH<sub>2</sub>CCl<sub>3</sub>), 7.19 (1H, dd, *J* = 1.3, 9.0 Hz, H-6), 7.29 (1H, dd, *J* = 1.9, 10.9 Hz, H-5), 7.44 (1H, t, *J* = 7.8 Hz, H-3), OH peak not observed. LRMS *m/z* [M+H]<sup>+</sup> = 389, C<sub>9</sub>H<sub>8</sub>Cl<sub>3</sub>FO<sub>5</sub>S required 353.57

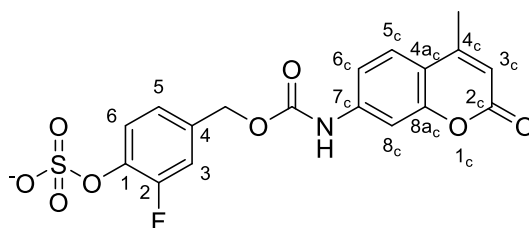
### 2-fluoro-4-((((4-methyl-2-oxo-2H-chromen-7-yl)carbamoyl)oxy)methyl)phenyl (2,2,2-trichloroethyl) sulfate (5d)



Following **general procedure C**, benzyl alcohol **7d** (0.09g, 0.25 mmol) reacted to afford carbamate **5d**. The reaction produced a thick white suspension. The reaction was quenched with H<sub>2</sub>O (5 mL) and precipitate filtered off. The filtrate was concentrated *in vacuo* and the crude residue evaporated onto silica. Purification by column chromatography (0.1-2.5 % MeOH-DCM) and trituration in Methanol (5 mL) was unsuccessful affording a mixture with residual **3**. The presence of **5d** was confirmed by TLC, LRMS and <sup>1</sup>H NMR analysis and the crude mixture was carried through without further purification. LRMS *m/z* [M+H]<sup>+</sup> = 555, C<sub>20</sub>H<sub>15</sub>Cl<sub>3</sub>FO<sub>8</sub>S required 554.75.

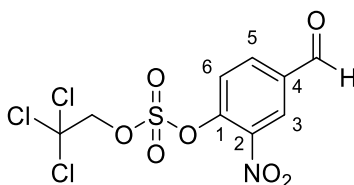
## Experimental

### 2-fluoro-4-((((4-methyl-2-oxo-2H-chromen-7-yl)carbamoyl)oxy)methyl)phenyl sulfate



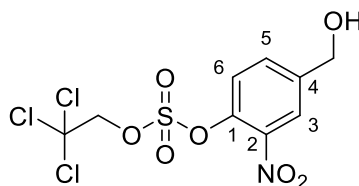
Following **general procedure D**, a mixed fraction of **5d** (0.05 g, ~ 0.09 mmol) was deprotected to yield **1d**. No reduction was observed by TLC and **LRMS** after 2 hours and a further portion of Zn dust (0.02 g, 0.36 mmol) and ammonium formate (0.07 g, 0.98 mmol) were added to the mixture and stirred vigorously for another 2 h. After 2 hours neither **5d** or **1d** were observed by TLC or **LRMS** analysis. The reaction was concentrated *in vacuo* and the crude residue was suspended in MeOH. TLC and **LRMS** of the crude mixture confirmed the presence of **1d** and the mixture was evaporated onto silica. **1d** was purified by column chromatography (1-30% MeOH-DCM) to afford the title product (0.01 g, 9% yield from **7d**, **HPLC** purity 95%). **<sup>1</sup>H NMR**  $\delta_{\text{H}}$  2.45 (3H, d,  $J = 1.2$  Hz, H-4<sub>c</sub>), 5.18 (2H, s, CH<sub>2</sub>), 6.20 (1H, d,  $J = 1.2$  Hz, 3<sub>c</sub>), 7.17-7.22 (2H, m, H-5, 5<sub>c</sub>), 7.41 (1H, dd,  $J = 2.1, 8.7$  Hz, H-5<sub>c</sub>), 7.53, 1H, d,  $J = 8.2$  Hz, H-6), 7.63 (1H, d,  $J = 2.0$  Hz, H-3), 7.68 (1H, d,  $J = 8.8$  Hz, 6<sub>c</sub>). **<sup>13</sup>C NMR** acquisition prevented by limited compound supply. **HRMS**  $m/z$  [M]<sup>-</sup> = 422.035, C<sub>19</sub>H<sub>15</sub>FNO<sub>8</sub>S<sup>-</sup> required 422.0422

### 4-formyl-2-nitrophenyl (2,2,2-trichloroethyl) sulfate (**8e**)



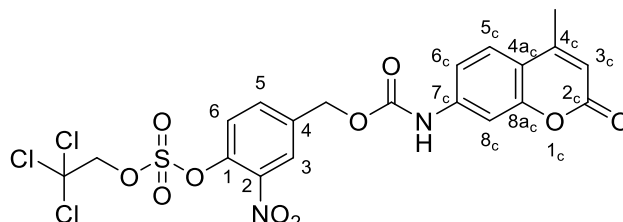
Following **general procedure A**, 4-hydroxy-2-nitrobenzaldehyde **9e** (0.10 g, 0.60 mmol) reacted to afford benzaldehyde **8e**. Following workup, the crude residue was purified by column chromatography (20% EtOAc-X<sub>4</sub>) to yield the title product **9e** as a brown oil (0.14 g, 64%). **<sup>1</sup>H NMR** (CDCl<sub>3</sub>)  $\delta_{\text{H}}$  5.01 (2H, CH<sub>2</sub>Cl<sub>3</sub>), 7.89 (1H, d,  $J = 8.49$  Hz, H-6), 8.24 (1H, dd,  $J = 2.04, 8.50$  Hz, H-5), 8.58 (1H, d,  $J = 2.01$  Hz, H-3), 10.09 (1H, s, CHO). **LRMS**  $m/z$  [M+H]<sup>+</sup> = 413, C<sub>9</sub>H<sub>6</sub>Cl<sub>3</sub>NO<sub>7</sub>S required 378.56

## 4-(hydroxymethyl)-2-nitrophenyl (2,2,2-trichloroethyl) sulfate (7e)



Following **general procedure B**, benzaldehyde **8e** (0.12 g, 0.33 mmol) was reduced to afford benzyl alcohol **7e**. Following work up the crude residue was purified by column chromatography to yield the title product **7e** as a clear oil (0.11 g, 88%).  $^1\text{H NMR}$  ( $\text{CDCl}_3$ )  $\delta_{\text{H}}$  4.84 (2H, d,  $J = 3.56$  Hz,  $\text{CH}_2\text{OH}$ ), 4.97 (2H, s,  $\text{CH}_2\text{CCl}_3$ ), 7.65 (1H, d,  $J = 8.51$  Hz, H-6), 7.72 (1H, dd,  $J = 2.12, 8.59$  Hz, H-5) 8.12 (1H, d,  $J = 2.03$  Hz, H-3), *OH* peak not observed.  $^{13}\text{C NMR}$  ( $\text{CDCl}_3$ )  $\delta_{\text{C}}$  61.2 ( $\text{CH}_2\text{OH}$ ), 80.4 ( $\text{CH}_2\text{CCl}_3$ ), 92.6 ( $\text{CH}_2\text{CCl}_3$ ), 123.7 (CH, 3) 124.0 (CH, 5), 133.0 (CH, 6) 139.2 (C, 4), 141.4 (C, 1), 144.8 (C, 2). **HRMS**  $m/z$   $[\text{M}+\text{H}]^+ = 377.9020$ ,  $\text{C}_9\text{H}_8\text{Cl}_3\text{NO}_7\text{S}$  required 378.9093.

## 4-(((4-methyl-2-oxo-2H-chromen-7-yl)carbamoyloxy)methyl)-2-nitrophenyl (2,2,2-trichloroethyl) sulfate (5e)



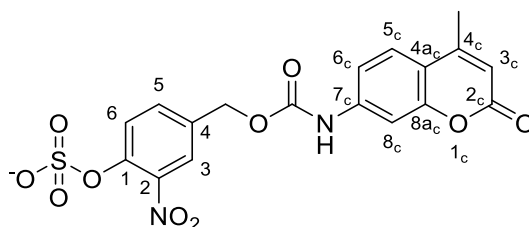
Following **general procedure C**, benzyl alcohol **7e** (0.19 g, 0.5 mmol) was reacted to afford **5e**. Following reaction for 62 hours the reaction mixture was a thick white suspension. The reaction was quenched with  $\text{H}_2\text{O}$  (5 mL) and concentrated *in vacuo*. The crude residue was triturated in MeOH, (5 mL x2) and the soluble fraction evaporated onto silica. **5e** was purified by flash column chromatography (0.1-5% MeOH-DCM) to yield the title product **5e** as a white solid (0.10 g, 34%).  $^1\text{H NMR}$  ( $d_4$ -DMSO)  $\delta_{\text{H}}$  2.39 (3H, d,  $J = 1.05$  Hz, H-4<sub>c</sub>), 5.34 (2H, s,  $\text{CH}_2\text{CCl}_3$ ), 6.24 (1H, d,  $J = 1.17$  Hz, 3<sub>c</sub>), 7.41 (1H, dd,  $J = 2.07, 8.7$  Hz, H-6<sub>c</sub>), 7.55 (1H, d,  $J = 2.01$  Hz, H-3), 7.71 (1H, d,  $J = 8.72$  Hz, 8<sub>c</sub>) 7.91 (1H, d,  $J = 8.5$  Hz, H-6), 8.00 (1H, dd,  $J = 2.10, 8.84$  Hz, H-5), 8.34 (1H, d,  $J = 2.05$  Hz, H-5<sub>c</sub>), 10.40 (1H, s, NH).  $^{13}\text{C NMR}$  ( $d_6$ -DMSO)  $\delta_{\text{C}}$  18.0 ( $\text{CH}_3$ , 4<sub>c</sub>), 64.3 ( $\text{CH}_2\text{OCON}$ ), 80.5 ( $\text{CH}_2\text{CCl}_3$ ), 92.6 ( $\text{CCl}_3$ ), 104.5 (CH 8<sub>c</sub>), 112.0 (CH 3<sub>c</sub>), 114.3 (CH 6<sub>c</sub>), 114.5 (C 4<sub>ac</sub>), 124.4 (CH, 3), 125.7 (CH 5), 126.1 (CH 5<sub>c</sub>), 134.9 (CH, 6),

## Experimental

138.4 (C 4), 140.2 (C 7<sub>c</sub>), 141.5 (C 2), 142.4 (C, 1), 152.8 (C 4<sub>c</sub>) 153.1 (C 8<sub>ac</sub>), 153.8 (OCON), 160.0 (C 2<sub>c</sub>). HRMS  $m/z$  [M]<sup>-</sup> = 580.9579, C<sub>20</sub>H<sub>15</sub>C<sub>13</sub>N<sub>2</sub>O<sub>10</sub>S required 580.9579.

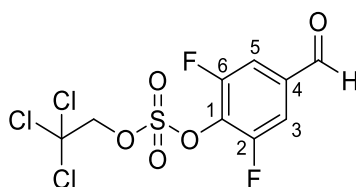
### 4-(((4-methyl-2-oxo-2H-chromen-7-yl)carbamoyloxy)methyl)-2-nitrophenyl sulfate

(1e)



To **5e** in DMF (5 mL) added 10% Pd/C (10% w/w, ~0.002g) and ammonium formate (0.02, 6 eq.) and stirred vigorously at 50 °C for 16 hours. TLC and LRMS analysis indicated no reaction had occurred and a further portion of 10% Pd/C (~0.015 g, 70% w/w) and ammonium formate (0.09, 42 eq.) and stirred vigorously at 70 °C for 1 h. The reaction mixture was concentrated *in vacuo* and the crude residue purified by flash column chromatography (0.1 – 30% MeOH-DCM) to yield **1e** as a white solid (0.01g, 62%, HPLC purity 96%). <sup>1</sup>H NMR (CD<sub>3</sub>OD) δ<sub>H</sub> 2.38 (3H, d, *J* = 1.14 Hz, 4<sub>c</sub>), 5.20 (2H, s, CH<sub>2</sub>OCON), 6.23 (1H, d, *J* = 1.21 Hz, 3<sub>c</sub>), 7.41 (1H, dd, *J* = 2.10, 8.70 Hz, 6<sub>c</sub>), 7.54 (1H, d, *J* = 2.0 Hz, H-3), 7.63 (1H, d, *J* = 8.24 Hz, H-6), 7.69 (2H, m, H – 8<sub>c</sub>, 5), 7.91 (1H, d, *J* = 2.0 Hz, H-5<sub>c</sub>), 10.32 (1H, s, NH). <sup>13</sup>C NMR (CD<sub>3</sub>OD) 18.0 (CH<sub>3</sub> 4<sub>c</sub>), 64.9 (CH<sub>2</sub>, CH<sub>2</sub>OCON), 104.5 (CH, 8<sub>c</sub>) 111.9 (CH, 3<sub>c</sub>), 114.3 (CH, 6<sub>c</sub>), 114.5 (C, 4<sub>ac</sub>), 123.5 (CH, 2), 124.0 (2CH, 3, 5), 126.1 (CH, 5<sub>c</sub>), 131.7 (C, 4), 133.2(CH, 6), 142.5 (C, 7<sub>c</sub>), 142.6 (C, 2), 145.6 (C, 1), 153.0 (C, 4<sub>c</sub>), 153.3 (C, 8<sub>ac</sub>), 153.8 (C, OCON), 160.1 (C, 2<sub>c</sub>). HRMS molecular ion not observed.

### 2,6-difluoro-4-formylphenyl (2,2,2-trichloroethyl) sulfate (8f)



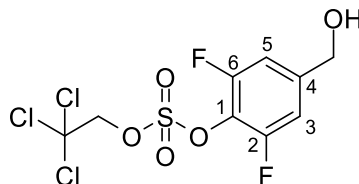
Following **general procedure A**, phenol **9f** was reacted to yield **8f**. The reaction was incomplete after 2 hours so added further portion of **14** (0.20 g, 0.3 eq.) and stirred for 30 minutes. Following workup the crude residue was purified by flash column chromatography to yield **8f** as a brown oil (0.13 g, 30%) and **9f** recovered as the major product. <sup>1</sup>H NMR (CDCl<sub>3</sub>)

## Experimental

$\delta_{\text{H}}$  4.99 (2H, d,  $J = 1.56$  Hz,  $\text{CH}_2\text{CCl}_3$ ), 7.61 (2H, sex,  $J = 1.04, 1.28, 2.33, 6.94$  Hz, H- 3, 5).

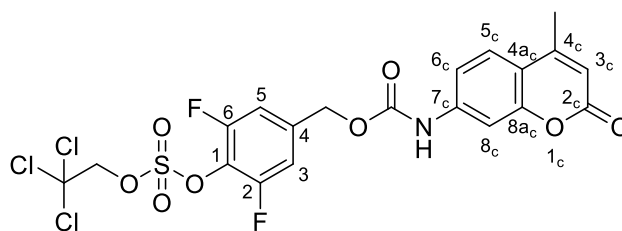
LRMS  $m/z$   $[\text{M}+\text{H}]^+ = 404$ ,  $\text{C}_9\text{H}_5\text{Cl}_3\text{F}_2\text{O}_5\text{S}$  required 369.54.

### 2,6-difluoro-4-(hydroxymethyl)phenyl (2,2,2-trichloroethyl) sulfate (7g)



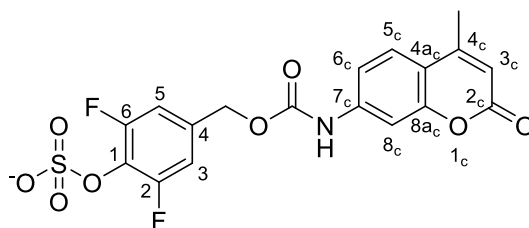
Following **general procedure B**, **8f** (0.13, 0.35 mM) was reduced to afford **7f**. Following workup the crude reaction residue was purified by flash column chromatography to yield **7a** as a clear oil (0.09 g, 72%) and **8f** as a minor product.  $^1\text{H NMR}$  ( $\text{CDCl}_3$ )  $\delta_{\text{H}}$  4.72 (2H, d,  $J = 5.5$  Hz,  $\text{CH}_2\text{OH}$ ), 4.96 (2H, s,  $\text{CH}_2\text{CCl}_3$ ), 7.09 (2H, q, 3.89, 8.31 Hz, H-3,5), *OH* peak not observed. LRMS  $m/z$   $[\text{M}+\text{H}]^+ = 407$ ,  $\text{C}_9\text{H}_7\text{Cl}_3\text{F}_2\text{O}_5\text{S}$  required 371.56.

### 2,6-difluoro-4-(((4-methyl-2-oxo-2H-chromen-7-yl)carbamoyl)oxy)methyl)phenyl (2,2,2-trichloroethyl) sulfate (5f)



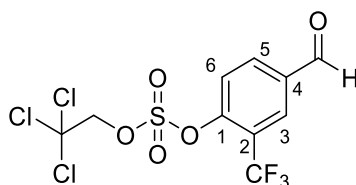
Following **general procedure C**, **7f** (0.07 g, 0.24 mM) was reacted to afford **5f** as a mixture with **3**. The reaction was stirred for 64 hours producing a thick white suspension. T added  $\text{H}_2\text{O}$  (5 mL) to quench the reaction and the precipitate filtered off washing with MeOH (20 mL). The filtrate was collected and concentrated *in vacuo*. The crude residue was unable to be purified by column chromatography (0.1-2.5 MeOH-DCM) affording a mixture with residual **3**. The presence of **5f** was a confirmed by TLC and LRMS  $m/z$   $[\text{M}+\text{H}]^+ = 572$ ,  $\text{C}_{20}\text{H}_{14}\text{Cl}_3\text{F}_2\text{NO}_8\text{S}$  required 572.74.

**2,6-difluoro-4-((((4-methyl-2-oxo-2H-chromen-7-yl)carbamoyl)oxy)methyl)phenyl sulfate (1f)**



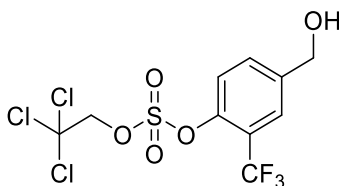
Following **general procedure D**, a mixture of **7f** and **3** (0.06 g) was reduced to afford **1e**. After 18 hours the reaction mixture was concentrated *in vacuo*. The crude residue was suspended in DMC (10mL) and precipitate filtered off. The filtrate was purified by flash column chromatography (0.1-30% MeOH-DCM) to yield **1f** (0.01 g, 11% total yield from **7f**, HPLC purity = 97%). <sup>1</sup>H NMR (CD<sub>3</sub>OD) δ<sub>H</sub> 2.45 (3H, d, *J* = 1.17 Hz, 4<sub>c</sub>), 5.18 (2H, s, CH<sub>2</sub>OCON), 6.20 (1H, d, *J* = 1.81 Hz, 3<sub>c</sub>), 6.98 (2H, d, *J* = 8.60 Hz, H-3,5), 7.41 (1H, dd, *J* = 2.14, 8.71 Hz, H-6<sub>c</sub>), 7.64 (1H, d, *J* = 2.05 Hz, H-8<sub>c</sub>), 7.69 (1H, d, *J* = 8.73 Hz, H-5<sub>c</sub>) NH peak not observed., HMRS *m/z* [M<sup>-</sup>] = 440.0260, C<sub>18</sub>H<sub>13</sub>F<sub>2</sub>NO<sub>8</sub>S required 441.0325. 7.10 (2H, d, *J* = 8.83 Hz, 3,5),

**4-formyl-2-(trifluoromethyl)phenyl (2,2,2-trichloroethyl) sulfate (8g)**



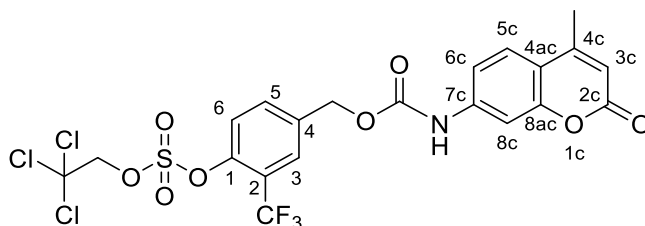
Following **general procedure A**, **9g** was reacted to afford **8g**. The reaction mixture was stirred at room temperature for 16 hours. Following workup the crude reaction residue was purified by flash column chromatography to yield **8g** (0.306 g, 73%). <sup>1</sup>H NMR (CDCl<sub>3</sub>) δ<sub>H</sub> 4.93 (2H, s, CH<sub>2</sub>Cl<sub>3</sub>), 7.91 (1H, d, *J* = 8.55 Hz, H-3), 8.19 (1H, dd, *J* = 2.02, 8.55 Hz, H-5), 8.27 (1H, d, *J* = 1.69 Hz, H-6), 10.07 (d, *J* = 2.04 Hz, CHO). LRMS *m/z* [M+H]<sup>+</sup> = 437, C<sub>10</sub>H<sub>6</sub>Cl<sub>3</sub>F<sub>3</sub>O<sub>5</sub>S required 401.56.

**4-formyl-2-(trifluoromethyl)phenyl (2,2,2-trichloroethyl) sulfate (7g)**



Following **general procedure B**, **8g** (0.30, 0.84 mmol) was reduced to afford **7g**. After workup the reaction residue was purified by flash column chromatography to afford **7g** as a colourless oil (0.11 g, 36%) and a second impure fraction.  $^1\text{H NMR}$  ( $\text{CDCl}_3$ )  $\delta_{\text{H}}$  4.79 (2H, s,  $\text{CH}_2\text{OH}$ ), 4.92 (2H, s,  $\text{CH}_2\text{CCl}_3$ ), 7.66 (2H, m, H-5,3), 7.75 (1H, d,  $J = 0.70$  Hz, H-6), OH peak not observed. **LRMS**  $m/z$   $[\text{M}+\text{H}]^+ = 439$ ,  $\text{C}_{10}\text{H}_8\text{Cl}_3\text{F}_3\text{O}_5\text{S}$  required 403.57.

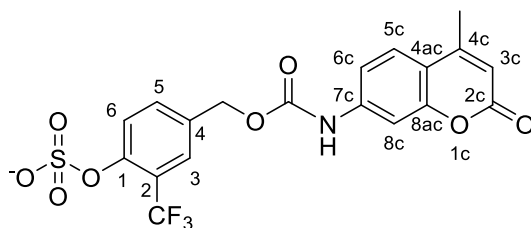
**4-(((4-methyl-2-oxo-2H-chromen-7-yl)carbamoyl)oxy)methyl)-2-(trifluoromethyl)phenyl (2,2,2-trichloroethyl) sulfate (5g)**



Following **general procedure C**, **7g** (0.11 g, 0.27 mmol) was reacted to afford **5g**. The reaction mixture was stirred for 1 week producing a thick white suspension. The reaction was quenched with  $\text{H}_2\text{O}$  (5 mL) and precipitate filtered off, washing with MeOH (20 mL). The filtrate was concentrated *in vacuo* and the crude residue purified by flash column chromatography (0.1-2.5% MeOH-DCM) and trituration of fractions in MeOH collecting pure **5g** in the filtrate (0.11 g, 55%).  $^1\text{H NMR}$  ( $\text{d}_6\text{-DMSO}$ )  $\delta_{\text{H}}$  2.39 (3H, d,  $J = 0.97$  Hz, H-4<sub>c</sub>), 5.31 (2H, s,  $\text{CH}_2\text{OCON}$ ), 5.48 (2H, s,  $\text{CH}_2\text{CCl}_3$ ), 6.24 (1H, d,  $J = 1.13$  Hz, H-3<sub>c</sub>), 7.41 (1H, d,  $J = 2.0, 8.7$  Hz, H-6<sub>c</sub>), 7.55 (1H, d,  $J = 1.96$  Hz, H-6), 7.71 (1H, d,  $J = 8.75$  Hz, H-8<sub>c</sub>), 7.81 (1H, d,  $J = 8.53$  Hz, H-3), 7.96 (1H, d,  $J = 8.67$  Hz, H-5<sub>c</sub>) 8.03 (1H, dd,  $J = 1.78, 6.99$  Hz, H-5), 10.36 (1H, s, NH). **LRMS**  $m/z$   $[\text{M}+\text{H}]^+ = 605$ ,  $\text{C}_{21}\text{H}_{15}\text{Cl}_3\text{F}_3\text{NO}_8\text{S}$  required 604.76.

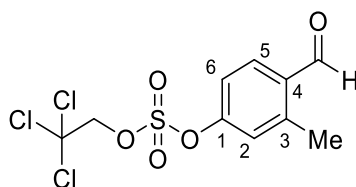


**4-(((4-methyl-2-oxo-2H-chromen-7-yl)carbamoyl)oxy)methyl)-2-(trifluoromethyl)phenyl sulfate (1g)**

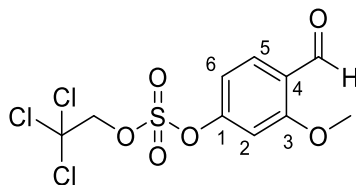


Following **general procedure D**, **5g** (0.11 g, 0.18 mmol) was reduced to afford **1g**. After 2 hours the Zn had been consumed and TLC and LRMS analysis reported the reaction was not complete. A further portion of Zn (4 eq.) and ammonium formate (6 eq.) and stirred at room temperature for 30 minutes. The reaction mixture was concentrated *in vacuo* and the crude residue purified by flash column chromatography (0-30% MeOH-DCM) to yield **1g** as a white solid (0.02 g, 22%, **HPLC** purity = 98%). **<sup>1</sup>H NMR** (CD<sub>3</sub>OD)  $\delta_{\text{H}}$  2.45 (3H, d,  $J = 1.18$  Hz, H-4<sub>c</sub>) 5.23 (2H, s, CH<sub>2</sub>OCON), 6.20 (1H, d,  $J = 1.18$  Hz, H-3<sub>c</sub>), 7.39 (1H, dd,  $J = 2.14, 8.71$  Hz, H-6<sub>c</sub>), 7.63 (1H, d,  $J = 2.14$  Hz, H-8<sub>c</sub>), 7.68 (3H, m, H-3, 5<sub>c</sub>, 6), 7.85 (1H, d,  $J = 8.58$  Hz, H-5). The NH peak was not observed. **<sup>13</sup>C NMR** (CD<sub>3</sub>OD)  $\delta_{\text{C}}$  18.7 (CH<sub>3</sub> 4<sub>c</sub>), 66.9 (CH<sub>2</sub>), 106.5 (CH 8<sub>c</sub>), 113.1 (CH 3<sub>c</sub>), 116.1 (C 4<sub>ac</sub>), 116.4 (CH 6<sub>c</sub>), 122.5 (C 5), 122.9 (CH 6), 123.4 (C CF<sub>3</sub>), 126.1 (CH 5<sub>c</sub>), 126.9 (CH 3), 127.7 (C 4), 134.2 (C 1), 144.5 (C 7<sub>c</sub>), 152.3 (C 4<sub>c</sub>), 155.2 (C 2), 155.7 (C 8<sub>ac</sub>), 155.8 (C OCNO), 163.6 (2<sub>c</sub>). **HRMS**  $m/z$  [M]<sup>-</sup> = 472.0322, C<sub>18</sub>H<sub>14</sub>F<sub>3</sub>NO<sub>8</sub>S required 473.0387.

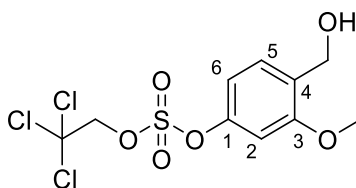
**4-formyl-3-methylphenyl (2,2,2-trichloroethyl) sulfate (8h)**



Following **general procedure A**, phenol **9h** (0.30 g, 1.96 mmol) was reacted to afford **8h**. Following work up the crude reaction residue was purified by column chromatography (20% EtOAc-X<sub>4</sub>) to yield **8h** (0.28 g, 29%). **<sup>1</sup>H NMR**  $\delta_{\text{H}}$  (CDCl<sub>3</sub>), 2.48 (3H, s, H-3), 4.87 (2H, s, CH<sub>2</sub>CCl<sub>3</sub>), 7.57 (1H, d,  $J = 8.36$  Hz, H-5), 7.70 (1H, ddd,  $J = 0.47, 1.62, 8.38$  Hz, H-6), 7.82 (1H, d,  $J = 0.48$  Hz, H-2), 10.00 (1H, s, CHO). **LRMS**  $m/z$  [M+H]<sup>+</sup> = 393, C<sub>10</sub>H<sub>9</sub>Cl<sub>3</sub>O<sub>5</sub>S required 347.59.

**4-formyl-3-methoxyphenyl (2,2,2-trichloroethyl) sulfate (8i)**

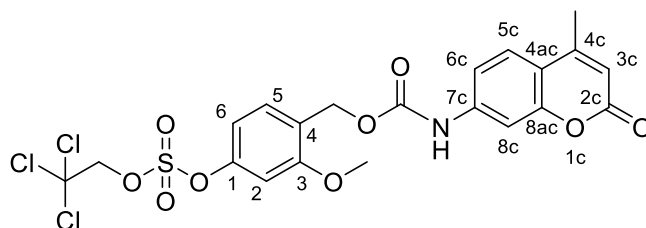
Following **general procedure A**, phenol **9i** (0.30 g, 1.96 mmol) was reacted to afford **8i**. Following work up the crude reaction residue was purified by flash column chromatography to yield **8i** as a brown oil (0.46 g, 65%).  $^1\text{H NMR}$   $\delta_{\text{H}}$  3.96 (3H, s, OMe), 4.87 (2H, s,  $\text{CH}_2\text{CCl}_3$ ), 7.02 (2H, m, H-2, 6), 7.91 (1H, d,  $J = 8.3$  Hz, H-5), 10.41 (1H, s, CHO).  $^{13}\text{C NMR}$   $\delta_{\text{C}}$  56.42 ( $\text{CH}_3$ ), 80.7 ( $\text{CH}_2$ ), 92.4 (C  $\text{CCl}_3$ ), 105.2 (CH), 113.3 (CH), 124.3 (C), 130.7 (CH), 155.1 (C), 163.1 (C), 188.2 (CHO). Molecular ion not observed by **HRMS**, **LRMS**  $m/z$   $[\text{M}+\text{H}]^+ = 398$ ,  $\text{C}_{10}\text{H}_9\text{Cl}_3\text{O}_6\text{S}$  required 363.59.

**4-(hydroxymethyl)-3-methoxyphenyl (2,2,2-trichloroethyl) sulfate (7i)**

Following **general procedure B**, aldehyde **8i** (0.15 g, 0.4 mmol) was reduced to afford **7i**. Following work up the crude reaction residue was purified by flash column chromatography (20% EtOAc- $\text{X}_4$ ), to yield alcohol **7i** as a clear oil (0.09 g, 60%)  $^1\text{H NMR}$  ( $\text{CDCl}_3$ )  $\delta_{\text{H}}$  3.87 (3H, s, OMe), 4.68 (2H, d,  $J = 6.09$  Hz,  $\text{CH}_2\text{OCON}$ ), 4.83 (2H, s,  $\text{CH}_2\text{Cl}_3$ ), 6.88 (1H, d,  $J = 2.29$  Hz, H-2), 6.95 (1H, dd,  $J = 2.31, 8.24$  Hz, H-6), 7.36 (1H, d,  $J = 8.26$  Hz, H-5), OH peak not observed.  $^{13}\text{C NMR}$   $\delta_{\text{C}}$  56.0 ( $\text{CH}_3$ ), 61.3 ( $\text{CH}_2, \text{CH}_2\text{OH}$ ), 80.6 ( $\text{CH}_2, \text{CH}_2\text{CCl}_3$ ), 104.2 (CH), 122.9 (CH), 129.2 (C 4), 129.5 (CH), 150.5 (C, 1), 158.4 (C, 2). Molecular ion not observed by **HRMS**. **LRMS**  $m/z$   $[\text{M}+\text{H}]^+ = 401$ ,  $\text{C}_{10}\text{H}_{11}\text{Cl}_3\text{O}_6\text{S}$  required 365.60.

## Experimental

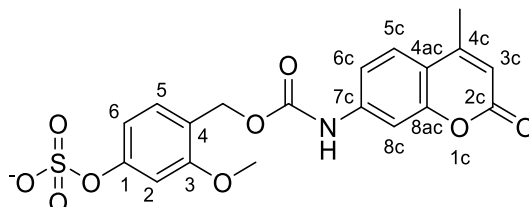
### 3-methoxy-4-((((4-methyl-2-oxo-2H-chromen-7-yl)carbamoyl)oxy)methyl)phenyl (2,2,2-trichloroethyl) sulfate (**5i**)



Following **general procedure C**, alcohol **7i** (0.06 g, 0.68 mmol) was reacted to afford **5i**. Prior to the reaction stock **AMC** was dissolved in DCM and concentrated *in vacuo*. Following addition of **7i** the reaction was stirred at room temperature for 18 hours becoming a brown suspension. The reaction was quenched with H<sub>2</sub>O and precipitate filtered off washing with MeOH. The filtrate was concentrated *in vacuo* and the crude reaction mixture purified by flash column chromatography (0.1 – 2.5% MeOH-DCM) collecting fractions with **5i** and trituration of the crude fractions in MeOH collecting **5i** in the filtrate. The filtrate was concentrated *in vacuo* to yield **5i** as a white solid (0.05 g, 13%). <sup>1</sup>H NMR (d<sub>6</sub>-DMSO) δ<sub>H</sub> 2.29 (3H, d, *J* = 0.85 Hz, H-4<sub>c</sub>), 3.88 (3H, s, OMe), 4.31 (2H, d, *J* = 5.92 Hz, CH<sub>2</sub>OCO), 5.37 (2H, s, CH<sub>2</sub>CCl<sub>3</sub>), 5.91 (1H, d, *J* = 1.04 Hz, 3<sub>c</sub>), 6.36 (1H, d, *J* = 2.15 Hz, 8<sub>c</sub>), 6.62 (1H, dd, *J* = 2.2, 8.7 Hz, H-6<sub>c</sub>), 7.04 (1H, dd, *J* = 2.32, 8.37 Hz, H-6), 7.17 (1H, d, *J* = 2.33 Hz, H-2), 7.31 (1H, d, *J* = 8.39 Hz, H-5), 7.46 (1H, d, *J* = 8.77 Hz, H-5<sub>c</sub>), 10.36 (1H, s, NH).

**LRMS** *m/z* [M+H]<sup>+</sup> = 566, C<sub>12</sub>H<sub>18</sub>Cl<sub>3</sub>NO<sub>9</sub>S required 566.78.

### 3-methoxy-4-((((4-methyl-2-oxo-2H-chromen-7-yl)carbamoyl)oxy)methyl)phenyl sulfate (**1i**)

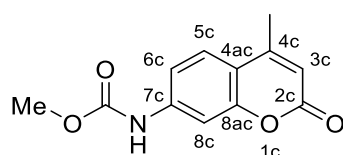


Following **general procedure D**, **5i** (0.02 g, 0.04 mmol) was reduced to afford **1i**. After 18 hours the TLC and LRMS saw no formation of **1i**, and a further portion of Zn (12 eq.) and ammonium formate (24 eq.) and stirred vigorously at room temperature for 6 hours. The reaction was concentrated *in vacuo* and the crude reaction residue purified by flash column

## Experimental

chromatography (2%-40% MeOH-DCM). The resulting white solid was freeze dried to afford **1i** (0.01g, 62%, HPLC purity = 95%).  $^1\text{H NMR}$  ( $\text{CD}_3\text{OD}$ )  $\delta_{\text{H}}$  2.37 (3H, d,  $J = 0.99$  Hz, H-4<sub>c</sub>), 3.89 (3H, s, H-3), 4.58 (2H, s, CH<sub>2</sub>), 6.43 (1H, d,  $J = 2.29$  Hz, H-2), 6.65 (1H, dd,  $J = 2.29$ , 8.78 Hz, H-6), 6.82 (1H, dd,  $J = 2.17$ , 8.26 Hz, H-6<sub>c</sub>), 6.95 (1H, d,  $J = 2.13$  Hz, H-8<sub>c</sub>), 7.20 (1H, d,  $J = 8.25$  Hz, H-5), 7.45 (1H, d,  $J = 8.81$  Hz, H-5<sub>c</sub>).  $^{13}\text{C NMR}$  ( $\text{CD}_3\text{OD}$ )  $\delta_{\text{C}}$  18.7 (CH<sub>3</sub>), 42.6 (CH<sub>2</sub>) 56.2 (CH<sub>3</sub>), 105.4 (CH), 111.1 (CH), 114.3 (C), 124.3 (2C), 126.9 (CH), 127.0 (CH), 127.3 (CH), 129.7 (CH), 130.6 (CH) 154.43 (2C) 156.7 (2C), 157.7 (C), 159.3 (C). HRMS  $m/z$  [ $\text{M}$ ]<sup>-</sup> = 434.0516, C<sub>19</sub>H<sub>17</sub>NO<sub>9</sub>S<sup>-</sup> required 435.0590

### methyl (4-methyl-2-oxo-2H-chromen-7-yl)carbamate (**22**)



Following **general procedure D**, MeOH (20 mL) was reacted to afford methylcarbamate **22**. Following removal of excess phosgene, MeOH (20 mL) was added to the reaction mixture and left to stir at room temperature for 2 hours. The reaction mixture became a white suspension and was quenched with additional MeOH (20 mL). The reaction mixture was concentrated *in vacuo* and suspended in MeOH and filtered collecting the purified **22** as a white solid. Yield not recorded.  $^1\text{H NMR}$  consistent with previous literature(186).

# References:

## References

1. Cancer [Internet]. [cited 2022 Apr 23]. Available from: <https://www.who.int/health-topics/cancer>
2. DeVita VT, Chu E. A history of cancer chemotherapy. *Cancer Res.* 2008 Nov 1;68(21):8643–53.
3. Leyland-Jones B. Trastuzumab: hopes and realities. *The Lancet Oncology.* 2002 Mar 1;3(3):137–44.
4. Zahavi D, Weiner L. Monoclonal Antibodies in Cancer Therapy. *Antibodies.* 2020 Sep;9(3):34.
5. Keizer RJ, Huitema ADR, Schellens JHM, Beijnen JH. Clinical Pharmacokinetics of Therapeutic Monoclonal Antibodies. *Clin Pharmacokinet.* 2010 Aug 1;49(8):493–507.
6. Hansel TT, Kropshofer H, Singer T, Mitchell JA, George AJT. The safety and side effects of monoclonal antibodies. *Nat Rev Drug Discov.* 2010 Apr;9(4):325–38.
7. Chames P, Van Regenmortel M, Weiss E, Baty D. Therapeutic antibodies: successes, limitations and hopes for the future. *British Journal of Pharmacology.* 2009;157(2):220–33.
8. Beckman RA, Weiner LM, Davis HM. Antibody constructs in cancer therapy. *Cancer.* 2007;109(2):170–9.
9. Czuczman MS, Olejniczak S, Gowda A, Kotowski A, Binder A, Kaur H, et al. Acquisition of Rituximab Resistance in Lymphoma Cell Lines Is Associated with Both Global CD20 Gene and Protein Down-Regulation Regulated at the Pretranscriptional and Posttranscriptional Levels. *Clin Cancer Res.* 2008 Mar 1;14(5):1561–70.
10. Joubert N, Beck A, Dumontet C, Denevault-Sabourin C. Antibody–Drug Conjugates: The Last Decade. *Pharmaceuticals.* 2020 Sep;13(9):245.
11. Chau CH, Steeg PS, Figg WD. Antibody–drug conjugates for cancer. *The Lancet.* 2019 Aug 31;394(10200):793–804.
12. Lehar SM, Pillow T, Xu M, Staben L, Kajihara KK, Vandlen R, et al. Novel antibody–antibiotic conjugate eliminates intracellular *S. aureus*. *Nature.* 2015 Nov;527(7578):323–8.
13. Bross PF, Beitz J, Chen G, Chen XH, Duffy E, Kieffer L, et al. Approval Summary: Gemtuzumab Ozogamicin in Relapsed Acute Myeloid Leukemia. *Clin Cancer Res.* 2001 Jun 1;7(6):1490–6.
14. de Claro RA, McGinn K, Kwitkowski V, Bullock J, Khandelwal A, Habtemariam B, et al. U.S. Food and Drug Administration Approval Summary: Brentuximab Vedotin for the Treatment of Relapsed Hodgkin Lymphoma or Relapsed Systemic Anaplastic Large-Cell Lymphoma. *Clin Cancer Res.* 2012 Nov 1;18(21):5845–9.
15. Ballantyne A, Dhillon S. Trastuzumab Emtansine: First Global Approval. *Drugs.* 2013 May 1;73(7):755–65.

## References

16. Jen EY, Ko CW, Lee JE, Valle PLD, Aydanian A, Jewell C, et al. FDA Approval: Gemtuzumab Ozogamicin for the Treatment of Adults with Newly Diagnosed CD33-Positive Acute Myeloid Leukemia. *Clin Cancer Res*. 2018 Jul 15;24(14):3242–6.
17. Beck A, Goetsch L, Dumontet C, Corvaia N. Strategies and challenges for the next generation of antibody–drug conjugates. *Nat Rev Drug Discov*. 2017 May;16(5):315–37.
18. Lee A. Loncastuximab Tesirine: First Approval. *Drugs*. 2021 Jul 1;81(10):1229–33.
19. Markham A. Tisotumab Vedotin: First Approval. *Drugs*. 2021 Dec 1;81(18):2141–7.
20. Research C for DE and. FDA grants accelerated approval to mirvetuximab soravtansine-gynx for FR $\alpha$  positive, platinum-resistant epithelial ovarian, fallopian tube, or peritoneal cancer. FDA [Internet]. 2022 Nov 14 [cited 2022 Dec 31]; Available from: <https://www.fda.gov/drugs/resources-information-approved-drugs/fda-grants-accelerated-approval-mirvetuximab-soravtansine-gynx-fra-positive-platinum-resistant>
21. Markham A. Belantamab Mafodotin: First Approval. *Drugs*. 2020 Oct 1;80(15):1607–13.
22. GSK pulls Blenrep cancer accelerated approval days after trial flop [Internet]. [cited 2023 Jan 1]. Available from: <https://www.fiercepharma.com/marketing/surprise-move-obedient-gsk-pulls-blenrep-accelerated-approval-days-after-confirmatory>
23. Joubert N, Denevault-Sabourin C, Bryden F, Viaud-Massuard MC. Towards antibody-drug conjugates and prodrug strategies with extracellular stimuli-responsive drug delivery in the tumor microenvironment for cancer therapy. *European Journal of Medicinal Chemistry*. 2017 Dec 15;142:393–415.
24. Giansanti F, Capone E, Ponziani S, Piccolo E, Gentile R, Lamolinara A, et al. Secreted Gal-3BP is a novel promising target for non-internalizing Antibody–Drug Conjugates. *Journal of Controlled Release*. 2019 Jan 28;294:176–84.
25. Hasan MdM, Laws M, Jin P, Rahman KM. Factors influencing the choice of monoclonal antibodies for antibody–drug conjugates. *Drug Discovery Today*. 2022 Jan 1;27(1):354–61.
26. Rudnick SI, Lou J, Shaller CC, Tang Y, Klein-Szanto AJP, Weiner LM, et al. Influence of affinity and antigen internalization on the uptake and penetration of Anti-HER2 antibodies in solid tumors. *Cancer Res*. 2011 Mar 15;71(6):2250–9.
27. Immunogenicity Testing of Therapeutic Protein Products —Developing and Validating Assays for Anti-Drug Antibody Detection Guidance for Industry. 2019;37.
28. Yaghoubi S, Karimi MH, Lotfinia M, Gharibi T, Mahi-Birjand M, Kavi E, et al. Potential drugs used in the antibody–drug conjugate (ADC) architecture for cancer therapy. *Journal of Cellular Physiology*. 2020;235(1):31–64.
29. Salomon PL, Singh R. Sensitive ELISA Method for the Measurement of Catabolites of Antibody–Drug Conjugates (ADCs) in Target Cancer Cells. *Mol Pharmaceutics*. 2015 Jun 1;12(6):1752–61.

## References

30. Bargh JD, Isidro-Llobet A, Parker JS, Spring DR. Cleavable linkers in antibody–drug conjugates. *Chem Soc Rev*. 2019 Aug 12;48(16):4361–74.
31. Burke PJ, Senter PD, Meyer DW, Miyamoto JB, Anderson M, Toki BE, et al. Design, synthesis, and biological evaluation of antibody-drug conjugates comprised of potent camptothecin analogues. *Bioconjug Chem*. 2009 Jun;20(6):1242–50.
32. Hamblett KJ, Senter PD, Chace DF, Sun MMC, Lenox J, Cerveny CG, et al. Effects of Drug Loading on the Antitumor Activity of a Monoclonal Antibody Drug Conjugate. *Clin Cancer Res*. 2004 Oct 15;10(20):7063–70.
33. Jackson DY. Processes for Constructing Homogeneous Antibody Drug Conjugates. *Org Process Res Dev*. 2016 May 20;20(5):852–66.
34. Lyon RP, Bovee TD, Doronina SO, Burke PJ, Hunter JH, Neff-LaFord HD, et al. Reducing hydrophobicity of homogeneous antibody-drug conjugates improves pharmacokinetics and therapeutic index. *Nat Biotechnol*. 2015 Jul;33(7):733–5.
35. Keam SJ. Trastuzumab Deruxtecan: First Approval. *Drugs*. 2020 Apr 1;80(5):501–8.
36. Syed YY. Sacituzumab Govitecan: First Approval. *Drugs*. 2020 Jul 1;80(10):1019–25.
37. Leal M, Sapra P, Hurvitz SA, Senter P, Wahl A, Schutten M, et al. Antibody–drug conjugates: an emerging modality for the treatment of cancer. *Annals of the New York Academy of Sciences*. 2014 Aug 1;1321(1):41–54.
38. Uadia P, Blair AH, Ghose T. Tumor and tissue distribution of a methotrexate-anti-EL4 immunoglobulin conjugate in EL4 lymphoma-bearing mice. *Cancer Res*. 1984 Oct;44(10):4263–6.
39. Poli GL, Bianchi C, Virotta G, Bettini A, Moretti R, Trachsel E, et al. Radretumab Radioimmunotherapy in Patients with Brain Metastasis: A 124I-L19SIP Dosimetric PET Study. *Cancer Immunology Research*. 2013 Aug 7;1(2):134–43.
40. Doronina SO, Mendelsohn BA, Bovee TD, Cerveny CG, Alley SC, Meyer DL, et al. Enhanced Activity of Monomethylauristatin F through Monoclonal Antibody Delivery: Effects of Linker Technology on Efficacy and Toxicity. *Bioconjugate Chem*. 2006 Jan 1;17(1):114–24.
41. Doronina SO, Toki BE, Torgov MY, Mendelsohn BA, Cerveny CG, Chace DF, et al. Development of potent monoclonal antibody auristatin conjugates for cancer therapy. *Nat Biotechnol*. 2003 Jul;21(7):778–84.
42. Widdison WC, Wilhelm SD, Cavanagh EE, Whiteman KR, Leece BA, Kovtun Y, et al. Semisynthetic Maytansine Analogues for the Targeted Treatment of Cancer. *J Med Chem*. 2006 Jul 1;49(14):4392–408.
43. Zein N, Sinha AM, McGahren WJ, Ellestad GA. Calicheamicin gamma 1I: an antitumor antibiotic that cleaves double-stranded DNA site specifically. *Science*. 1988 May 27;240(4856):1198–201.



## References

44. Ogitani Y, Aida T, Hagihara K, Yamaguchi J, Ishii C, Harada N, et al. DS-8201a, A Novel HER2-Targeting ADC with a Novel DNA Topoisomerase I Inhibitor, Demonstrates a Promising Antitumor Efficacy with Differentiation from T-DM1. *Clinical Cancer Research*. 2016 Oct 13;22(20):5097–108.
45. Goldenberg DM, Sharkey RM. Antibody-drug conjugates targeting TROP-2 and incorporating SN-38: A case study of anti-TROP-2 sacituzumab govitecan. *mAbs*. 2019 Aug 18;11(6):987–95.
46. Tietze LF, von Hof JM, Müller M, Krewer B, Schubert I. Glycosidic Prodrugs of Highly Potent Bifunctional Duocarmycin Derivatives for Selective Treatment of Cancer. *Angewandte Chemie International Edition*. 2010;49(40):7336–9.
47. Su D, Chen J, Cosino E, dela Cruz-Chuh J, Davis H, Del Rosario G, et al. Antibody–Drug Conjugates Derived from Cytotoxic seco-CBI-Dimer Payloads Are Highly Efficacious in Xenograft Models and Form Protein Adducts In Vivo. *Bioconjugate Chem*. 2019 May 15;30(5):1356–70.
48. Hartley JA, Flynn MJ, Bingham JP, Corbett S, Reinert H, Tiberghien A, et al. Pre-clinical pharmacology and mechanism of action of SG3199, the pyrrolbenzodiazepine (PBD) dimer warhead component of antibody-drug conjugate (ADC) payload tesirine. *Sci Rep*. 2018 Jul 11;8(1):10479.
49. Tong JTW, Harris PWR, Brimble MA, Kavianinia I. An Insight into FDA Approved Antibody-Drug Conjugates for Cancer Therapy. *Molecules*. 2021 Jan;26(19):5847.
50. Akaiwa M, Dugal-Tessier J, Mendelsohn BA. Antibody–Drug Conjugate Payloads; Study of Auristatin Derivatives. *Chemical and Pharmaceutical Bulletin*. 2020;68(3):201–11.
51. Maderna A, Leverett CA. Recent Advances in the Development of New Auristatins: Structural Modifications and Application in Antibody Drug Conjugates. *Mol Pharmaceutics*. 2015 Jun 1;12(6):1798–812.
52. Koichi MIYAZAKI, Motohiro KOBAYASHI, Tsugitaka NATSUME, Masaaki GONDO, Takashi MIKAMI, Kyoichi SAKAKIBARA, Shigeru TSUKAGOSHI et al. Synthesis and Antitumor Activity of Novel Dolastatin 10 Analogs. *Chemical & Pharmaceutical Bulletin*. 1995;43(10):1706–18.
53. Remillard S, Rebhun LI, Howie GA, Kupchan SM. Antimitotic activity of the potent tumor inhibitor maytansine. *Science*. 1975 Sep 19;189(4207):1002–5.
54. Ravry MJ, Omura GA, Birch R. Phase II evaluation of maytansine (NSC 153858) in advanced cancer. A Southeastern Cancer Study Group trial. *Am J Clin Oncol*. 1985 Apr 1;8(2):148–50.
55. Prokop A, Wrasidlo W, Lode H, Herold R, Lang F, Henze G, et al. Induction of apoptosis by enediyne antibiotic calicheamicin 9II proceeds through a caspase-mediated mitochondrial amplification loop in an entirely Bax-dependent manner. *Oncogene*. 2003 Dec;22(57):9107–20.

## References

56. Ricart AD. Antibody-Drug Conjugates of Calicheamicin Derivative: Gemtuzumab Ozogamicin and Inotuzumab Ozogamicin. *Clin Cancer Res.* 2011 Oct 15;17(20):6417–27.
57. Goldenberg DM, Stein R, Sharkey RM. The emergence of trophoblast cell-surface antigen 2 (TROP-2) as a novel cancer target. *Oncotarget.* 2018 Jun 22;9(48):28989–9006.
58. Kamal A, Ramesh G, Laxman N, Ramulu P, Srinivas O, Neelima K, et al. Design, synthesis, and evaluation of new noncross-linking pyrrolobenzodiazepine dimers with efficient DNA binding ability and potent antitumor activity. *J Med Chem.* 2002 Oct 10;45(21):4679–88.
59. Pei Z, Chen C, Chen J, Cruz-Chuh J dela, Delarosa R, Deng Y, et al. Exploration of Pyrrolobenzodiazepine (PBD)-Dimers Containing Disulfide-Based Prodrugs as Payloads for Antibody–Drug Conjugates. *Mol Pharmaceutics.* 2018 Sep 4;15(9):3979–96.
60. Jeffrey SC, Burke PJ, Lyon RP, Meyer DW, Sussman D, Anderson M, et al. A Potent Anti-CD70 Antibody–Drug Conjugate Combining a Dimeric Pyrrolobenzodiazepine Drug with Site-Specific Conjugation Technology. *Bioconjugate Chem.* 2013 Jul 17;24(7):1256–63.
61. Yao HP, Zhao H, Hudson R, Tong XM, Wang MH. Duocarmycin-based antibody–drug conjugates as an emerging biotherapeutic entity for targeted cancer therapy: Pharmaceutical strategy and clinical progress. *Drug Discovery Today.* 2021 Aug 1;26(8):1857–74.
62. Schwartz GH, Patnaik A, Hammond LA, Rizzo J, Berg K, Von Hoff DD, et al. A phase I study of bizelesin, a highly potent and selective DNA-interactive agent, in patients with advanced solid malignancies. *Annals of Oncology.* 2003 May 1;14(5):775–82.
63. Cristofanilli M, Bryan WJ, Miller LL, Chang AY, Gradishar WJ, Kufe DW, et al. Phase II study of adozelesin in untreated metastatic breast cancer. *Anticancer Drugs.* 1998 Oct 1;9(9):779–82.
64. Yu SF, Lee DW, Zheng B, del Rosario G, Leipold D, Booler H, et al. An Anti–CD22-seco-CBI-Dimer Antibody–Drug Conjugate (ADC) for the Treatment of Non-Hodgkin Lymphoma That Provides a Longer Duration of Response than Auristatin-Based ADCs in Preclinical Models. *Molecular Cancer Therapeutics.* 2021 Feb 5;20(2):340–6.
65. Dokter W, Ubink R, Lee M van der, Vleuten M van der, Achterberg T van, Jacobs D, et al. Preclinical Profile of the HER2-Targeting ADC SYD983/SYD985: Introduction of a New Duocarmycin-Based Linker-Drug Platform. *Mol Cancer Ther.* 2014 Nov 1;13(11):2618–29.
66. Nadal-Serrano M, Morancho B, Escrivá-de-Romaní S, Bernadó Morales C, Luque A, Escorihuela M, et al. The Second Generation Antibody-Drug Conjugate SYD985 Overcomes Resistances to T-DM1. *Cancers.* 2020 Mar;12(3):670.
67. Banerji U, van Herpen CML, Saura C, Thistlethwaite F, Lord S, Moreno V, et al. Trastuzumab duocarmazine in locally advanced and metastatic solid tumours and HER2-expressing breast cancer: a phase 1 dose-escalation and dose-expansion study. *The Lancet Oncology.* 2019 Aug 1;20(8):1124–35.

## References

68. Pillow TH, Tercel M. CHAPTER 11:Duocarmycin–PBD Dimers as Antibody–Drug Conjugate (ADC) Payloads. In: Cytotoxic Payloads for Antibody–Drug Conjugates [Internet]. 2019 [cited 2021 Oct 15]. p. 241–58. Available from: <https://pubs.rsc.org/en/content/chapter/bk9781788010771-00241/978-1-78801-077-1>
69. Tercel M, Stribbling SM, Sheppard H, Siim BG, Wu K, Pullen SM, et al. Unsymmetrical DNA Cross-Linking Agents: Combination of the CBI and PBD Pharmacophores. *J Med Chem*. 2003 May 1;46(11):2132–51.
70. Peck M, Rothenberg ME, Deng R, Lewin-Koh N, She G, Kamath AV, et al. A Phase 1, Randomized, Single-Ascending-Dose Study To Investigate the Safety, Tolerability, and Pharmacokinetics of DSTA4637S, an Anti-Staphylococcus aureus Thiomab Antibody-Antibiotic Conjugate, in Healthy Volunteers. *Antimicrobial Agents and Chemotherapy*. 63(6):e02588-18.
71. Buttgerit F, Aelion J, Rojkovich B, Zubrzycka-Sienkiewicz A, Radstake T, Chen S, et al. Op0115 Efficacy and Safety of Abbv-3373, a Novel Anti-Tnf Glucocorticoid Receptor Modulator Antibody Drug Conjugate, in Patients with Moderate to Severe Rheumatoid Arthritis Despite Methotrexate Therapy: A Phase 2a Proof of Concept Study. *Annals of the Rheumatic Diseases*. 2021 Jun 1;80(Suppl 1):64–64.
72. Lu J, Jiang F, Lu A, Zhang G. Linkers Having a Crucial Role in Antibody–Drug Conjugates. *International Journal of Molecular Sciences*. 2016 Apr;17(4):561.
73. Strop P, Liu SH, Dorywalska M, Delaria K, Dushin RG, Tran TT, et al. Location Matters: Site of Conjugation Modulates Stability and Pharmacokinetics of Antibody Drug Conjugates. *Chemistry & Biology*. 2013 Feb 21;20(2):161–7.
74. Lhospice F, Brégeon D, Belmant C, Dennler P, Chiotellis A, Fischer E, et al. Site-Specific Conjugation of Monomethyl Auristatin E to Anti-CD30 Antibodies Improves Their Pharmacokinetics and Therapeutic Index in Rodent Models. *Mol Pharm*. 2015 Jun 1;12(6):1863–71.
75. J. Walsh S, D. Bargh J, M. Dannheim F, R. Hanby A, Seki H, J. Counsell A, et al. Site-selective modification strategies in antibody–drug conjugates. *Chemical Society Reviews*. 2021;50(2):1305–53.
76. Modi S, Saura C, Yamashita T, Park YH, Kim SB, Tamura K, et al. Trastuzumab Deruxtecan in Previously Treated HER2-Positive Breast Cancer. *N Engl J Med*. 2020 Feb 13;382(7):610–21.
77. Wang L, Amphlett G, Blättler WA, Lambert JM, Zhang W. Structural characterization of the maytansinoid-monoclonal antibody immunoconjugate, huN901-DM1, by mass spectrometry. *Protein Sci*. 2005 Sep;14(9):2436–46.
78. Sun MMC, Beam KS, Cerveny CG, Hamblett KJ, Blackmore RS, Torgov MY, et al. Reduction-alkylation strategies for the modification of specific monoclonal antibody disulfides. *Bioconjug Chem*. 2005;16(5):1282–90.
79. Shen BQ, Xu K, Liu L, Raab H, Bhakta S, Kenrick M, et al. Conjugation site modulates the in vivo stability and therapeutic activity of antibody-drug conjugates. *Nat Biotechnol*. 2012 Jan 22;30(2):184–9.

## References

80. Fontaine SD, Reid R, Robinson L, Ashley GW, Santi DV. Long-term stabilization of maleimide-thiol conjugates. *Bioconjug Chem*. 2015 Jan 21;26(1):145–52.
81. Christie RJ, Fleming R, Bezabeh B, Woods R, Mao S, Harper J, et al. Stabilization of cysteine-linked antibody drug conjugates with N-aryl maleimides. *Journal of Controlled Release*. 2015 Dec 28;220:660–70.
82. Behrens CR, Ha EH, Chinn LL, Bowers S, Probst G, Fitch-Bruhns M, et al. Antibody–Drug Conjugates (ADCs) Derived from Interchain Cysteine Cross-Linking Demonstrate Improved Homogeneity and Other Pharmacological Properties over Conventional Heterogeneous ADCs. *Mol Pharmaceutics*. 2015 Nov 2;12(11):3986–98.
83. Badescu G, Bryant P, Bird M, Henseleit K, Swierkosz J, Parekh V, et al. Bridging disulfides for stable and defined antibody drug conjugates. *Bioconjug Chem*. 2014 Jun 18;25(6):1124–36.
84. Walsh SJ, Omarjee S, Galloway WRJD, Kwan TTL, Sore HF, Parker JS, et al. A general approach for the site-selective modification of native proteins, enabling the generation of stable and functional antibody–drug conjugates. *Chem Sci*. 2019 Jan 16;10(3):694–700.
85. Maruani A, Smith MEB, Miranda E, Chester KA, Chudasama V, Caddick S. A plug-and-play approach to antibody-based therapeutics via a chemoselective dual click strategy. *Nat Commun*. 2015 Mar 31;6:6645.
86. Agarwal P, Bertozzi CR. Site-Specific Antibody–Drug Conjugates: The Nexus of Bioorthogonal Chemistry, Protein Engineering, and Drug Development. *Bioconjugate Chem*. 2015 Feb 18;26(2):176–92.
87. Junutula JR, Raab H, Clark S, Bhakta S, Leipold DD, Weir S, et al. Site-specific conjugation of a cytotoxic drug to an antibody improves the therapeutic index. *Nat Biotechnol*. 2008 Aug;26(8):925–32.
88. Vollmar BS, Wei B, Ohri R, Zhou J, He J, Yu SF, et al. Attachment Site Cysteine Thiol pKa Is a Key Driver for Site-Dependent Stability of THIOMAB Antibody–Drug Conjugates. *Bioconjug Chem*. 2017 Oct 18;28(10):2538–48.
89. Pillow TH, Tien J, Parsons-Reponte KL, Bhakta S, Li H, Staben LR, et al. Site-specific trastuzumab maytansinoid antibody–drug conjugates with improved therapeutic activity through linker and antibody engineering. *J Med Chem*. 2014 Oct 9;57(19):7890–9.
90. Govindan SV, Goldenberg DM. Designing immunoconjugates for cancer therapy. *Expert Opinion on Biological Therapy*. 2012 Jul;12(7):873–90.
91. Erickson HK, Widdison WC, Mayo MF, Whiteman K, Audette C, Wilhelm SD, et al. Tumor Delivery and In Vivo Processing of Disulfide-Linked and Thioether-Linked Antibody–Maytansinoid Conjugates. *Bioconjugate Chem*. 2010 Jan 20;21(1):84–92.
92. van der Lee MMC, Groothuis PG, Ubink R, van der Vleuten MAJ, van Achterberg TA, Loosveld EM, et al. The Preclinical Profile of the Duocarmycin-Based HER2-Targeting ADC SYD985 Predicts for Clinical Benefit in Low HER2-Expressing Breast Cancers. *Mol Cancer Ther*. 2015 Mar;14(3):692–703.

## References

93. Hamann PR, Hinman LM, Hollander I, Beyer CF, Lindh D, Holcomb R, et al. Gemtuzumab Ozogamicin, A Potent and Selective Anti-CD33 Antibody–Calicheamicin Conjugate for Treatment of Acute Myeloid Leukemia. *Bioconjugate Chem.* 2002 Jan 1;13(1):47–58.
94. DiJoseph JF, Khandke K, Dougher MM, Evans DY, Armellino DC, Hamann PR, et al. CMC-544 (inotuzumab ozogamicin): A CD22-targeted immunoconjugate of calicheamicin. *Hematology Meeting Reports (formerly Haematologica Reports)* [Internet]. 2008 [cited 2021 Aug 6];2(5). Available from: <https://www.pagepress.org/journals/index.php/hmr/article/view/735>
95. Doronina SO, Toki BE, Torgov MY, Mendelsohn BA, Cervený CG, Chace DF, et al. Development of potent monoclonal antibody auristatin conjugates for cancer therapy. *Nat Biotechnol.* 2003 Jul;21(7):778–84.
96. Boedtker E, Pedersen SF. The Acidic Tumor Microenvironment as a Driver of Cancer. *Annual Review of Physiology.* 2020;82(1):103–26.
97. DiJoseph JF, Dougher MM, Armellino DC, Kalyandrug L, Kunz A, Boghaert ER, et al. CD20-specific antibody-targeted chemotherapy of non-Hodgkin's B-cell lymphoma using calicheamicin-conjugated rituximab. *Cancer Immunol Immunother.* 2007 Jul 1;56(7):1107–17.
98. Moon SJ, Govindan SV, Cardillo TM, D'Souza CA, Hansen HJ, Goldenberg DM. Antibody conjugates of 7-ethyl-10-hydroxycamptothecin (SN-38) for targeted cancer chemotherapy. *J Med Chem.* 2008 Nov 13;51(21):6916–26.
99. Wang J, Li S, Luo T, Wang C, Zhao J. Disulfide Linkage: A Potent Strategy in Tumor-Targeting Drug Discovery. *Current Medicinal Chemistry.* 2012 Jun 1;19(18):2976–83.
100. Mills BJ, Lang CA. Differential distribution of free and bound glutathione and cyst(e)ine in human blood. *Biochemical Pharmacology.* 1996 Aug 9;52(3):401–6.
101. Gamcsik MP, Kasibhatla MS, Teeter SD, Colvin OM. Glutathione levels in human tumors. *Biomarkers.* 2012 Dec 1;17(8):671–91.
102. Bernardes GJL, Casi G, Trüssel S, Hartmann I, Schwager K, Scheuermann J, et al. A Traceless Vascular-Targeting Antibody–Drug Conjugate for Cancer Therapy. *Angewandte Chemie International Edition.* 2012;51(4):941–4.
103. Perrino E, Steiner M, Krall N, Bernardes GJL, Pretto F, Casi G, et al. Curative properties of noninternalizing antibody-drug conjugates based on maytansinoids. *Cancer Res.* 2014 May 1;74(9):2569–78.
104. J. Stenton B, L. Oliveira B, J. Matos M, Sinatra L, L. Bernardes GJ. A thioether-directed palladium-cleavable linker for targeted bioorthogonal drug decaging. *Chemical Science.* 2018;9(17):4185–9.
105. Engels J, Schlaeger EJ. Synthesis, structure, and reactivity of adenosine cyclic 3',5'-phosphate-benzyltriesters. *J Med Chem.* 1977 Jul;20(7):907–11.

## References

106. Li J, Xiao D, Xie F, Li W, Zhao L, Sun W, et al. Novel antibody-drug conjugate with UV-controlled cleavage mechanism for cytotoxin release. *Bioorganic Chemistry*. 2021 Jun 1;111:104475.
107. Nani RR, Gorka AP, Nagaya T, Yamamoto T, Ivanic J, Kobayashi H, et al. In Vivo Activation of Duocarmycin–Antibody Conjugates by Near-Infrared Light. *ACS Cent Sci*. 2017 Apr 26;3(4):329–37.
108. Cooper E, Choi PJ, Denny WA, Jose J, Dragunow M, Park TIH. The Use of Heptamethine Cyanine Dyes as Drug-Conjugate Systems in the Treatment of Primary and Metastatic Brain Tumors. *Frontiers in Oncology*. 2021;11:1336.
109. Lysosomal cysteine proteases: facts and opportunities. *The EMBO Journal*. 2001 Sep 3;20(17):4629–33.
110. Mohamed MM, Sloane BF. multifunctional enzymes in cancer. *Nat Rev Cancer*. 2006 Oct;6(10):764–75.
111. Aggarwal N, Sloane BF. Cathepsin B: Multiple roles in cancer. *Proteomics Clin Appl*. 2014 Jun;8(0):427–37.
112. Joyce JA, Baruch A, Chehade K, Meyer-Morse N, Giraudo E, Tsai FY, et al. Cathepsin cysteine proteases are effectors of invasive growth and angiogenesis during multistage tumorigenesis. *Cancer Cell*. 2004 May 1;5(5):443–53.
113. Dorywalska M, Strop P, Melton-Witt JA, Hasa-Moreno A, Farias SE, Galindo Casas M, et al. Effect of attachment site on stability of cleavable antibody drug conjugates. *Bioconjug Chem*. 2015 Apr 15;26(4):650–9.
114. Caculitan NG, Dela Cruz Chuh J, Ma Y, Zhang D, Kozak KR, Liu Y, et al. Cathepsin B Is Dispensable for Cellular Processing of Cathepsin B-Cleavable Antibody-Drug Conjugates. *Cancer Res*. 2017 Dec 15;77(24):7027–37.
115. Dorywalska M, Dushin R, Moine L, Farias SE, Zhou D, Navaratnam T, et al. Molecular Basis of Valine-Citrulline-PABC Linker Instability in Site-Specific ADCs and Its Mitigation by Linker Design. *Mol Cancer Ther*. 2016 May;15(5):958–70.
116. Dubowchik GM, Mosure K, Knipe JO, Firestone RA. Cathepsin B-sensitive dipeptide prodrugs. 2. Models of anticancer drugs paclitaxel (Taxol®), mitomycin C and doxorubicin. *Bioorganic & Medicinal Chemistry Letters*. 1998 Dec 1;8(23):3347–52.
117. Dubowchik GM, Firestone RA, Padilla L, Willner D, Hofstead SJ, Mosure K, et al. Cathepsin B-Labile Dipeptide Linkers for Lysosomal Release of Doxorubicin from Internalizing Immunoconjugates: Model Studies of Enzymatic Drug Release and Antigen-Specific In Vitro Anticancer Activity. *Bioconjugate Chem*. 2002 Jul 1;13(4):855–69.
118. Dubowchik GM, Firestone RA. Cathepsin B-sensitive dipeptide prodrugs. 1. A model study of structural requirements for efficient release of doxorubicin. *Bioorganic & Medicinal Chemistry Letters*. 1998 Dec 1;8(23):3341–6.

## References

119. Deeks ED. Polatuzumab Vedotin: First Global Approval. *Drugs*. 2019 Sep 1;79(13):1467–75.
120. Chang E, Weinstock C, Zhang L, Charlab R, Dorff SE, Gong Y, et al. FDA Approval Summary: Enfortumab Vedotin for Locally Advanced or Metastatic Urothelial Carcinoma. *Clinical Cancer Research*. 2021 Feb 15;27(4):922–7.
121. Shiose Y, Ochi Y, Kuga H, Yamashita F, Hashida M. Relationship between Drug Release of DE-310, Macromolecular Prodrug of DX-8951f, and Cathepsins Activity in Several Tumors. *Biological and Pharmaceutical Bulletin*. 2007 Dec 1;30(12):2365–70.
122. Ogitani Y, Aida T, Hagihara K, Yamaguchi J, Ishii C, Harada N, et al. DS-8201a, A Novel HER2-Targeting ADC with a Novel DNA Topoisomerase I Inhibitor, Demonstrates a Promising Antitumor Efficacy with Differentiation from T-DM1. *Clin Cancer Res*. 2016 Oct 15;22(20):5097–108.
123. Burke PJ, Toki BE, Meyer DW, Miyamoto JB, Kissler KM, Anderson M, et al. Novel immunoconjugates comprised of streptonigrin and 17-amino-geldanamycin attached via a dipeptide-p-aminobenzyl-amine linker system. *Bioorganic & Medicinal Chemistry Letters*. 2009 May 15;19(10):2650–3.
124. Wang Y, Fan S, Zhong W, Zhou X, Li S. Development and Properties of Valine-Alanine based Antibody-Drug Conjugates with Monomethyl Auristatin E as the Potent Payload. *International Journal of Molecular Sciences*. 2017 Sep;18(9):1860.
125. Jeffrey SC, Nguyen MT, Andreyka JB, Meyer DL, Doronina SO, Senter PD. Dipeptide-based highly potent doxorubicin antibody conjugates. *Bioorganic & Medicinal Chemistry Letters*. 2006 Jan 15;16(2):358–62.
126. Cazzamalli S, Corso AD, Neri D. Linker stability influences the anti-tumor activity of acetazolamide-drug conjugates for the therapy of renal cell carcinoma. *J Control Release*. 2017 Jan 28;246:39–45.
127. Wei B, Gunzner-Toste J, Yao H, Wang T, Wang J, Xu Z, et al. Discovery of Peptidomimetic Antibody–Drug Conjugate Linkers with Enhanced Protease Specificity. *J Med Chem*. 2018 Feb 8;61(3):989–1000.
128. Tranoy-Opalinski I, Legigan T, Barat R, Clarhaut J, Thomas M, Renoux B, et al.  $\beta$ -Glucuronidase-responsive prodrugs for selective cancer chemotherapy: An update. *European Journal of Medicinal Chemistry*. 2014 Mar 3;74:302–13.
129. Dal Corso A, Cazzamalli S, Gébleux R, Mattarella M, Neri D. Protease-Cleavable Linkers Modulate the Anticancer Activity of Noninternalizing Antibody–Drug Conjugates. *Bioconjugate Chem*. 2017 Jul 19;28(7):1826–33.
130. Bahar FG, Ohura K, Ogihara T, Imai T. Species Difference of Esterase Expression and Hydrolase Activity in Plasma. *Journal of Pharmaceutical Sciences*. 2012 Oct 1;101(10):3979–88.
131. Renoux B, Raes F, Legigan T, Péraudeau E, Eddhif B, Poinot P, et al. Targeting the tumour microenvironment with an enzyme-responsive drug delivery system for the efficient therapy of breast and pancreatic cancers. *Chemical Science*. 2017;8(5):3427–33.

## References

132. Jeffrey SC, Andreyka JB, Bernhardt SX, Kissler KM, Kline T, Lenox JS, et al. Development and Properties of  $\beta$ -Glucuronide Linkers for Monoclonal Antibody–Drug Conjugates. *Bioconjugate Chem.* 2006 May 1;17(3):831–40.
133. Li F, Emmerton KK, Jonas M, Zhang X, Miyamoto JB, Setter JR, et al. Intracellular Released Payload Influences Potency and Bystander-Killing Effects of Antibody-Drug Conjugates in Preclinical Models. *Cancer Res.* 2016 May 1;76(9):2710–9.
134. Kolodych S, Michel C, Delacroix S, Koniev O, Ehkirch A, Eberova J, et al. Development and evaluation of  $\beta$ -galactosidase-sensitive antibody-drug conjugates. *Eur J Med Chem.* 2017 Dec 15;142:376–82.
135. Legigan T, Clarhaut J, Tranoy-Opalinski I, Monvoisin A, Renoux B, Thomas M, et al. The First Generation of  $\beta$ -Galactosidase-Responsive Prodrugs Designed for the Selective Treatment of Solid Tumors in Prodrug Monotherapy. *Angewandte Chemie.* 2012;124(46):11774–8.
136. Kern JC, Dooney D, Zhang R, Liang L, Brandish PE, Cheng M, et al. Novel Phosphate Modified Cathepsin B Linkers: Improving Aqueous Solubility and Enhancing Payload Scope of ADCs. *Bioconjugate Chem.* 2016 Sep 21;27(9):2081–8.
137. Kern JC, Cancilla M, Dooney D, Kwasnjuk K, Zhang R, Beaumont M, et al. Discovery of Pyrophosphate Diesters as Tunable, Soluble, and Bioorthogonal Linkers for Site-Specific Antibody–Drug Conjugates. *J Am Chem Soc.* 2016 Feb 3;138(4):1430–45.
138. D. Bargh J, J. Walsh S, Isidro-Llobet A, Omarjee S, S. Carroll J, R. Spring D. Sulfatase-cleavable linkers for antibody-drug conjugates. *Chemical Science.* 2020;11(9):2375–80.
139. Hanson SR, Best MD, Wong CH. Sulfatases: Structure, Mechanism, Biological Activity, Inhibition, and Synthetic Utility. *Angewandte Chemie International Edition.* 2004;43(43):5736–63.
140. Albin N, Massaad L, Toussaint C, Mathieu MC, Morizet J, Parise O, et al. Main drug-metabolizing enzyme systems in human breast tumors and peritumoral tissues. *Cancer Res.* 1993 Aug 1;53(15):3541–6.
141. D. Bargh J, J. Walsh S, Ashman N, Isidro-Llobet A, S. Carroll J, R. Spring D. A dual-enzyme cleavable linker for antibody–drug conjugates. *Chemical Communications.* 2021;57(28):3457–60.
142. Lübke T, Damme M. Lysosomal sulfatases: a growing family. *Biochem J.* 2020 Oct 30;477(20):3963–83.
143. Correia MSP, Ballet C, Meistermann H, Conway LP, Globisch D. Comprehensive kinetic and substrate specificity analysis of an arylsulfatase from *Helix pomatia* using mass spectrometry. *Bioorganic & Medicinal Chemistry.* 2019 Mar 15;27(6):955–62.
144. Williams DB, Varia SA, Stella VJ, Pitman IH. Evaluation of the prodrug potential of the sulfate esters of acetaminophen and 3-hydroxymethyl-phenytoin. *International Journal of Pharmaceutics.* 1983 Mar 1;14(1):113–20.



## References

145. Stella VJ, Nti-Addae KW. Prodrug strategies to overcome poor water solubility. *Advanced Drug Delivery Reviews*. 2007 Jul 30;59(7):677–94.
146. Leenders RGG, Scheeren HW, Houba PHJ, Boven E, Haisma HJ. Synthesis and evaluation of novel daunomycin-phosphate-sulfate  $\beta$ -glucuronide and  $\beta$ -glucoside prodrugs for application in adepts. *Bioorganic & Medicinal Chemistry Letters*. 1995 Dec 21;5(24):2975–80.
147. Coughtrie MW, Bamforth KJ, Sharp S, Jones AL, Borthwick EB, Barker EV, et al. Sulfation of endogenous compounds and xenobiotics--interactions and function in health and disease. *Chem Biol Interact*. 1994 Jun;92(1–3):247–56.
148. Diez-Roux G, Ballabio A. Sulfatases and Human Disease. *Annual Review of Genomics and Human Genetics*. 2005;6(1):355–79.
149. Hernandez-Guzman FG, Higashiyama T, Pangborn W, Osawa Y, Ghosh D. Structure of Human Estrone Sulfatase Suggests Functional Roles of Membrane Association\*. *Journal of Biological Chemistry*. 2003 Jun 20;278(25):22989–97.
150. Robertson DA, Freeman C, Morris CP, Hopwood JJ. A cDNA clone for human glucosamine-6-sulphatase reveals differences between arylsulphatases and non-arylsulphatases. *Biochem J*. 1992 Dec 1;288(Pt 2):539–44.
151. Lukatela G, Krauss N, Theis K, Selmer T, Gieselmann V, von Figura K, et al. Crystal structure of human arylsulfatase A: the aldehyde function and the metal ion at the active site suggest a novel mechanism for sulfate ester hydrolysis. *Biochemistry*. 1998 Mar 17;37(11):3654–64.
152. Bond CS, Clements PR, Ashby SJ, Collyer CA, Harrop SJ, Hopwood JJ, et al. Structure of a human lysosomal sulfatase. *Structure*. 1997 Feb 15;5(2):277–89.
153. Demydchuk M, Hill CH, Zhou A, Bunkóczi G, Stein PE, Marchesan D, et al. Insights into Hunter syndrome from the structure of iduronate-2-sulfatase. *Nat Commun*. 2017 Jun 8;8(1):15786.
154. Rivera-Colón Y, Schutsky EK, Kita AZ, Garman SC. The Structure of Human GALNS Reveals the Molecular Basis for Mucopolysaccharidosis IV A. *Journal of Molecular Biology*. 2012 Nov 9;423(5):736–51.
155. Sidhu NS, Schreiber K, Pröpper K, Becker S, Usón I, Sheldrick GM, et al. Structure of sulfamidase provides insight into the molecular pathology of mucopolysaccharidosis IIIA. *Acta Cryst D*. 2014 May 1;70(5):1321–35.
156. Morimoto-Tomita M, Uchimura K, Werb Z, Hemmerich S, Rosen SD. Cloning and Characterization of Two Extracellular Heparin-degrading Endosulfatases in Mice and Humans \*. *Journal of Biological Chemistry*. 2002 Dec 20;277(51):49175–85.
157. Waldow A, Schmidt B, Dierks T, von Bülow R, von Figura K. Amino acid residues forming the active site of arylsulfatase A. Role in catalytic activity and substrate binding. *J Biol Chem*. 1999 Apr 30;274(18):12284–8.

## References

158. Appel MJ, Bertozzi CR. Formylglycine, a Post-Translationally Generated Residue with Unique Catalytic Capabilities and Biotechnology Applications. *ACS Chem Biol*. 2015 Jan 16;10(1):72–84.
159. Schmidt B, Selmer T, Ingendoh A, Figurat K von. A novel amino acid modification in sulfatases that is defective in multiple sulfatase deficiency. *Cell*. 1995 Jul 28;82(2):271–8.
160. Chruszcz M, Laidler P, Monkiewicz M, Ortlund E, Lebioda L, Lewinski K. Crystal structure of a covalent intermediate of endogenous human arylsulfatase A. *Journal of Inorganic Biochemistry*. 2003 Aug 1;96(2):386–92.
161. Jonas S, van Loo B, Hyvönen M, Hollfelder F. A New Member of the Alkaline Phosphatase Superfamily with a Formylglycine Nucleophile: Structural and Kinetic Characterisation of a Phosphonate Monoester Hydrolase/Phosphodiesterase from *Rhizobium leguminosarum*. *Journal of Molecular Biology*. 2008 Dec 5;384(1):120–36.
162. von Bülow R, Schmidt B, Dierks T, von Figura K, Usón I. Crystal Structure of an Enzyme-Substrate Complex Provides Insight into the Interaction between Human Arylsulfatase A and its Substrates During Catalysis. *Journal of Molecular Biology*. 2001 Jan 12;305(2):269–77.
163. Chai CL, Loughlin WA, Lowe G. The stereochemical course of sulphuryl transfer catalysed by arylsulphatase II from *Aspergillus oryzae*. *Biochem J*. 1992 Nov 1;287(Pt 3):805–12.
164. Ahmed V, Ispahany M, Ruttgaizer S, Guillemette G, Taylor SD. A fluorogenic substrate for the continuous assaying of aryl sulfatases. *Anal Biochem*. 2005 May 1;340(1):80–8.
165. Woo LWL, Ganeshapillai D, Thomas MP, Sutcliffe OB, Malini B, Mahon MF, et al. Structure–Activity Relationship for the First-in-Class Clinical Steroid Sulfatase Inhibitor Irosustat (STX64, BN83495). *ChemMedChem*. 2011 Nov 4;6(11):2019–34.
166. Ahmed S, James K, Patel CK. First Report of the Investigation into the Importance of pKa in the Inhibition of Estrone Sulfatase by Sulfamate Containing Compounds. *Biochemical and Biophysical Research Communications*. 2000 Jun 7;272(2):583–5.
167. Ahmed S, Owen CP, James K, Patel CK, Patel M. Acid dissociation constant, a potential physicochemical factor in the inhibition of the enzyme estrone sulfatase (ES). *Bioorganic & Medicinal Chemistry Letters*. 2001 Apr 9;11(7):899–902.
168. Howarth NM, Purohit A, Robinson JJ, Vicker N, Reed MJ, Potter BVL. Estrone 3-Sulfate Mimics, Inhibitors of Estrone Sulfatase Activity: Homology Model Construction and Docking Studies. *Biochemistry*. 2002 Dec 1;41(50):14801–14.
169. Anderson C, Freeman J, Lucas LH, Farley M, Dalhoumi H, Widlanski TS. Estrone Sulfatase: Probing Structural Requirements for Substrate and Inhibitor Recognition. *Biochemistry*. 1997 Mar 1;36(9):2586–94.
170. Rinderknecht H, Geokas MC, Carmack C, Haverback BJ. The determination of arylsulfatases in biological fluids. *Clinica Chimica Acta*. 1970 Sep 1;29(3):481–91.

## References

171. The activity of arylsulfatase A and B on tyrosine O-sulfates. *Biochimica et Biophysica Acta (BBA) - Enzymology*. 1979 Feb 9;566(2):321–6.
172. Austin J, McAfee D, Armstrong D, O'Rourke M, Shearer L, Bachhawat B, et al. Abnormal Sulphatase Activities in Two Human Diseases (Metachromatic Leucodystrophy and Gargoylism). *Biochemical Journal*. 1964 Nov 1;93(2):15C-17C.
173. Cerebroside 3-sulfate as a physiological substrate of arylsulfatase A. *Biochimica et Biophysica Acta (BBA) - Enzymology*. 1968 Mar 25;151(3):619–27.
174. Morihiro K, Ankenbruck N, Lukasak B, Deiters A. Small Molecule Release and Activation through DNA Computing. *J Am Chem Soc*. 2017 Oct 4;139(39):13909–15.
175. Miller MA, Mikula H, Luthria G, Li R, Kronister S, Prytyskach M, et al. Modular Nanoparticulate Prodrug Design Enables Efficient Treatment of Solid Tumors Using Bioorthogonal Activation. *ACS Nano*. 2018 Dec 26;12(12):12814–26.
176. Jia H, Hu G, Shi D, Gan L, Zhang H, Yao X, et al. Fluorophore-Dependent Cleavage of Disulfide Bond Leading to a Highly Selective Fluorescent Probe of Thioredoxin. *Anal Chem*. 2019 Jul 2;91(13):8524–31.
177. Penney CL, Perlin AS. A method for the sulfation of sugars, employing a stable, aryl sulfate intermediate. *Carbohydrate Research*. 1981 Jul 1;93(2):241–6.
178. Simpson LS, Widlanski TS. A Comprehensive Approach to the Synthesis of Sulfate Esters. *J Am Chem Soc*. 2006 Feb 1;128(5):1605–10.
179. Taylor SD, Desoky A. Rapid and efficient chemoselective and multiple sulfations of phenols using sulfuryl imidazolium salts. *Tetrahedron Letters*. 2011 Jun 29;52(26):3353–7.
180. Desoky AY, Hendel J, Ingram L, Taylor SD. Preparation of trifluoroethyl- and phenyl-protected sulfates using sulfuryl imidazolium salts. *Tetrahedron*. 2011 Feb 11;67(6):1281–7.
181. Ingram LJ, Desoky A, Ali AM, Taylor SD. O- and N-Sulfations of Carbohydrates Using Sulfuryl Imidazolium Salts. *J Org Chem*. 2009 Sep 4;74(17):6479–85.
182. Liu Y, Lien IFF, Ruttgaizer S, Dove P, Taylor SD. Synthesis and Protection of Aryl Sulfates Using the 2,2,2-Trichloroethyl Moiety. *Org Lett*. 2004 Jan 1;6(2):209–12.
183. Proud AD, Prodder JC, Flitsch SL. Development of a protecting group for sulfate esters. *Tetrahedron Letters*. 1997 Oct 13;38(41):7243–6.
184. Hay MP, Anderson RF, Ferry DM, Wilson WR, Denny WA. Synthesis and Evaluation of Nitroheterocyclic Carbamate Prodrugs for Use with Nitroreductase-Mediated Gene-Directed Enzyme Prodrug Therapy. *J Med Chem*. 2003 Dec 1;46(25):5533–45.
185. Devendra R, Edmonds NR, Söhnel T. Computational and experimental investigations of the urethane formation mechanism in the presence of organotin(IV) carboxylate catalysts. *Journal of Molecular Catalysis A: Chemical*. 2013 Jan 1;366:126–39.

## References

186. Velikorodov AV, Imasheva NM. Synthesis of carbamate derivatives of coumarin and chromene. *Russ J Org Chem*. 2008 Sep 1;44(9):1374–7.
187. Roy AB. Sulfatases from *Helix pomatia*. In: *Methods in Enzymology* [Internet]. Academic Press; 1987 [cited 2021 Aug 10]. p. 361–6. (Sulfur and Sulfur Amino Acids; vol. 143). Available from: <https://www.sciencedirect.com/science/article/pii/0076687987430644>
188. Hay MP, Sykes BM, Denny WA, O'Connor CJ. Substituent effects on the kinetics of reductively-initiated fragmentation of nitrobenzyl carbamates designed as triggers for bioreductive prodrugs. *J Chem Soc, Perkin Trans 1*. 1999 Jan 1;(19):2759–70.
189. Ottanà R, Maccari R, Mortier J, Caselli A, Amuso S, Camici G, et al. Synthesis, biological activity and structure–activity relationships of new benzoic acid-based protein tyrosine phosphatase inhibitors endowed with insulinomimetic effects in mouse C2C12 skeletal muscle cells. *European Journal of Medicinal Chemistry*. 2014 Jan 7;71:112–27.

## References

